Old Dominion University

ODU Digital Commons

Electrical & Computer Engineering Theses & Dissertations

Electrical & Computer Engineering

Winter 2004

Electrical Breakdown in Polar Liquids

Shu Xiao
Old Dominion University

Follow this and additional works at: https://digitalcommons.odu.edu/ece_etds

 Part of the Electrical and Computer Engineering Commons

Recommended Citation

Xiao, Shu. "Electrical Breakdown in Polar Liquids" (2004). Doctor of Philosophy (PhD), Dissertation, Electrical & Computer Engineering, Old Dominion University, DOI: 10.25777/vm33-5163
https://digitalcommons.odu.edu/ece_etds/147

This Dissertation is brought to you for free and open access by the Electrical & Computer Engineering at ODU Digital Commons. It has been accepted for inclusion in Electrical & Computer Engineering Theses & Dissertations by an authorized administrator of ODU Digital Commons. For more information, please contact digitalcommons@odu.edu.

Electrical Breakdown in Polar Liquids

by

Shu Xiao
B.S. July 1996, Gannan Teacher College
M.S. August 1999, University of Electronic Science and Technology of China

A Dissertation Submitted to the Faculty of
Old Dominion University in Partial Fulfillment of the
Requirement for the Degree of

DOCTOR OF PHILOSOPHY

ELECTRICAL ENGINEERING

OLD DOMINION UNIVERSITY
December 2004

Approved by:

Karl H. Schoenbach (Director)

Ravindra P. Joshi (Member)

John B. Cooper (Member)

Mounir Laroussi (Member)

Reproduced with permission of the copyright owner. Further reproduction prohibited without permission.

ABSTRACT

ELECTRICAL BREAKDOWN IN POLAR LIQUIDS

Shu Xiao
Old Dominion University, 2004
Director: Dr. Karl H. Schoenbach

Hydrodynamic processes following the electrical breakdown in polar liquids, mainly water and propylene carbonate, are studied with electrical pulse-probe systems and optical diagnostics including shadowgraphy and Schlieren techniques. The dielectric strength of water in a repetitively pulsed power system is found to be 750 kV/cm and 650 kV/cm for pulses of 200 nanosecond and 8 microsecond duration, respectively. For energies less than 1 J, the discharge plasma decays in approximately one microsecond. The mechanical effect created by the expanding plasma is a shock wave which has an initial pressure of 1 GPa and decays within approximately 5 microseconds. The observed shock wave pattern is determined by the electrode geometry. The percentage of energy converted to shock energy is decreased as total energy rises, for example, 20% for total energy of 15 J and 8% for 50 J. The process following shock wave emission is the formation of a vapor bubble caused by the Joule heating of the liquid. It takes approximately 250 microseconds for the vapor bubble to reach its maximum size and a millisecond to decay. The presence of the vapor bubble determines the recovery of the dielectric strength after breakdown as shown with the electrical pulse-probe measurements. The vapor bubble formation scales with the energy input. The duration of vapor bubble is increased by a factor of ten when the energy is increased from 1 J to 50 J. Besides water, propylene

Reproduced with permission of the copyright owner. Further reproduction prohibited without permission.

carbonate is also studied with regard to its dielectric strength, breakdown, and postbreakdown development. Propylene carbonate has shown a breakdown strength of 760 kV/cm. Electrical breakdown in propylene carbonate at 1 J has also shown similar temporal development as water for plasma decay, shock wave emission, and vapor bubble expansion. However, due to the formation of polymers during the discharge, it takes several seconds to restore its dielectric strength. Both water and propylene carbonate are self-healing polar liquids, allowing repetitive applications. The repetition rate can be increased to values exceeding 1 kHz by applying laminar flow.

Reproduced with permission of the copyright owner. Further reproduction prohibited without permission.

ACKNOWLEDGMENTS

I would like to express my sincere appreciation and gratitude to my advisor, Dr. Karl Schoenbach, for his guidance and continuous support of my study. I would like to thank Dr. Ravindra P. Joshi, Dr. Jonh B. Cooper, and Dr. Mounir Laroussi for serving on my dissertation committee.

I am grateful for valuable discussions with Dr. Jurgen Kolb, Dr. Christian Bickes, Dr. Sunao Katsuki, Dr. Susumu Kono, Dr. Chungqi Jiang, Dr. Mohamed Moselhy, Dr. Muhammad Abdel-Aleam, and Dr. Frank Leipold. I also would like to thank to Ron Bentley, Nobuhiko Takano, and Srida BabuTala for their help and cooperation during the course of this dissertation. I want to express my special thanks to Rachel Shevin for her corrections of the thesis.

I extend many thanks to Barbara Carroll for her help in my study at the Center for Bioelectrics.

My gratitude is devoted to my wife, Feng Lian, for the love and support she has provided through my academic endeavors. Finally, I would like to thank my parents for their love and inspiration during the completion of this dissertation.

Reproduced with permission of the copyright owner. Further reproduction prohibited without permission.

TABLE OF CONTENTS

Reproduced with permission of the copyright owner. Further reproduction prohibited without permission.

Reproduced with permission of the copyright owner. Further reproduction prohibited without permission.

Reproduced with permission of the copyright owner. Further reproduction prohibited without permission.

LIST OF TABLES

Reproduced with permission of the copyright owner. Further reproduction prohibited without permission.

LIST OF FIGURES

Figure Page

Reproduced with permission of the copyright owner. Further reproduction prohibited without permission.

Reproduced with permission of the copyright owner. Further reproduction prohibited without permission.

Reproduced with permission of the copyright owner. Further reproduction prohibited without permission.

Reproduced with permission of the copyright owner. Further reproduction prohibited without permission.

CHAPTER I

INTRODUCTION

Electrical discharges in liquids, which involve aspects of plasma physics, electrochemistry, fluid dynamics and material sciences, have been studied extensively [1-3]. Liquid breakdown phenomena are related to many fields including energy storage [4-6], switching media [7-8], high voltage insulation [9], and acoustic devices [10-12]. Notably, polar liquids have large dielectric constants and allow a relatively small volume to store a large energy.

1.1 POLAR LIQUIDS

Water, a typical example of a polar liquid, is held together by hydrogen bonding (Fig. 1.1). Its bond strength is between the weak van-der-Waals and the strong covalent bond (Table 1.1). Due to its large dipole moment, the dielectric constant of water is dominated by the reorientation of the molecule. Water changes its dipole arrangements, and thus its dielectric constant, under an electrical field, a phenomenon known as the Kerr effect [13]. For extremely high electric fields (>> 1 MV/cm) additional changes in dielectric constant are expected [14].

Liquid water can be thought of as a seething mass of water molecules in which hydrogen-bonded clusters are continually forming, breaking apart, and re-forming. Because the energy of a hydrogen bond is comparable to the average thermal energy at ordinary temperatures, thermal motions dislocate these bonds

---

Journal Mode used in this thesis is *Journal of Applied Physics.*

Reproduced with permission of the copyright owner. Further reproduction prohibited without permission.

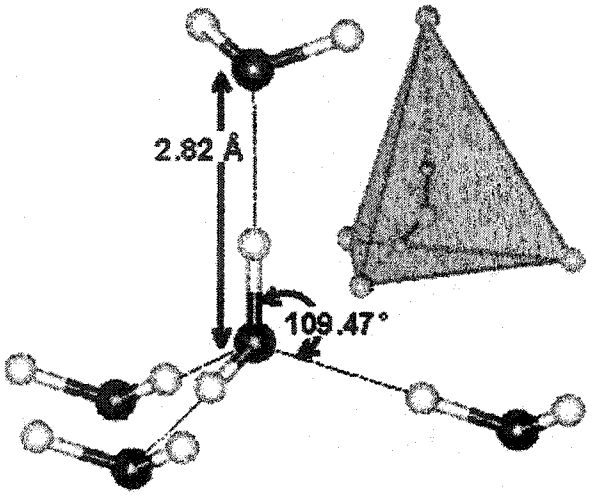

(a)

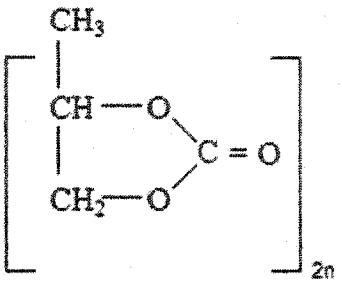

Propylene carbonate

(b)

FIG. 1.1. Polar liquids. a) Water holds molecules together by hydrogen bond. b) Propylene carbonate structure.

TABLE 1.1. Chemical bond and its energy strength

Bond	Bond Strength (kJ/mole)
Hydrogen bond (H-O-H)	40
O-H	460
C-H	415
C-C	330
C=C	590
C=O	710
C-O	290

TABLE 1.2. Physical parameters for water and propylene carbonate (20 °C and 1 bar)

	Density (g/cm^3)	Dielectric Constant	Refractive Index	Boiling Point (°C)	Freezing Point (°C)	Heat Capacity ($Jmol^{-1}K^{-1}$)	Surface Tension (mN/meter)	Viscosity (mPa·s)
Water (H_2O)	1.0	80.1	1.33	100	0 °C	75.3	73	1.0
Propylene Carbonate ($C_4H_6O_3$)	1.2	66	1.422	243	-54.5 °C	218.6	42	2.83

Reproduced with permission of the copyright owner. Further reproduction prohibited without permission.

almost as quickly as they form. For this reason, the dielectric constant has a strong dependence on temperature [15]:

$$\varepsilon = 249 - 0.79 \cdot T + 0.00071 \cdot T^2 \qquad 1.1$$

At room temperature, the dielectric constant of water is 80.1. Temperature increase causes a decrease in the dielectric constant, which is unfavorable for applications relying on its dielectric property. In addition, water tends to undergo a temperature dependent ionic dissociation reaction, which leads to a certain number of charge carriers even in pure water. For example, water produces carriers from the reaction:

$$2HOH \Leftrightarrow H_3O^+ + OH^- \qquad 1.2$$

The carrier density from the dissociation reaction is exponentially dependent on temperature [16]. To avoid thermal deterioration of the electrical insulation ability, the use of polar liquids as insulators requires pulsed voltage applications so as to avoid long-term heating and temperature rise.

While water has advantages of low cost, high availability, and ease of handling, it has a high freezing point of 0°C which prohibits its use at lower temperatures. One of the alternative candidates is propylene carbonate ($C_4H_6O_3$); its chemical structure is shown in Fig. 1.1b. It is also a polar liquid and has a dielectric constant of 66. Its freezing point is -54.5°C and the boiling point is 243°C, as shown in Table 1.2. In addition, the heat capacity of propylene carbonate is three times higher than water. These properties make propylene carbonate more tolerable to temperature variations. Thus, propylene carbonate

Reproduced with permission of the copyright owner. Further reproduction prohibited without permission.

could be a better choice than water for energy storage or as an insulation material.

Also shown in Table 1.2, at the same temperature (20°C), pressure (1 bar) and wavelength of illumination (632 nm), propylene carbonate has a refractive index which is only 0.1 larger than water. This means similar optical sensitivity is needed to see refractions in both liquids. With the same optical equipment, this should allow us to detect the disturbance that alters light propagation.

1.2 LIQUID-METAL CONTACT

When liquid and a metal electrode are in contact, the potential difference across the electrode-electrolyte interface immediately causes an electrical double layer. Shown in Fig. 1.2 is a Helmholtz's model that describes the structure of the interface. The interactions between the ions in solution and the electrode surface are electrostatic. The interface remains neutral and the charge held on the electrode is balanced by the redistribution of ions close to the electrode surface. The attracted ions approach the electrode surface and form a layer balancing the electrode charge. This layer can be several nanometers wide. The overall result is two layers of charge (the double layer) and a potential drop confined to this region.

The Helmholtz model provides a basis for physics in the electrode-electrolyte interface region. However, it does not include many factors such as diffusion/mixing in solution, the possibility of absorption onto the surface, and the

Reproduced with permission of the copyright owner. Further reproduction prohibited without permission.

interaction between solvent dipole moments and the electrode. A later model put forward by Stern addresses some of these limitations [17].

The electrical field in the double layer can be very high. It is on the order of 10 MV/cm for a voltage providing a bulk average E-field of 150 kV/cm [19]. This extremely high electric field induces a change in the static dielectric constant. According to Bockris, the dielectric constant in the electric double layer is approximately six or less [20]. Other effects in the double layer are field-enhanced dissociation of the water molecules, field enhanced ionic mobilities, and field-enhanced oxidation and reduction processes [21]. These effects indicate the double layer is a possible site of generation of charged particles with a greater kinetic energy than in the bulk liquid that has a lower electric field.

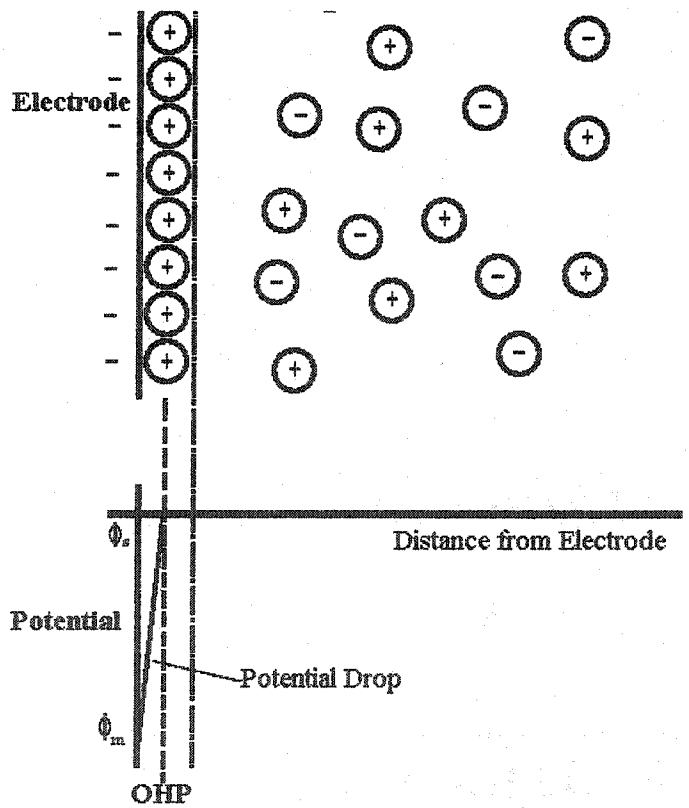

FIG. 1.2. Electrical double layer in the metal-liquid contact [17].

Reproduced with permission of the copyright owner. Further reproduction prohibited without permission.

1.3 ELECTRICAL BREAKDOWN MECHANISMS IN LIQUIDS

Applying a sufficiently high pulsed electrical field to a liquid gap could generate a partial discharge (streamer or corona [22]) or breakdown [23]. Unlike discharges in gas (for example, air, with a density 1/1000 of liquid water), direct electron emission into the liquid is unlikely to cause collisional ionization because the high collision frequency makes it more difficult for electrons to gain sufficient ionization energy along the free path, and they can be easily be trapped by vibrational excitation, attachment, or other processes. The ionization coefficient for electrons in liquids is negligible for the fields at which the breakdown occurs [24]. It is generally accepted that the breakdown initiates from a highly localized, low density region at the electrodes [24-27]. In this region, an electrical discharge occurs which has some of the characteristics of electron avalanches observed in gas discharges.

1.3.1 Vapor Bubble Model

A vapor bubble is one kind of low density region and is a possible site of electrical discharge initiation. It can either pre-exist on the electrodes or be generated in the liquid due to thermal heating after voltage application. When the local temperature becomes higher than the boiling point of the liquid at a given pressure, vapor bubbles begin to appear.

The generation of vapor bubbles at the initial stages of breakdown in liquids was observed experimentally [28-29]. As bubbles are generated, they grow and deform under the electric field. When bubbles achieve a certain size,

Reproduced with permission of the copyright owner. Further reproduction prohibited without permission.

the conditions for gas breakdown are reached. The breakdown of the vapor inside a bubble leads to a local enhancement of the electric field in the surrounding liquid. Under certain conditions, the bubble expands due to the evaporation of adjacent volumes of liquid. Thus, more bubbles are generated and a proceeding breakdown of the liquid dielectric becomes possible [30]. For the onset of breakdown in water, the density needs to be less than some critical value, n_c; for water $n_c = 10^{20}$ cm^{-3} [31]. Also, the bubble size should become sufficiently large for the critical electron avalanche to develop [32]. It was shown that the inception time of the bubble nuclei is the main contribution to the statistical lag time of a breakdown [32].

1.3.2 Crack Model

The crack model, suggests that some low density void or crack is preceding the liquid breakdown [33-34]. The crack differs from the thermal vapor bubble generated by Joule heating in that it is produced by a "cold", electrically induced process.

An electric field induces ponderomotive mechanical force, including Coulomb force, electrophoretic force arising from the non-uniformity of the polarizablity, and a volumetric electrostrictive force arising from a density-dependent permittivity. The field will introduce additional tractions on the interface volume with tensor components $(\varepsilon-\varepsilon_0/2)E^2$ and $-\varepsilon_0 E^2/2$ in the radial and tangential directions respectively. These forces will alter the lateral cohesion of the liquid and lower the tension in an interfacial double-layer at a metal electrode-

Reproduced with permission of the copyright owner. Further reproduction prohibited without permission.

liquid contact. The effect depends on E^2 and acts in a direction orthogonal to electric field and thus tangential to the electrode surface.

For a metal contact in a strong electrolyte, the interfacial double layer thickness may be $<10^{-9}$ m, and since the equilibrium potential difference could be of the order of 1 V, the mean electric field could be as large as 10^9 Vm^{-1}. Under this condition, the change in interfacial tension falls in the range of 0.2–18 mNm^{-1}. The reduction of interfacial tension at an electrode interface is on the order of the surface tension for many liquids. For example, the surface tension of n-hexane is about 18 mNm^{-1}. This means that the cohesion of the liquid, across the electrode surface at the tip where the field is high, will be lost and the liquid molecules will tend to move apart, as shown in Fig. 1.3a. Consequently, cavities (or voids) are likely to form, initially on a sub-microscopic scale, possibly allowing a primary crack to develop. The crack starts along a field line with an axis normal to the cathode surface (Fig. 1.3b). Along the axis, electrons could readily pass from the exposed cathode into the liquid. The electrons will enter the liquid at the outer tip of the primary crack. They then form a highly localized negative space charge there. This will cause a severe distortion of the electric field. As a consequence, a second generation of cracks will appear to form a bush-like extension of the primary crack. Further propagation of the crack is likely to proceed by filamentary crack development into the liquid and finally leads to breakdown. At the anode surface, a similar crack process can occur. In the crack, the accelerated electrons leave positive ions behind to be neutralized by following electrons or

Reproduced with permission of the copyright owner. Further reproduction prohibited without permission.

negative ions. Successive cracks will develop through the field distortion by positive ions and eventually causes the breakdown.

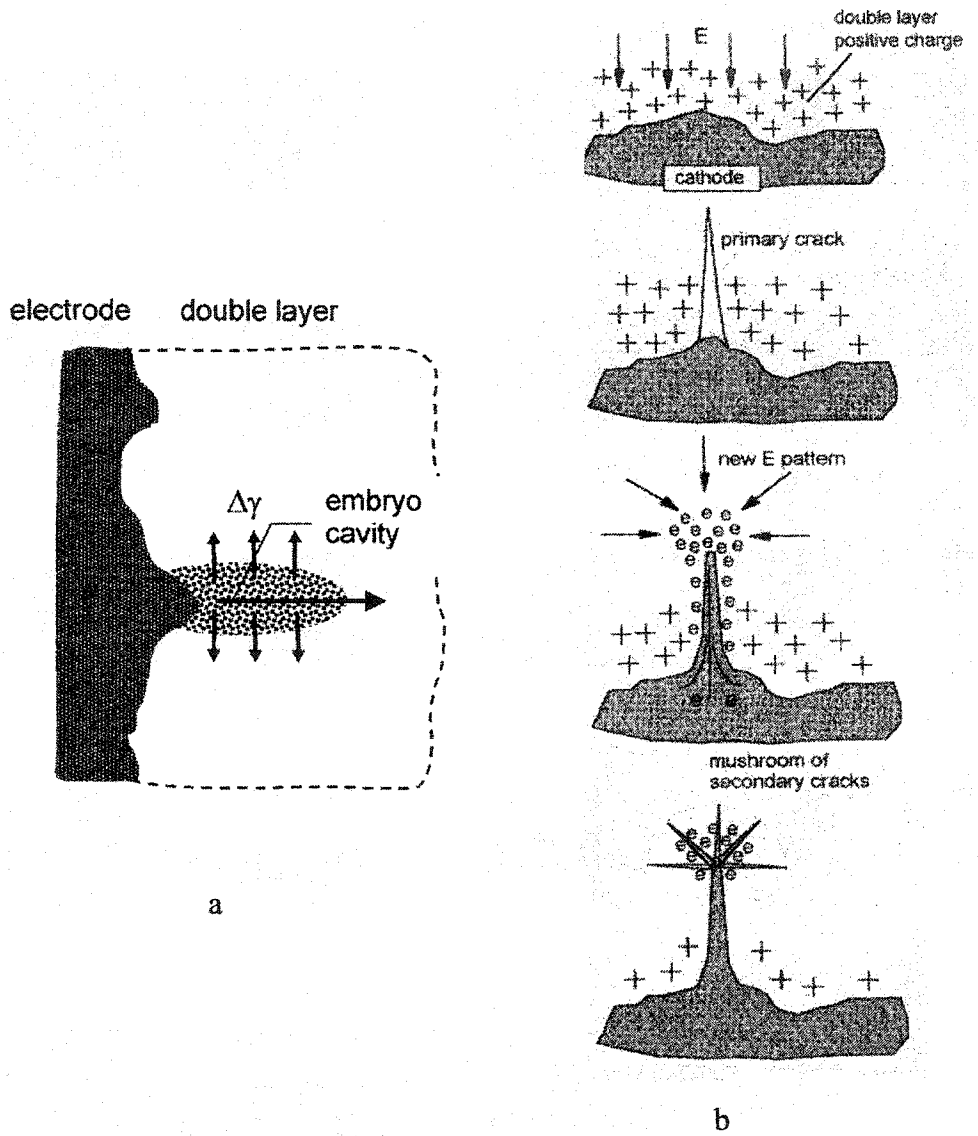

FIG. 1.3. a) Generation of a crack at an electrode asperity as a result of a local reduction in the interfacial tension [34]. b) The primary crack at a cathode surface which indicates the extension of the crack and the field distortion in the head of the crack [33].

Reproduced with permission of the copyright owner. Further reproduction prohibited without permission.

1.3.3 Positive Feedback Mechanism

Joshi et al. investigate a positive feedback mechanism that can be initiated near the electrodes with high electric field [35]. Since the electric field in the metal-liquid contact double layer is very large, the polar molecules will undergo realignment due to the electrostatic interactions. Dipoles are arranged in an orderly way, which reduces the effective polarization of the liquid. This reduction further strengthens the electric field. Through the Monte Carlo simulation of strong field and relative permittivity, it is found that increasing the electric field (10^7 - 10^{10} V/m) results in monotonically decreasing the permittivity. This effect also causes an increase in pressure based on Maxwell stress tensor, which is expanded in the form of shock wave.

Another consequence of the positive feedback mechanism is the enhancement of the current ejection. Since a Schottky-emission current is given as proportional to $K_0\exp[K_1(E/\varepsilon_r)]$, where E is the electric field and $K_{0,1}$ are field-independent constants. An increase of electric field and a decrease of relative permittivity due to the positive feedback mechanism can lead to a large enhancement of the emission current, which may be considered as the prerequisite conditions to the breakdown.

The electron-impact ionization in liquids is unlikely [36]. Instead, the ionization process can happen in randomly distributed gas bubbles. It is argued that at the liquid-bubble interface, a strong electric field may cause field ionization and result in plasma formation and conductivity enhancement. This effect could explain the observed random structure of the streamer.

Reproduced with permission of the copyright owner. Further reproduction prohibited without permission.

1.5 TOPICS OF THE DISSERTATION

The hydrodynamic processes after breakdown in polar liquids are studied in this dissertation. They are of great interest in understanding the breakdown mechanism in dielectric liquids. Moreover, various postbreakdown events provide information about the preceding breakdown. In our study of breakdown, we use submillimeter gaps and non-uniform electrodes. We also choose sub-microsecond pulses generated by a 50 Ω Blumlein line pulse power system, which allows a much higher hold-off voltage and thus a higher breakdown strength than previous breakdown and postbreakdown studies [37-38], in which low electric fields (long gap distance of several millimeter range), long-term stresses, and a large electrode area were used.

We study the postbreakdown phenomena in two polar liquids, water and propylene carbonate. They both have high dielectric constants, allowing their use as an energy storage media. Notably, propylene carbonate has a low freezing point (-55 °C) and is thus capable of being utilized at low temperature. The shock wave emissions, are formed by a fast plasma piston in polar liquids. The spatial and temporal evolutions of shock waves are recorded optically by shadowgraphy and the Schlieren method. Thermal processes due to the plasma heating of the liquids are studied with the same optical approaches. Electrical voltage and current diagnostics measure the electrical properties of the polar liquids during the breakdown. The study of the chronology of the events in water after breakdown is extended to higher energies generated by a 2.5 Ω system.

Reproduced with permission of the copyright owner. Further reproduction prohibited without permission.

The recovery process of liquids after breakdown determines the repetition frequency of the discharges. Compared to the prebreakdown phase in liquids, this subject is less studied. In this thesis, the electric and dielectric recovery in the postbreakdown phase of both water and propylene carbonate are explored.

From the application perspective, liquid breakdown has been studied mainly in very high power systems [39,40]. For example, a water switch in the GAMBLE II generator is capable of delivering 1 MV and 1 MA to the matched load with a risetime of 25 ns [39]. For a breakdown voltage of several tens of kilovolts (gap length ≈ hundreds of micrometers), there are only few experiments reported [35-36]. However, applications for MW pulses in the ns range, at low energy (J) but high repetition rate (kHz), have recently emerged in the new field of bioelectrics [41], and in jet combustion, shock mitigation, and boundary layer control in jet airplanes [42]. Pulsed power systems making use of water as energy storage and switching can meet these power and frequency requirements. For the nanosecond pulse range, charging time is usually in the submicrosecond range. A water gap under a millimeter in distance can hold voltage corresponding to the MW ranges or higher. Thus, the study of water breakdown and postbreakdown processes in submillimeter gaps with short pulse duration (submicrosecond and microseconds) is of interest both for understanding the physics of liquid breakdown and in practical applications.

Reproduced with permission of the copyright owner. Further reproduction prohibited without permission.

CHAPTER II

BACKGROUND

Most of the previous experiments in liquid breakdown were intended to increase the dielectric strength either in energy storage or power switching. Highly purified water is used to reduce the Ohmic loss in the energy storage. The resistivity of water ρ is kept almost near the intrinsic level so as to increase the intrinsic time constant $\tau = \varepsilon\varepsilon_0\rho$. Since the energy density has a power dependence of the electric field ($\propto E^2$), increasing the hold off voltage allows the stored energy to be increased. In addition, when water is used as a switching medium in the spark switch, it shortens the physical length of the spark and eventually reduces the inductance during the switching.

2.1 INITIATIONS OF ELECTRICAL BREAKDOWN IN LIQUIDS

Electrical breakdown in liquid is assumed to start from the low density regions in either a vapor bubble or a crack as described in Section 1.3. Fig. 2.1 shows streamers, the precursors of breakdown in water. Fig. 2.1a-b are the results obtained by a 200 ns pulse [43-44] and Fig. 2.1c is generated by a 100 μs long pulse [45]. It is found that a point electrode with negative polarity has a higher hold-off strength than a positive polarity electrode. All the streamers originate from the point electrode. Obviously, the difference in streamer structure and luminosity depends on the polarity of the electrode. Positive streamers are

Reproduced with permission of the copyright owner. Further reproduction prohibited without permission.

luminous while negative streamers appear as bushy structures and are dark against the bright background. This phenomenon is also observed in gas streamer discharge and is caused by field enhancement in the positive streamer head due to space charge effects [46]. It is also noticed that although several streamers expand and develop, only one streamer leads to breakdown.

It is observed that the bushy structure of the dark negative streamers has a different refractive index than the surrounding water, suggesting the density of the matter in the negative streamers is different from that of the liquid. They could be the vapor bubbles due to thermal heating or cracks caused by cold electric-mechanical force. However, they are not merely low-density regions with densities lower than liquid, because the dark streamers can still withstand the electrical stress and no breakdown has been observed inside the streamers until they touch the opposing electrode. This fact is different from the result in Fig. 2.1c, where a partial discharge occurs inside the "bubble" before it reaches the other electrode. Thus, the bushy structure may be vapor of high pressure or density, or at least with a breakdown strength not lower than the surrounding liquids.

The breakdown precursors generated by the long duration pulse in Fig. 2.1c seem to follow more closely to the conventional bubble model (Section 1.3). However, a discrepancy to the conventional bubble models is observed in the pattern of bubble development: the bubbles are scattered in the liquid without continuous connections with each other. Whereas in the conventional bubble model, vapor bubbles grow in size successively by following their predecessors.

Reproduced with permission of the copyright owner. Further reproduction prohibited without permission.

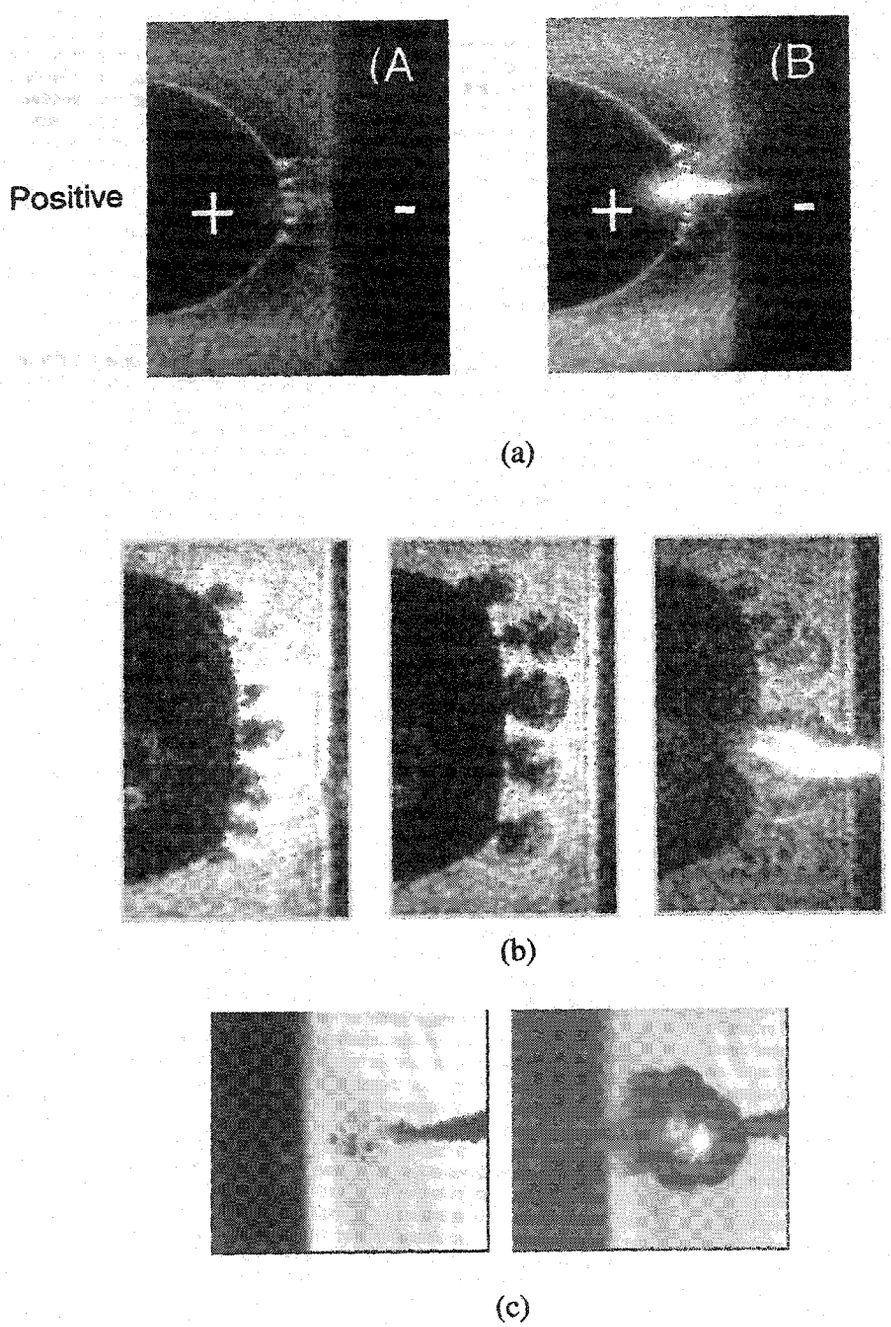

FIG. 2.1. a) Positive streamers and b) negative streamers in the prebreakdown phase generated by applying a 200 ns pulse. c) The breakdown is created by long pulses of several microseconds [43-45].

Reproduced with permission of the copyright owner. Further reproduction prohibited without permission.

In summary, a conclusive description of the nature of the streamers and the formation of these kinds of structures has not previously been developed. A thorough explanation of the breakdown initiations in liquids must address the differences in polarity dependent breakdown field strengths, streamer patterns, and pulsing time effects.

2.2 BREAKDOWN STRENGTH OF LIQUIDS

2.2.1 Scaling of Breakdown Strength

A well-known relation given by J. C. Martin describes the breakdown strength empirically for uniform electrodes based on linear regression [47-48]:

$$M=E_{max}(t_b-t_0)^{1/3}=\text{constant} \qquad 2.1$$

Here, t_0 is a time parameter usually defined as the time when the applied field exceeds some given fraction of its maximum value (e.g., 50%, 63%). The linear regression on the relation (Fig. 2.2) is $t_b= t_0+ (M/E_{max})^3$. The data yield M= 0.562 $(MV/cm)(\mu s)^{1/3}$. This value is close to the value of 0.6 usually quoted for uniformly stressed electrodes. In the experiment, electrodes have large area (300 mm^2) and long gap spacing (2.8-6.4 mm) was set [48]. Martin's relation is a good measure of breakdown in the time region 2-10 μs.

It was found that when asymmetric electrode geometry was used, the breakdown strength is highly dependent on the polarity of electrode. A relation later modified to include area and field enhancement effect gives

$$k_{\pm} = \alpha^{-1}E_{max}t_{eff}^{1/3}A^{n\pm} \qquad 2.2$$

Reproduced with permission of the copyright owner. Further reproduction prohibited without permission.

where A is the effective stressed electrode area (90% of the maximum E-field). The subscript + and – are for positive polarity and negative polarity respectively. For positive breakdown streamers, k_+=0.3, n_+= 0.058. The variable α is related to field enhancement factor. If the field at the negative electrode is increased sufficiently above that of the positive electrode, so that breakdown streamers start from the negative electrode, then the value of k_- is 0.6, n_-=0.069. The coefficients of Eq. 2.1-2.2 can be modified to predict the breakdown strength of different liquids. These relations are empirical laws and no physical interpretations have been given.

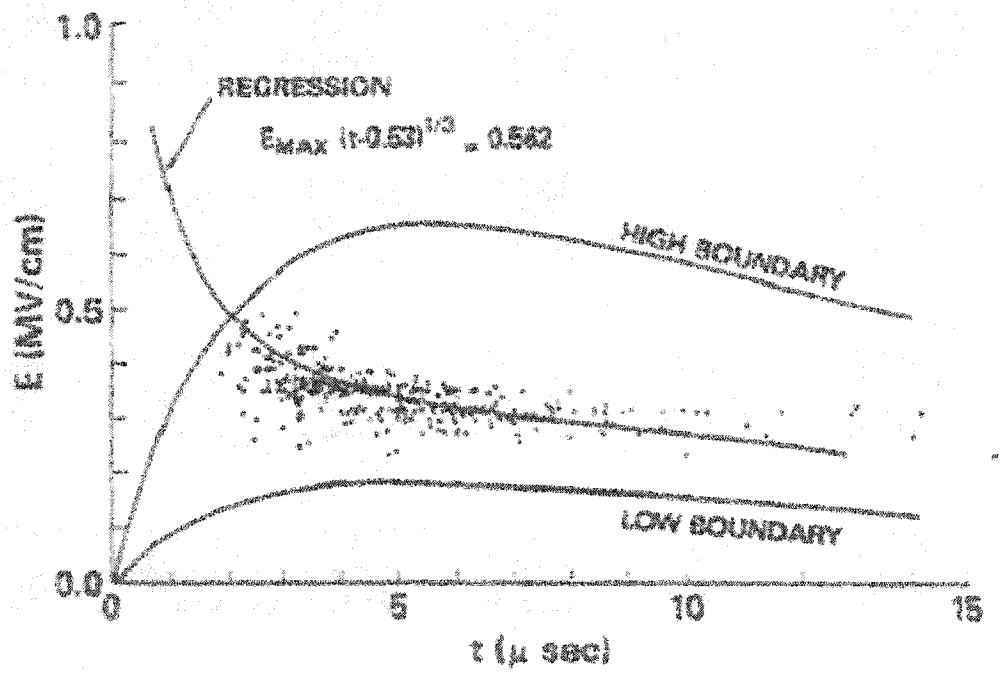

FIG. 2.2. Breakdown strength as a function of time from which Martin's scaling law for uniform electrode discharge is derived [48].

Reproduced with permission of the copyright owner. Further reproduction prohibited without permission.

2.2.2 Factors Influencing Breakdown Strength of Liquids

Liquid breakdown strength is dependent on temperature, liquid resistivity, electrode material, and electrode surfacing among other factors [7,49-54]. These effects are not included in Martin's scaling laws. On the other hand, optimizing these parameters can potentially increase the hold-off voltage of the liquid gap.

Electrode Surface Conditions

Electrode surface roughness was found to have a major effect on hold-off voltage [49]. When the electrode surface is polished to a mirror condition with submicron particle size (Fig. 2.3), the breakdown voltage is improved by approximately a factor of two (200 μm gap). After the first breakdown event causes the appearance of craters, the breakdown strength instantly decreases.

The surface conditioning is related to the microstructures on the electrode, such as the asperities that influence the non-uniformity of the electric field near the electrode. Micro-asperities also determine the field enhancement factor that is attributed to generating a very high electrical field. They are regarded as the field emission current sources. Polishing the electrode surface is expected to remove or reduce the number of asperities and thus lessen the probability of breakdown. The dependence of breakdown strength on electrode area was shown in [50]. When the area was increased by an order of two, the breakdown strength for 1% breakdown probability decreased by a factor of three.

Reproduced with permission of the copyright owner. Further reproduction prohibited without permission.

Hydrostatic Pressure

Extremely high pressures, on the order of thousands of atmospheres, are required to make an appreciable compression of liquids [51]. For example, water only changes its volume by 0.1 percent when the standard pressure (1 bar) is increased by a factor of 25. Therefore, under normal conditions it is possible to treat liquids as incompressible media. However, depending on the amount of dissolved gas in the liquid and adsorbed gas on the electrodes, pressure could influence the breakdown strength. It has been shown that a 9% increase in the breakdown strength occurs by varying the pressure from 0 to 30 psig (2.1 bar) (Fig. 2.4) [52]. In another experiment, the breakdown voltage was increased by a factor of 5 when the pressure was increased to 150 atm [7]. These results support the formation of gaseous bubbles in the prebreakdown process, which are sensitive to pressure since bubble expansion is dependent on pressure. The propagation velocity of the breakdown precursor, a streamer, was reduced by a factor of three when the hydrostatic pressure was increased from 5 MPa to 30 MPa [53].

Resistivity of Liquid

The resistance of a liquid is governed by the ionic current contribution in the prebreakdown phase. Field-enhanced dissociation (Onsager theory [21]) or ion injection at the electrode will likely dominate the ion production. Electric field distribution may be altered by the space charge effect of ions in the liquid bulk, and especially in the double layer. The electronic scavenger additive results in an

Reproduced with permission of the copyright owner. Further reproduction prohibited without permission.

increase in the average streamer propagation velocity, and the streamers become more luminous [54]. After breakdown, the thermal radiation shows a temperature of approximately 1 eV [56-58, also see Appendix A].

Various experimental data have covered resistivities from 2 - 3 $\times 10^7$ Ωcm to several kΩcm. It has shown that adding salt solution through an electrode grid into the main inter-electrode region increases the breakdown strength by a factor of three [7]. This indicates that Joule heating doesn't play a role. It was shown that the field irregularities on the surface are smoothed out by gradual distribution of high conductivity over a region of approximately 1 mm in thickness adjoining the surface. A similar tendency is observed in tap water compared to distilled water (Fig. 2.5) [49]. The breakdown strength increases from 1.6 MV/cm to 2 MV/cm when the resistivity was decreased from 400 kΩcm to 7 kΩcm.

Reproduced with permission of the copyright owner. Further reproduction prohibited without permission.

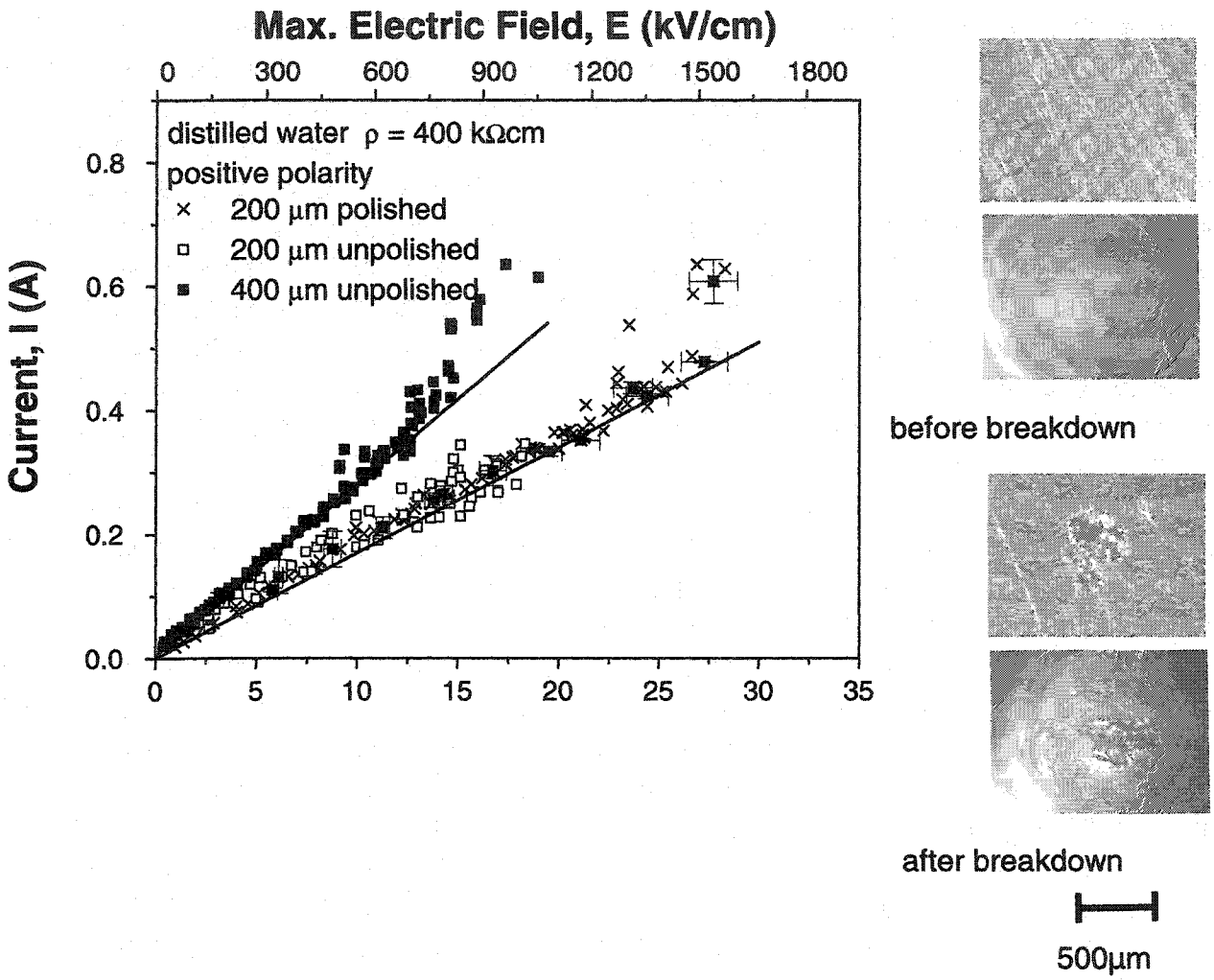

FIG. 2.3. Current-voltage characteristics for polished and unpolished electrodes [49].

Reproduced with permission of the copyright owner. Further reproduction prohibited without permission.

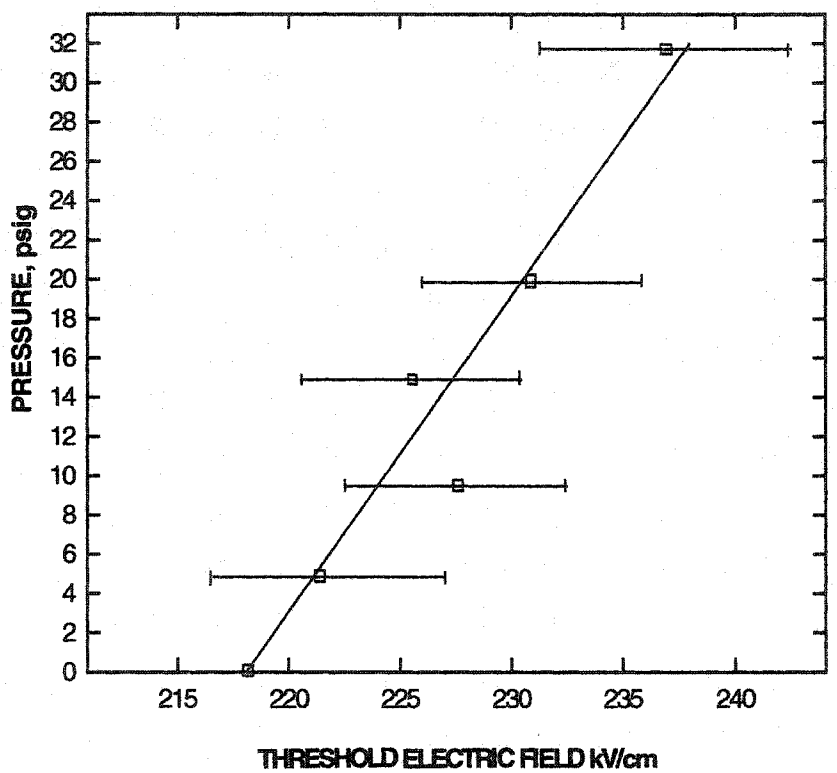

FIG. 2.4. Breakdown strength increases as the applied pressure increases [52].

Reproduced with permission of the copyright owner. Further reproduction prohibited without permission.

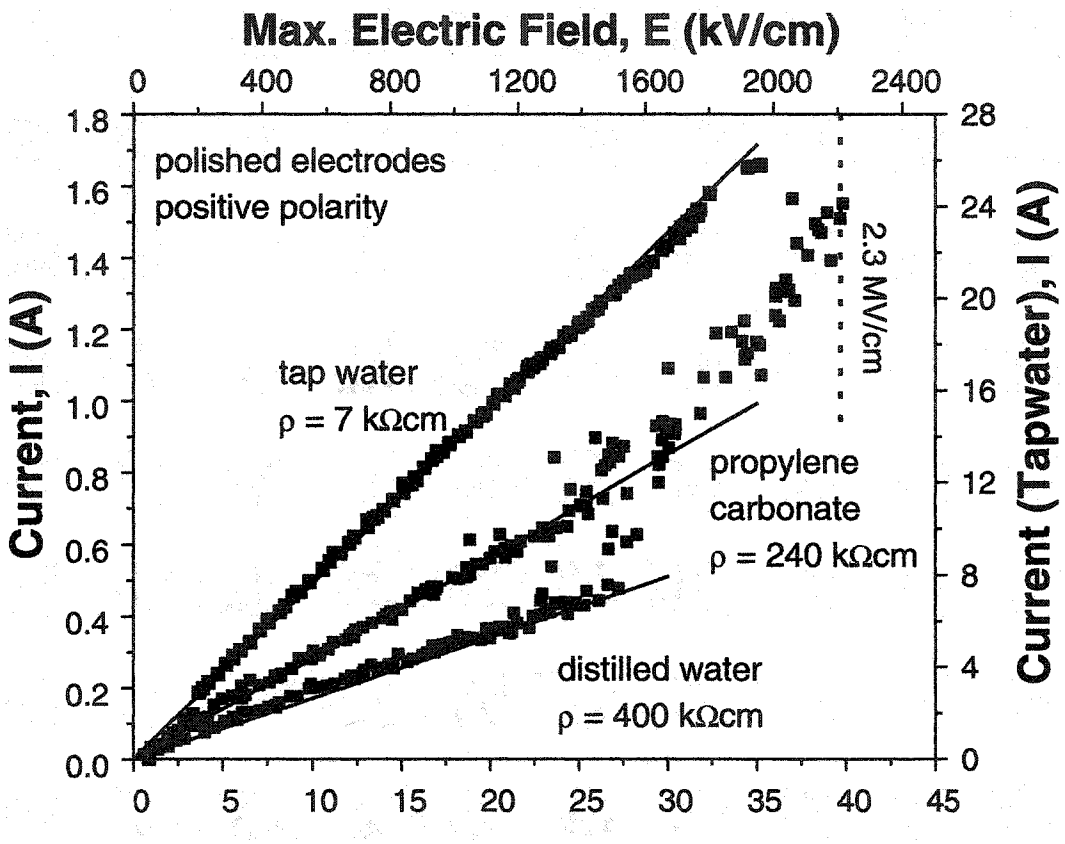

FIG. 2.5. Current voltage characteristics of tap water, distilled water and propylene carbonate for polished electrodes and positive polarity [49].

Reproduced with permission of the copyright owner. Further reproduction prohibited without permission.

CHAPTER III

EXPANSION OF PLASMA PISTON AFTER LIQUID BREAKDOWN

The hydrodynamic process following the breakdown in liquid has been described by several models [32,59-62]. For example, Jones and Kunhardt describe the establishment of the conduction channel in terms of the propagation of the ionization front, heating of the region ahead of the front, and ionization growth at the front [32]. Based on a similar physical process, another model includes chemical reactions such as water dissociation [59]. There is a model attempting to scale the arc formation in liquids from the equation of state for a plasma-liquid mixture [60]. In addition, numerical fluid models exist to include the energy balance for very high voltage and very low current water breakdown that have shown good agreement with experimental results [61-62]. Indeed, once the conduction channel in water is formed, the physics should be similar to that of a spark in gas. Braginskii's models, and other models based on it, were successfully applied to describe gas channel expansion [63-64]. It assumes that a comparatively narrow current-carrying channel exists first, which could be caused by the propagation of an ionization front along the axis. This channel reaches a high temperature and consequentially high ionization rate. Joule heating is released in the channel, which then leads to an increase in the pressure and an expansion of the channel. The thickened channel acts like a piston on the remaining gas and, since the expansion takes place with a supersonic speed, it produces a shock wave in the gas. This shock is propagated

Reproduced with permission of the copyright owner. Further reproduction prohibited without permission.

in front of the original "piston". The difference in a water spark lies in the interfacial property, i.e. the plasma-liquid thermal transportation process. The temperature gradient in the layer creating heat conduction, convection, and mass transfer make the size and conductance of the spark nonlinear, an important property in the behavior of its expansion.

3.1 SHOCK WAVE FORMATION

Fig. 3.1 shows how the supersonic motion of the piston creates a shock wave (compression wave). Here a plasma piston accelerates into a static gas (or liquid). Along this acceleration path, the gas flow starts to move at the piston's velocity. Each pressure wave is sent out at the local sonic velocity with respect to the gas through which it passes. However, the masses nearest the piston have both a higher velocity and a higher temperature (due to higher pressures) and consequently much higher pressure-wave speed than masses do further away. Eventually the pressure waves nearer the piston catch up and even overtake those further downstream until all the pressure waves coalesce and form a single steep pressure gradient, or shock wave [65]. This gradient leads to discontinuities of velocity, density, temperature and specific entropy.

The physical model that describes the development of the spark channel can be treated as a shock tube problem, as shown in Fig. 3.2. At time $t = 0$, there is a contact surface that separates the plasma and water region. At $t > 0$, the current increases, more energy releases in the channel, and a spherical shock wave is sent out, followed by the contact surface. Behind the contact surface, a

Reproduced with permission of the copyright owner. Further reproduction prohibited without permission.

rarefaction wave moves toward the opposing direction, lowering the density and pressure in the center of the plasma.

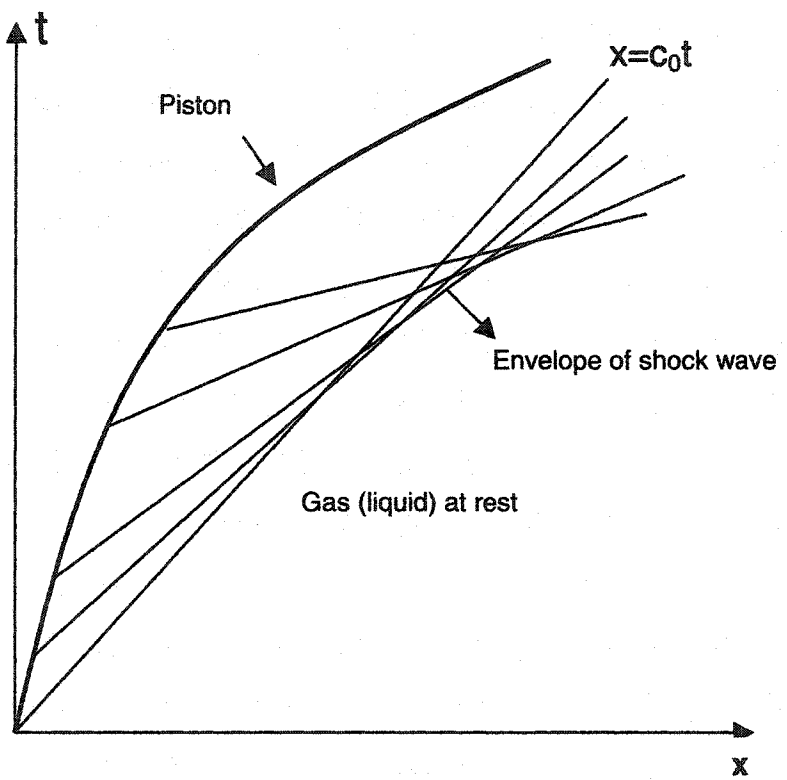

FIG. 3.1. Shock wave envelope produced by a uniformly accelerated piston [65].

Reproduced with permission of the copyright owner. Further reproduction prohibited without permission.

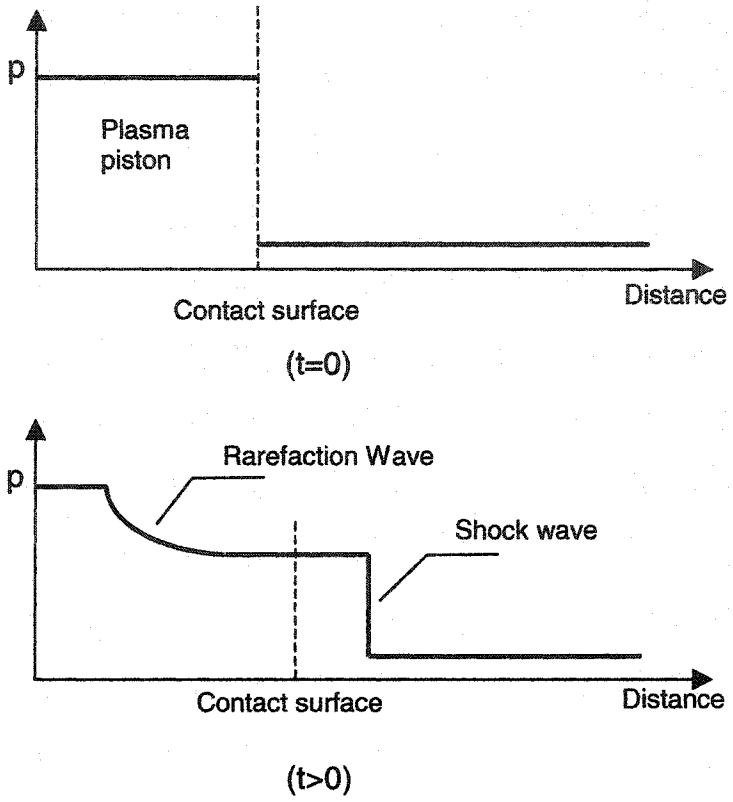

FIG. 3.2. Shock wave emission followed by a contact surface which separates the liquid and plasma.

3.2 SHOCK FRONT EXPANSION

The problem of describing a shock tube in a hydrodynamic fluid with discontinuity can be completely illustrated by three conservation equations and entropy conditions [66, and also see Appendix B]. We shall not proceed to solve the equations, but rather we pursue a simpler solution considering the conservation laws near the boundary and a similar derivation that can be found in Zahn [67]. In this case, the Joule heating source is neglected. We also assume the thermal parameters such as pressure and temperature have a large gradient along the radial direction, i.e., strong shock condition. Although a transition is

Reproduced with permission of the copyright owner. Further reproduction prohibited without permission.

presented in the early phase of the plasma, before energy is released entirely, this assumption is still valid when a shock wave is moving out of the plasma region.

At the shock wave boundary, the Rankine-Hugoniot (R-H) condition states that mass, momentum, and energy must all be conserved:

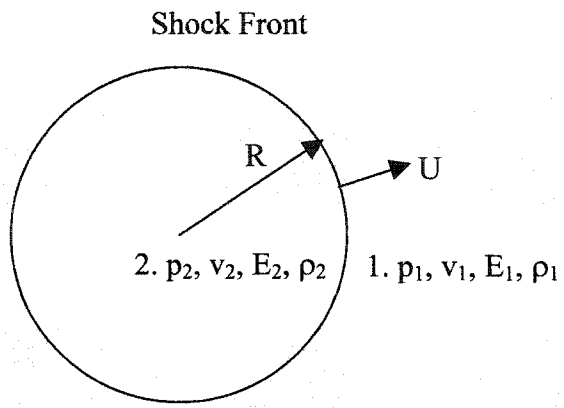

FIG. 3.3. Boundary of a shock wave, which separates the ambient state and the high pressure region, during the expansion.

The rate of mass flow away from the shock should be equal to the rate of mass flow into the shock:

$$\rho_1 (U-v_1) = \rho_2 (U-v_2)=m \qquad 3.1$$

where U= dR/dt, the shock velocity.

The momentum conservation reads:

$$p_1-p_2 = m(v_1 - v_2) \qquad 3.2$$

and, energy writes:

$$m[(v_1^2/2) +E_1]- m[(v_2^2/2) +E_2]= p_1v_1-p_2v_2 \qquad 3.3$$

Reproduced with permission of the copyright owner. Further reproduction prohibited without permission.

where $E = C_v T = p/\rho(\gamma-1)$ is the internal energy per unit mass, γ is the specific heat ratio, and the magnitude of γ for dissociated and ionized gas is determined primarily by the temperature and density. The determination of γ is rather difficult. Here, we follow Ya et al., and assume $\gamma=4/3$ in which it is assumed that translational and rotational energy is dominant [51].

When assuming a strong shock limit (where $p_2 >> p_1$, $v_2 >> v_1$), R-H conditions yield:

$$\rho_2 = \rho_1 (\gamma+1)/ (\gamma-1) \qquad 3.4$$

$$p_2 = [2\gamma/(\gamma+1)]p_1(U/c_1)2 = 2\rho_1 U /(\gamma+1) \qquad 3.5$$

$$v_2 = 2U/(\gamma+1) \qquad 3.6$$

where it is assumed that the speed of sound in the undisturbed liquid is given by $c_1 = (\gamma p_1/\rho_1)^{1/2}$.

The energy per unit length (along the spherical axis) behind the shock wave is then:

$$E = 4\pi \int_0^{R(t)} \rho(C_v T + v^2/2) r^2 dr = 4\pi \int_0^{R(t)} \left(\frac{p}{\gamma-1} + \rho\frac{v^2}{2}\right) r^2 dr \qquad 3.7$$

The following non-dimensional variables are introduced:

$$\xi = r/R(t) \qquad 3.8$$

$$\rho = \rho_1[\chi(\xi)] \qquad 3.9$$

$$v = (aR/t)V(\xi) \qquad 3.10$$

$$p = (aR/t)^2 (\rho_1/\gamma)P(\xi) \qquad 3.11$$

Reproduced with permission of the copyright owner. Further reproduction prohibited without permission.

To match these trial solutions with the Rankine-Hugoniot equations, they need to be equated at the shock front (ξ=1). Combining the expression for v in Eq. 3.6 and Eq. 3.10, yields a differential equation for the radius:

$$U = dR/dt = aR/t \tag{3.12}$$

with a solution, $R=\alpha t^a$

In terms of these new functions shown in Eqs. (3.8-3.11), the total energy per unit length may be written as:

$$E = 4\pi \frac{a^2 R^5}{t^2} \rho_1 T(\gamma) \tag{3.13}$$

where:

$$T(\gamma) = \int_0^1 [\frac{P(\xi)}{\gamma(\gamma-1)} + \frac{\chi(\xi)}{2} V^2(\xi)]\xi^2 d\xi \tag{3.14}$$

Assuming that once the energy deposited in the breakdown channel (gas column), it remains constant, we then have:

$$R^5/t^2 = \alpha^5 t^5 a/t^2 = \text{constant} \tag{3.15}$$

This requires 5a=2. Now:

$$a=2/5=0.4 \tag{3.16}$$

$$\alpha=[E/4\pi\times 0.16\rho_1 T(\gamma)]^{1/5} \tag{3.17}$$

A numerical integration provides $T(\gamma)$ near 0.5 for γ = 4/3, so we have:

$$R=\alpha t^a \tag{3.18}$$

where, $\alpha=(E/\rho_1)^{1/5}$ and a=0.4.

A similar relationship was developed by Sedov through a similarity and dimensional method, which successfully predicted various phenomena including

Reproduced with permission of the copyright owner. Further reproduction prohibited without permission.

a nuclear bomb shock [68]. We shall see that the expansion of a shock wave in water can be satisfactorily described by this law.

Reproduced with permission of the copyright owner. Further reproduction prohibited without permission.

CHAPTER IV

EXPERIMENTAL SETUP

To study the hydrodynamic phenomena and dielectric recovery after electrical breakdown in polar liquids, we have used pulse power systems, which allow the generated voltages to exceed the breakdown voltage of the liquids for asymmetrical submillimeter gaps. Two pulsed power systems provide short electrical pulses of submicrosecond (50 Ω), as described in [69] and long electrical pulses of several microseconds (2.5 Ω).

4.1 50 Ω SYSTEM

4.1.1 Pulsed Power System

The pulse forming line (PFL) provides a 200 ns pulse to water gap under matched conditions (Fig. 4.1). The PFL consists of two coaxial cables (RG-217, 50 Ω) in parallel, arranged in a Blumlein configuration, as shown in Fig. 4.1. The matched load has an impedance of 50 Ω. The PFL is charged by means of a DC high voltage power supply (Hipotronics, maximum voltage 30 kV) through a charging resistor of 100 MΩ. The charging time constant of the PFL is 0.8 second. The energy stored in the PFL is transferred to the water gap by means of a spark gap switch in atmospheric pressure air. The pulsed resistance of the water gap, measured for distilled water, is 56 kΩ for a pulse duration of 200 ns, which is large compared to the impedance of the PFL. The system is

Reproduced with permission of the copyright owner. Further reproduction prohibited without permission.

consequently mismatched before breakdown, and the voltage across the gap is twice the applied voltage. A 50 Ω resistor is placed in series to the water gap. As long as the gap does not break down, it has little effect on the voltage across the gap and the current flowing through it. However, after breakdown, when the water gap drops to a value small compared to 50 Ω, the load resistor (50 Ω) serves as matching resistor for the pulse power circuit and determines both current and pulse duration after breakdown.

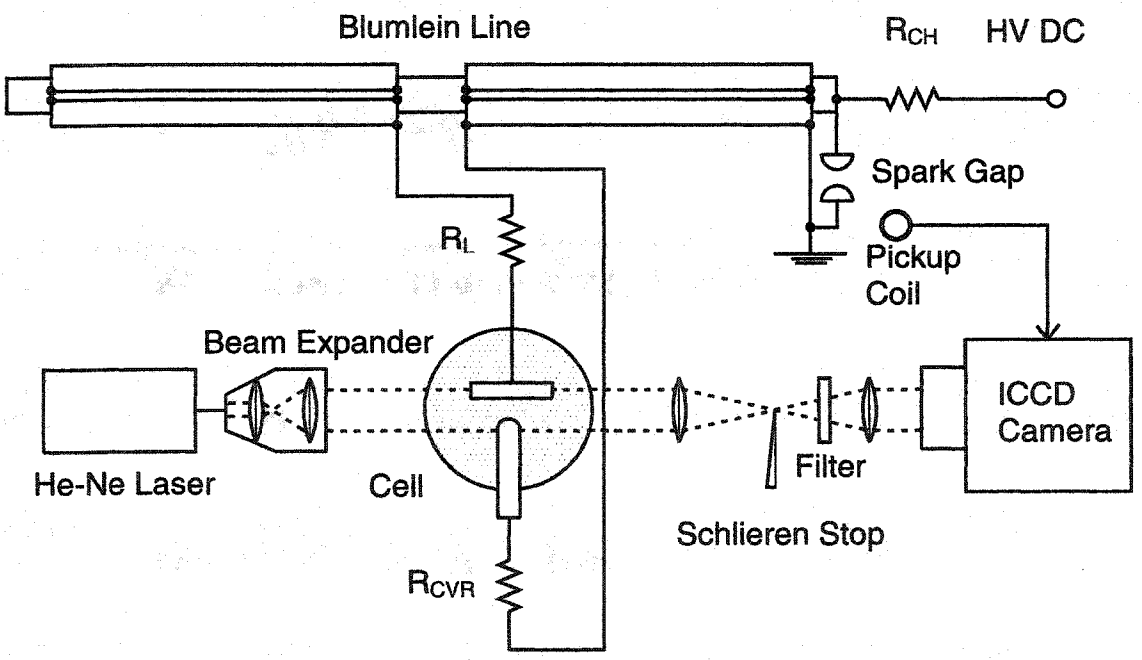

FIG. 4.1. Electrical circuits and optical setup. The Blumlein line consists of two cables (RG –217, 50 Ω, 20 m) in parallel, charged with a resistor R_{CH} of 100 MΩ. The Blumlein generator produces a 200 ns pulse of 30 kV amplitude with a matched load R_L of 50 Ω. The current viewing resistor R_{CVR} has a value of 1 Ω.

Reproduced with permission of the copyright owner. Further reproduction prohibited without permission.

4.1.2 Discharge Cell

The discharge cell for the experiment is shown in Fig. 4.2. We have used an electrode configuration that consists of a plane electrode which in the experiments served as cathode and a rod electrode with a hemispherical shape (radius = 0.85 mm) facing the planar electrode, as previously described in [43-44]. Both electrodes are made of stainless steel. The gap distance can be adjusted up to 1 mm with an accuracy of 5 μm. The two electrodes are placed in a water-filled stainless steel chamber with a water inlet and outlet, and with electrical connections for high voltage and electrical diagnostics. The chamber has two quartz windows for optical access. Distilled water is used with a resistivity in the range of 2-4 $\times 10^5$ Ωcm. The water between the electrodes is replaced after each electrical breakdown.

Reproduced with permission of the copyright owner. Further reproduction prohibited without permission.

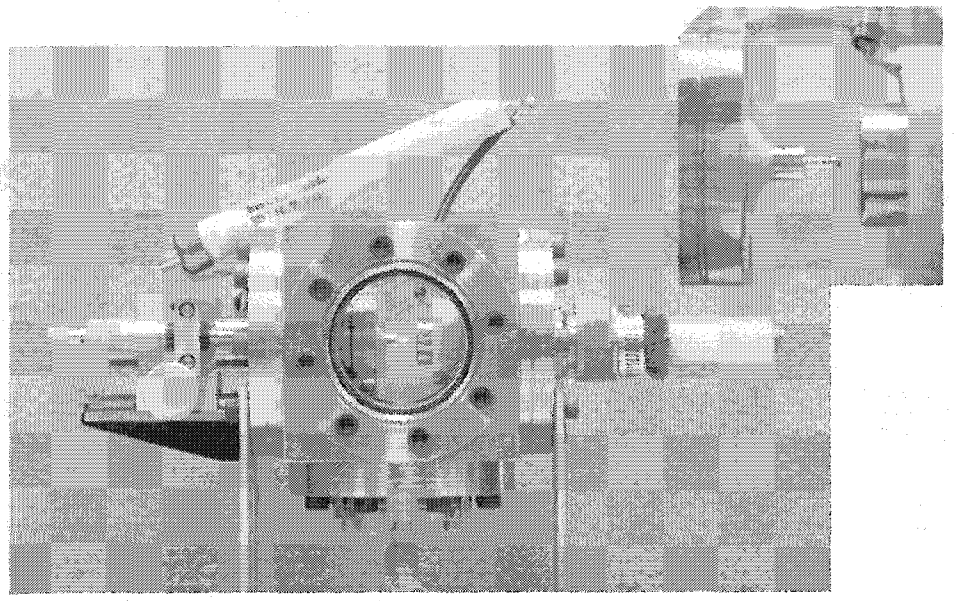

FIG. 4.2. Discharge cell. The electrodes are rod and plane shape. High voltage feedthrough (RG 220) is connected with plane electrode. The rod electrode is grounded. The gap distance is adjusted through a micrometer which is coupled with the rod electrode. The cell has windows on both sides for optical access. Also shown in the figure is a high voltage probe [43].

Reproduced with permission of the copyright owner. Further reproduction prohibited without permission.

4.1.3 Flow Systems

To remove the debris generated by the previous discharge, we include a flow system which allows us to replace the interelectrode volume. We use two types of electrode systems, allowing both transverse flow and axial flow (Fig. 4.3). For the transverse flow system, we introduce the liquid by a side-on nozzle. The nozzle is 1.8 mm in diameter with a distance of 3 mm from the rod-pin electrodes. The rod electrode has a semi-spherical shape with a diameter of 1.75 mm; the pin electrode is 1.3 mm in diameter and has a flat top. The second flow is realized by guiding the liquid through a nozzle electrode. The nozzle has an inner diameter of 0.76 mm. The other electrode is a pin electrode and has a diameter of 0.5 mm at the tip.

A high pressure pump (Kacher) is used to pressurize water with a resistivity of 4-5 kΩcm. For both flow methods, a by-pass valve is used to adjust the flow speed. The flow pattern can be changed from laminar to turbulent depending on the flow rates.

Reproduced with permission of the copyright owner. Further reproduction prohibited without permission.

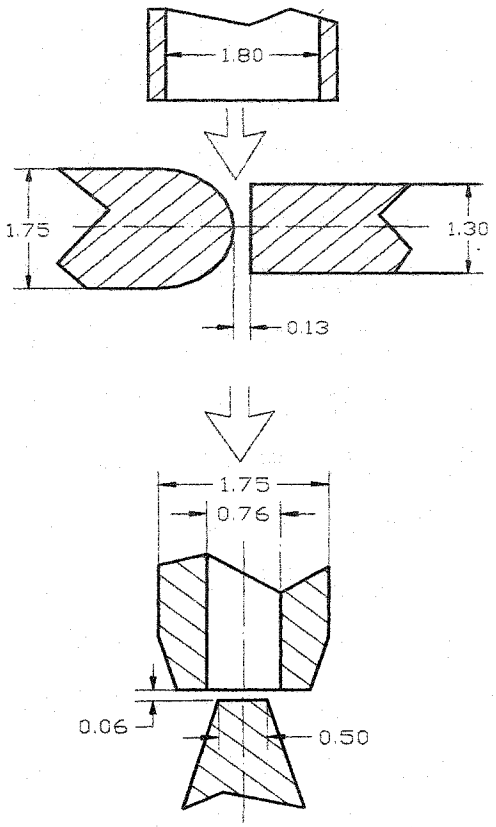

FIG. 4.3. Flow systems. Top: transverse flow is introducing from side-on by a nozzle 3 mm away. Pin and rod electrode are used with a distance 0.13 mm. Bottom: axial flow is guided by nozzle electrode to flush a pin electrode.

4.2 2.5 Ω SYSTEM

The second system operates at energies up to 50 J. We use an all water pulse power generator (Fig. 4.4-4.5). In this system, water serves as an energy storage medium and switching medium as well. The water gap serves as a

Reproduced with permission of the copyright owner. Further reproduction prohibited without permission.

closing switch for the PFL. After the water gap closes, most of the electrical energy stored in the PFL delivers to the matched load.

4.2.1 Water Pulse Forming Line

The water PFL is designed with a coaxial structure. The impedance of the line is determined by the water's dielectric constant and the distance between the outer conductor and the inner conductor:

$$Z_0 = \frac{138}{\sqrt{\varepsilon}} \log_{10} \frac{D}{d} \qquad 4.1$$

The outer radius of the inner conductor is 2", and the inner radius of the outer conductor is 2.76". This yields an impedance of 2.5 Ω. Both cylindrical conductors are weldless stainless steel. The length of the water-filled PFL is approximately 152 centimeters. The length of the pulsed forming line determines the pulse length of the generated pulse when switch is closing. In our system, it is approximately 100 ns. To reduce the Ohmic loss during charging, we use deionized water with resistivity on the order of MΩcm.

Reproduced with permission of the copyright owner. Further reproduction prohibited without permission.

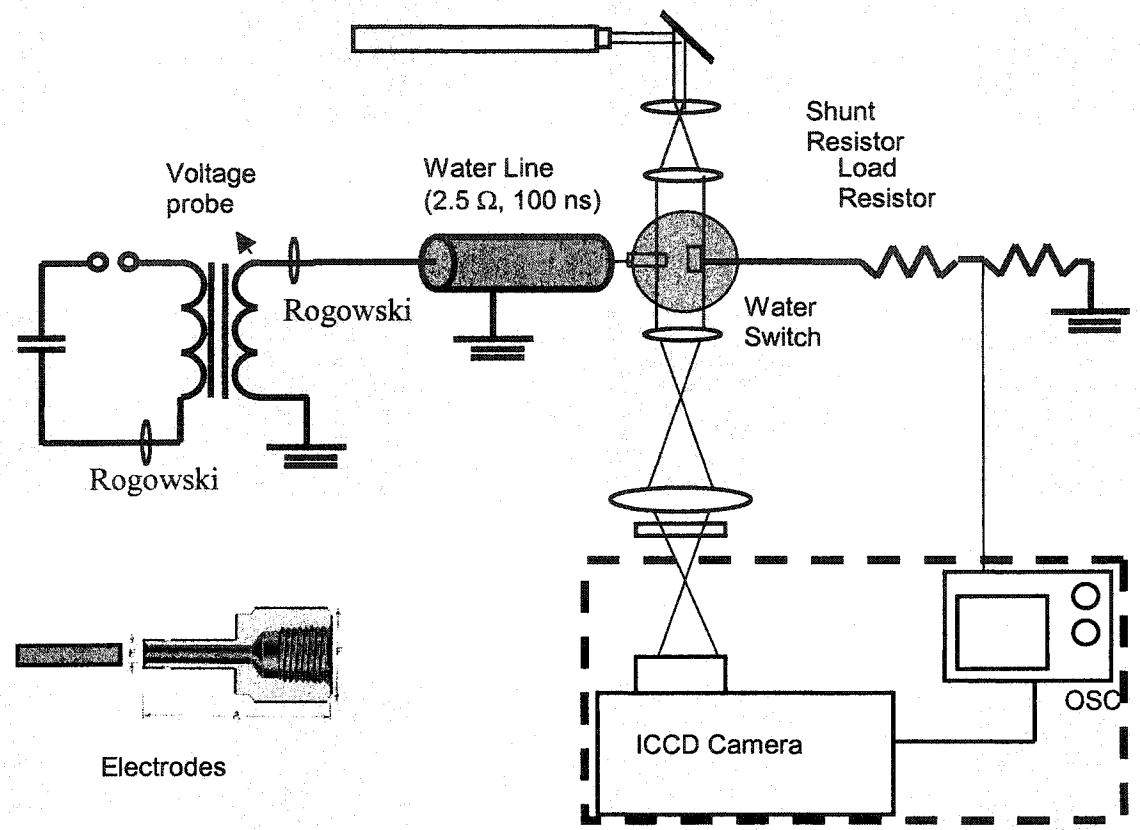

FIG. 4.4. All-water pulse power system consists of a water pulse forming line (2.5 Ω) and a water switch. The PFL is charged by a resonant charging circuit with a pulsed transformer. The water switch has electrodes of pin and nozzle. The optical diagnostic is shadowgraphy through a triggered, fast ICCD camera.

Reproduced with permission of the copyright owner. Further reproduction prohibited without permission.

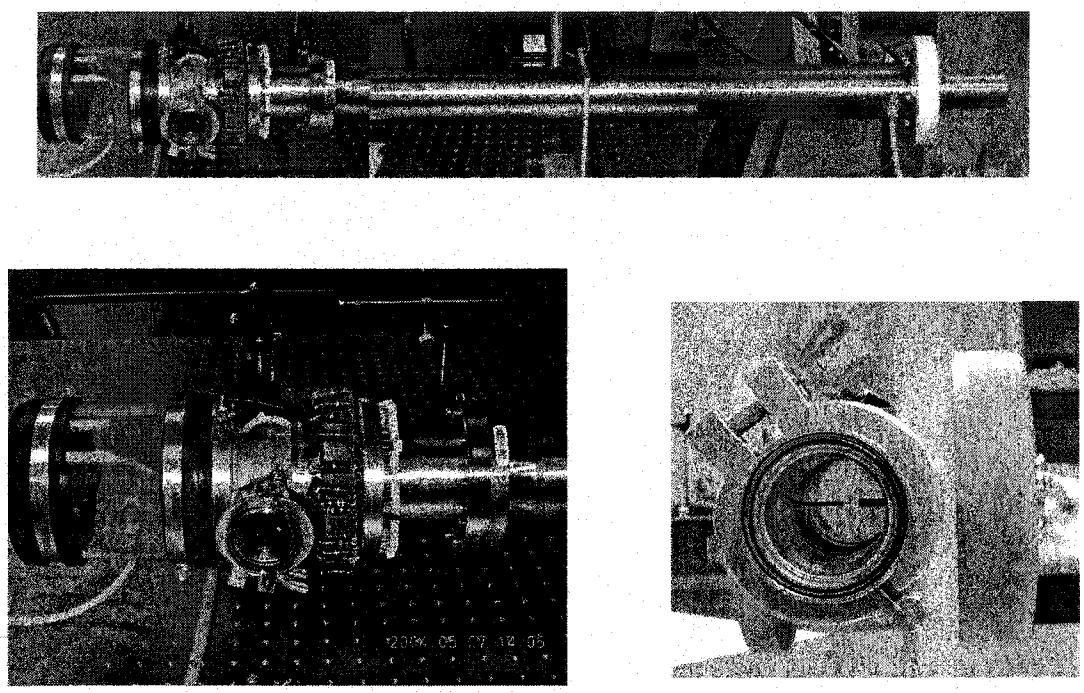

FIG. 4.5. Physical setup of the all water pulse power system. Top: the overview of the pulse forming line, water switch and load. Bottom left: water reservoir, water switch and load resistors. Bottom right: water gap.

Reproduced with permission of the copyright owner. Further reproduction prohibited without permission.

4.2.2 Resonant Charging System

The PFL is charged by a resonant charging circuit through a 1:8 transformer (coupling coefficient k = 0.8) by discharging the primary capacitor bank (2.1 μF) through a closing spark gap. The resonant charging circuit is optimized so as to achieve a high charging efficiency. A resonant condition is realized by insuring [73]:

$$L_1C_1=L_2C_2, \qquad 4.2$$

Where L_1 is the primary inductance of the transformer (25 μH), C_1 is the capacitance of the capacitor bank (2.1 μF). L_2 is the secondary inductance of the transformer (2.1 mH), C_2 is the capacitance of the pulsed forming line (25 nF). The charging period is determined by $\omega=1/(L_1C_1)^{0.5}$ and the coupling coefficient k. In our experiments, the charging period is eight microseconds (one quarter of the charging period). A typical charging current is compared to a simulation in Fig. 4.6. A good agreement is achieved in the first quarter of the charging phase. As time extends, the Ohmic heating effects may alter the dielectric capacitance of the water PFL and voltage finally damps due to Ohmic loss in the line. When voltage reaches the peak magnitude, the water gap breaks down at a self-breakdown mode. The system can be charged up to a voltage of 90 kV, corresponding to 100 J stored in the PFL. To match the impedance of the PFL, load resistors are built with fifty low inductance carbon composite resistors (50 Ω, 2 W) connected in parallel. The total resistance is 2.5 Ω.

Reproduced with permission of the copyright owner. Further reproduction prohibited without permission.

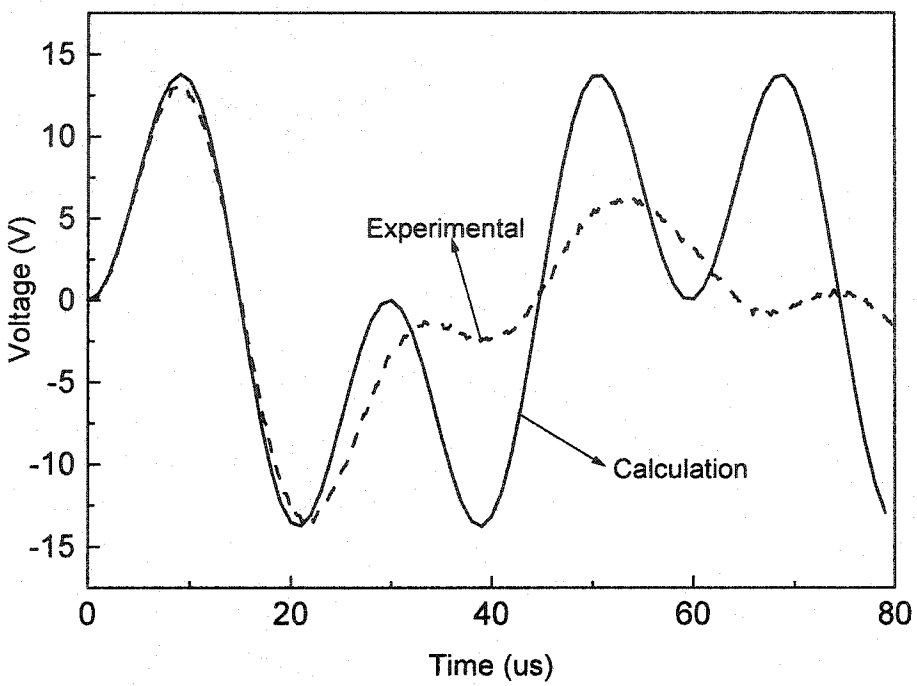

FIG. 4.6. Measured charging voltage pulse versus simulation results. This is based on 1.5 kV charging voltage. The parameters of the circuit are: k=0.8, L_1=25 μH, L_2=2.1mH, C_1=2.1 μF, C_2=25 nF.

4.2.3 Discharge Cell

The electrode geometry of the switch gap consists of a pin electrode 1.85 mm in diameter facing a nozzle electrode that allows flow water through the gap. The nozzle has an inner diameter of 2.0 mm, outer diameter of 2.88 mm, and serves as the anode. The high voltage pulse is applied to the nozzle. For all experiments, distilled water is used.

Reproduced with permission of the copyright owner. Further reproduction prohibited without permission.

CHAPTER V

DIAGNOSTICS

5.1 VOLTAGE AND CURRENT MEASUREMENTS

The voltages applied to the gaps in liquid discharges are measured by commercial high voltage probes (North Star Research Co. 200:1, 250 MHz and Tektronix P6015 A, 1000:1) and a self-made high voltage divider. Commercial probes allow us to measure the voltages up to 40 kV, which are mainly used in 50 Ω systems. We also use a self-made voltage probe to measure the voltages in the 2.5 Ω system. It is a resistor divider consisting of low-inductance carbon-film resistors and allows us to measure voltages up to 100 kV.

To measure the current flowing through the gaps, we use shunt resistors, which are in series with the discharge gaps. The current across the gaps is measured by picking up the voltage drops across the shunt resistors. They have a very low resistance (<=1 Ω) to avoid influencing the impedance of the circuit. For the current measurement in 2.5 Ω system, the shunt resistors are consist of 100 low inductance resistors, each with resistance of 2.2 Ω.

5.2 ELECTRICAL DIAGNOSTICS FOR VOLTAGE RECOVERY

To determine the dielectric recovery of the water gap, a pulse-probe system is used (Fig. 5.1). This system generates two voltage pulses with the first pulse causing the water breakdown and the second pulse measuring the dielectric strength of the water. A PFL with coaxial cables as energy storage

Reproduced with permission of the copyright owner. Further reproduction prohibited without permission.

elements (RG 214, 50 Ω, 4 m) and a spark gap switch is used to generate a rectangular voltage pulse of 40 ns across the water gap. Before water breaks down, this load is not matched to the PFL due to the high resistance of the water gap. After water breakdown, however, with the resistance of the water gap decreasing to values small compared to 50 Ω, the load resistor (50 Ω) in series with the water gap serves as matching resistor. This limits the current pulse after breakdown to 40 ns, as determined by the length of the cables. The second pulse is generated by a commercial high voltage generator (Maxwell 40330), which is triggered by a delayed pickup signal from the spark gap. The voltage generator is capable of generating the same magnitude in voltage as the first generator. The second pulse is applied to the water gap with a delay time varying from 250 μs to 100 ms, corresponding to a pulse rate of 4 kHz to 10 Hz. Since the voltage of the second pulse across the water gap is determined by the conductance of the water, the value of the measured voltage serves as a measure for the recovery of the water gap. The degree of recovery is defined as the ratio of the breakdown voltage of the second pulse to the breakdown voltage of the unperturbed water. Complete recovery is achieved when the second pulse voltage reaches the same magnitude in breakdown voltage as the first pulse.

We also use an alternative pulse-probe system (shown in Fig. 5.2) to study the dielectric recovery phenomena. A pulse is first generated by a Blumlein line pulser consisting of two RG-8 cables (50 Ω, 12 m) in parallel, charged by a high voltage DC power supply (Glassman, <20 kV). A spark gap switch is used as a closing switch to produce a 120 ns pulse. A pickup coil close to the spark

Reproduced with permission of the copyright owner. Further reproduction prohibited without permission.

gap generates a trigger signal for the second pulse generator. The delay is variable from 250 μs to 10 ms by a delay generator. The second pulse is generated by a resonant charging circuit consisting of a 4 nF capacitor and a 58 μH inductor. The capacitor is charged by a second high voltage DC power supply (Bertan, <30 kV) and discharged by closing a trigatron switch with a jitter of less than 200 ns. An exponential waveform with a risetime of several hundred nanoseconds is generated when the trigatron switch closes. The two pulse circuits are decoupled by a high voltage diode. A load resistor R_L (50 Ω) is connected in series with the water gap. Eight low-value carbon resistors in parallel are used as a shunt resistor R_{CVR} (0.3 Ω) to measure the current. The voltage applied to the gap is measured by a Tektronix high voltage probe and recorded by a Tektronix oscilloscope (TDS 3052, 1000:1).

Reproduced with permission of the copyright owner. Further reproduction prohibited without permission.

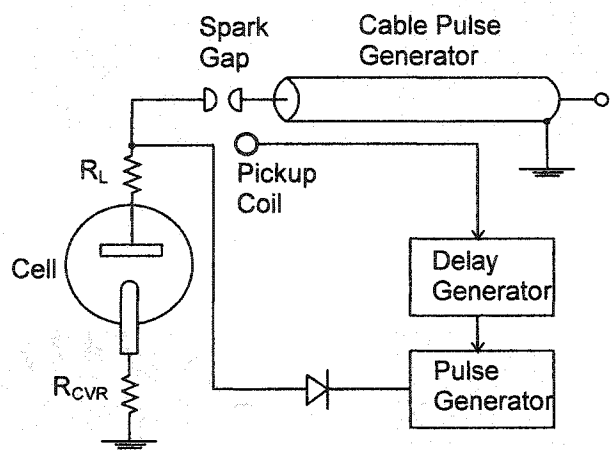

FIG. 5.1. Pulse-probe system (double pulse generator). The first pulse is generated by a cable pulse generator (50 Ω, 4 m), which produces a 40 ns pulse at up to 30 kV with a matched load of 50 Ω. The second pulse is generated by a trigger generator (Maxwell 40330). The interval between the two pulses is controlled by means of a delay generator that is triggered by the electromagnetic signal of the spark gap.

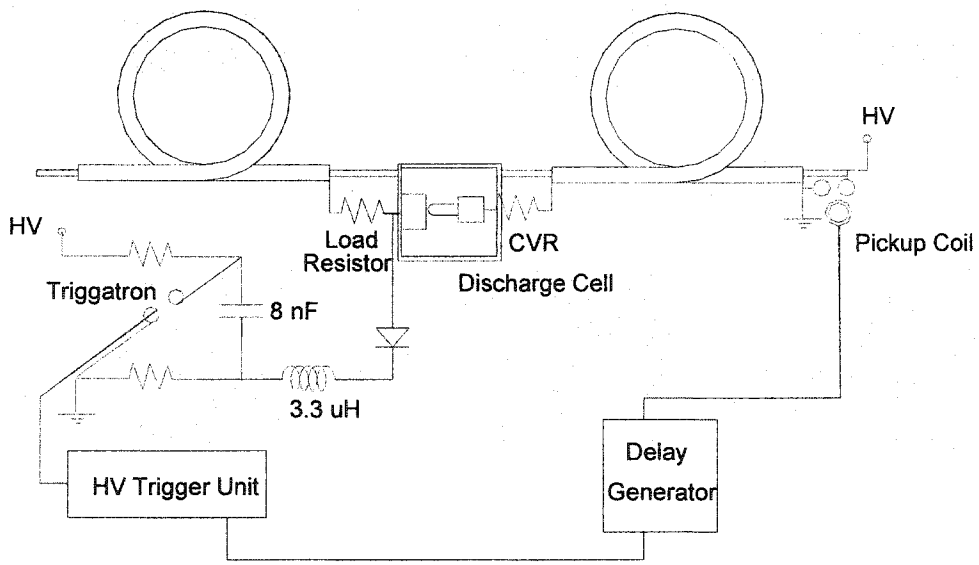

FIG. 5.2. Blumlein line pulse-probe system. The first pulse is generated by a Blumlein line generator which produces a 120 ns pulse. The second pulse is generated by a ramp pulse generator. The interval between the two pulses is controlled by means of a delay generator that is triggered by the electromagnetic signal of the spark gap.

Reproduced with permission of the copyright owner. Further reproduction prohibited without permission.

5.3 OPTICAL DIAGNOSTICS

Shadowgraph and Schlieren methods are used to study the temporal and spatial evolution of breakdown and postbreakdown phenomena by recording the change in the refractive index of the water. We use only shadowgraphy in the optical diagnostic of propylene carbonate. Both shadowgraphy and Schlieren methods are integrated optical systems, projecting optical information along an axis into the screen. Optical inhomogeneity refracts light rays in proportion to the gradients of refractive index in the x, y- plane [71]. The components of the angular ray deflection in the x- and y- directions are,

$$\delta_x = \frac{1}{n}\int \frac{\partial n}{\partial x}\partial z, \quad \delta_y = \frac{1}{n}\int \frac{\partial n}{\partial y}\partial z \tag{5.1}$$

For the area of extent L along the optical axis, Eq. 5.1 becomes,

$$\delta_x = \frac{L}{n_0}\frac{\partial n}{\partial x}, \quad \delta_y = \frac{1}{n_0}\frac{\partial n}{\partial y} \tag{5.2}$$

where n_0 is the refractive index of the surrounding medium. These expressions are the mathematical basis of the shadowgraphy and Schlieren system.

5.3.1 Shadowgraphy

A shadowgraphy diagnostic setup is shown in Fig. 5.3a. Before the test object is inserted into the system, and without the resulting lateral changes of the refractive index, the illumination is evenly projected into the screen. Once a test area is in the optical path, the ray becomes refracted because of the lateral refractive index gradient. Usually, the gradient is the greatest along the edge of the test object; thus, light refraction is strongest at the boundary area between

Reproduced with permission of the copyright owner. Further reproduction prohibited without permission.

the surroundings and test object. The angular ray deflection is δ, as shown in the Fig. 5.3a. No refraction occurs outside the test object or exactly at its center. At the screen, an overlap of the deflection angles appears which corresponds to the gradient of the deflection angles. Mathematically, we can express $\delta_x = \frac{L}{n_0}\frac{\partial^2 n}{\partial x^2}$, demonstrating that the shadowgraphy responds to the second spatial derivative of the refractive index.

5.3.2 Schlieren Method

A Schlieren system requires a focused lens and a sharp knife-edge or some other cutoff to block the refracted light partially, whereas no such cutoff is needed in shadowgraphy. The illuminance level in a Schlieren image responds to the first spatial derivative of the refractive index of the test area, e.g. $\partial n/\partial x$. As seen in Fig. 5.3b, an object S in the test area blends light rays away from their original paths. A second lens focuses the ray from each point in S to a corresponding point on the screen. There are two such rays, one of which bends upward, the other downward, from a specific point on S. Both rays are deflected away from the optical focus axis. The upward ray illuminates a point on the screen, but the downward ray hits the knife-edge and is blocked. It subsequently appears dark against the bright background. For this particular point of the object, the phase difference causing the vertical gradient $\partial n/\partial x$ in the test area is converted to a light amplitude difference. A finite Schlieren object refracts a multitude of rays in many directions. All downward components of these rays are

Reproduced with permission of the copyright owner. Further reproduction prohibited without permission.

blocked by the cutoff and so only the upward rays shadow a partial picture of the test object on the bright background screen.

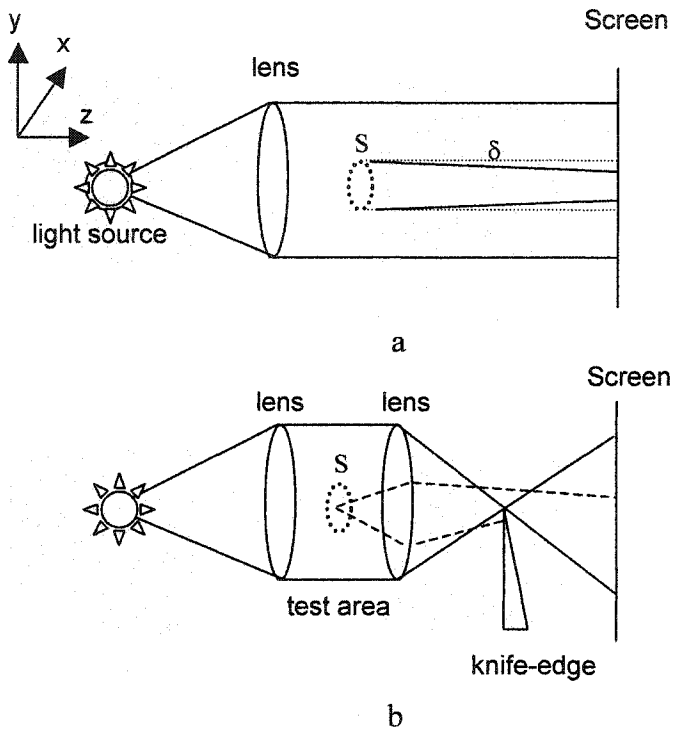

FIG. 5.3. a) Diagram of a shadowgraph. b) Schlieren system with a point light source.

5.3.3 Optical Setup

The experimental optical setup can be seen in Fig. 4.2 and Fig. 4.6. A 10 mW He-Ne laser is used as the light source. The expanded laser beam with a diameter of 3 mm covers the space between the two electrodes. A CCD camera [4Picos, Stanford Computer Research] is used to record the Schlieren images with a temporal resolution of 2 ns through a bandpass filter (632 nm) which

Reproduced with permission of the copyright owner. Further reproduction prohibited without permission.

allows only the laser light to pass. A razor blade is used as Schlieren cutoff. The camera is triggered by the pickup signal from the same spark gap that serves as a closing switch for the Blumlein line pulse generator. The recording time throughout the spark gap breakdown could be controlled by a variable delay time generator, which is set by the CCD controlling software.

For high energy level experiments, the camera is placed in a shielded Faraday cage with a pinhole as an optical access to avoid mistriggering from an increased EM noise. The camera is triggered from the oscilloscope (Tektronix TDS 640A) at various delay times with respect to the recorded current across the shunt resistor.

Reproduced with permission of the copyright owner. Further reproduction prohibited without permission.

CHAPTER VI

EXPERIMENTAL RESULTS

In this chapter, we present the experimental results of electrical breakdown and dielectric recovery of water and propylene carbonate obtained through the electrical and optical setups and diagnostics described in Chapters 4-5. The investigation attempts to delineate various phenomena following the breakdown and during the process of the dielectric recovery.

6.1 VOLTAGE-CURRENT CHARACTERISTICS OF BREAKDOWN IN WATER

With the 50 Ω Blumlein line pulsed power system, a high voltage pulse 200 ns in duration is generated which causes water breakdown. Here, the rod electrode is anode. Typical electrical voltage and current waveforms are shown in Fig. 6.1. At an applied voltage of approximately 15 kV (charging voltage V=7.5 kV), which corresponds to an average electric field of 750 kV/cm in the gap, the gap breaks down approximately 100 ns after the voltage is applied. After breakdown, the voltage across the gap decreases to values very small compared to the applied voltage. Voltage oscillations of small magnitude can be observed, caused by the stray capacitance and inductance in the circuit. The largest capacitance effect contributing to the oscillation exists between the plane electrode and the flange at which the hemispherical electrode is installed. Since this capacitance is discharged quickly after breakdown, it strongly contributes to the initial phase of the discharge.

Reproduced with permission of the copyright owner. Further reproduction prohibited without permission.

During breakdown, the current increases to a value of I = 150 A, as determined by the load impedance (V=7.5 kV, R_L=50 Ω). It stays constant for a duration of 100 ns, again determined by the now matched electrical circuit. After a period of 300 ns, a second current pulse is observed. This pulse is caused by reflection at the open end of the Blumlein PFL. The energy deposited into the water gap can be calculated as 20 mJ by integrating the measured voltage and current (Fig. 6.1). This is approximately 9% of the total energy stored in the PFL (225 mJ). The remaining 205 mJ is dissipated in the load resistor.

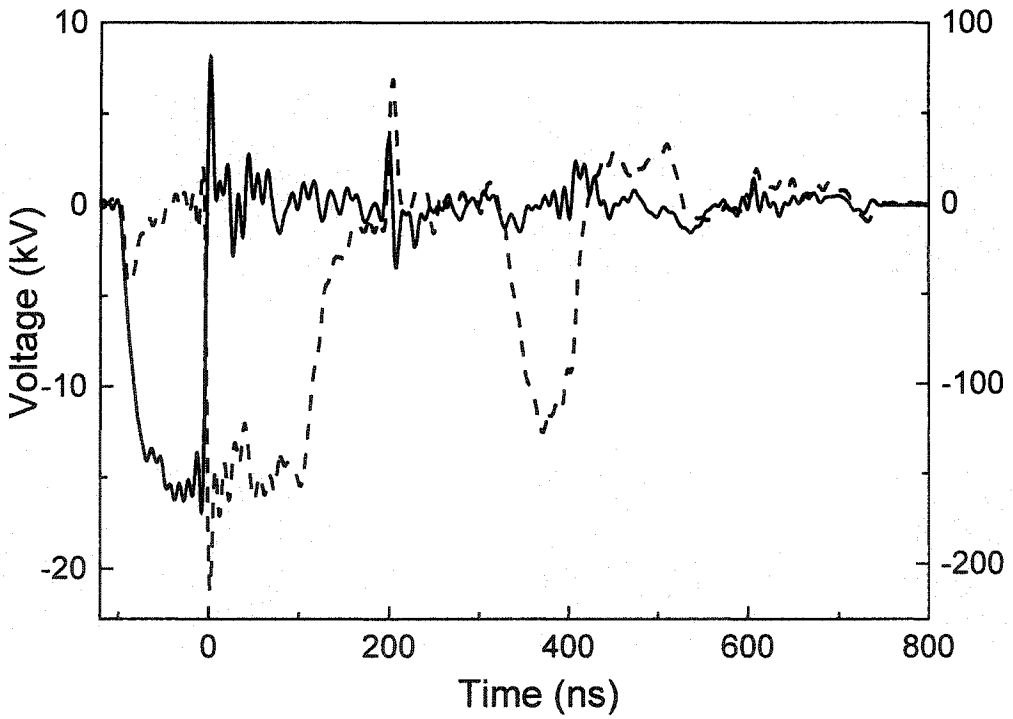

FIG. 6.1. Voltage (solid line) across the water gap and current (dashed line) through the gap. The high frequency components in both signals are removed by a 100 MHz low pass FFT filter.

Reproduced with permission of the copyright owner. Further reproduction prohibited without permission.

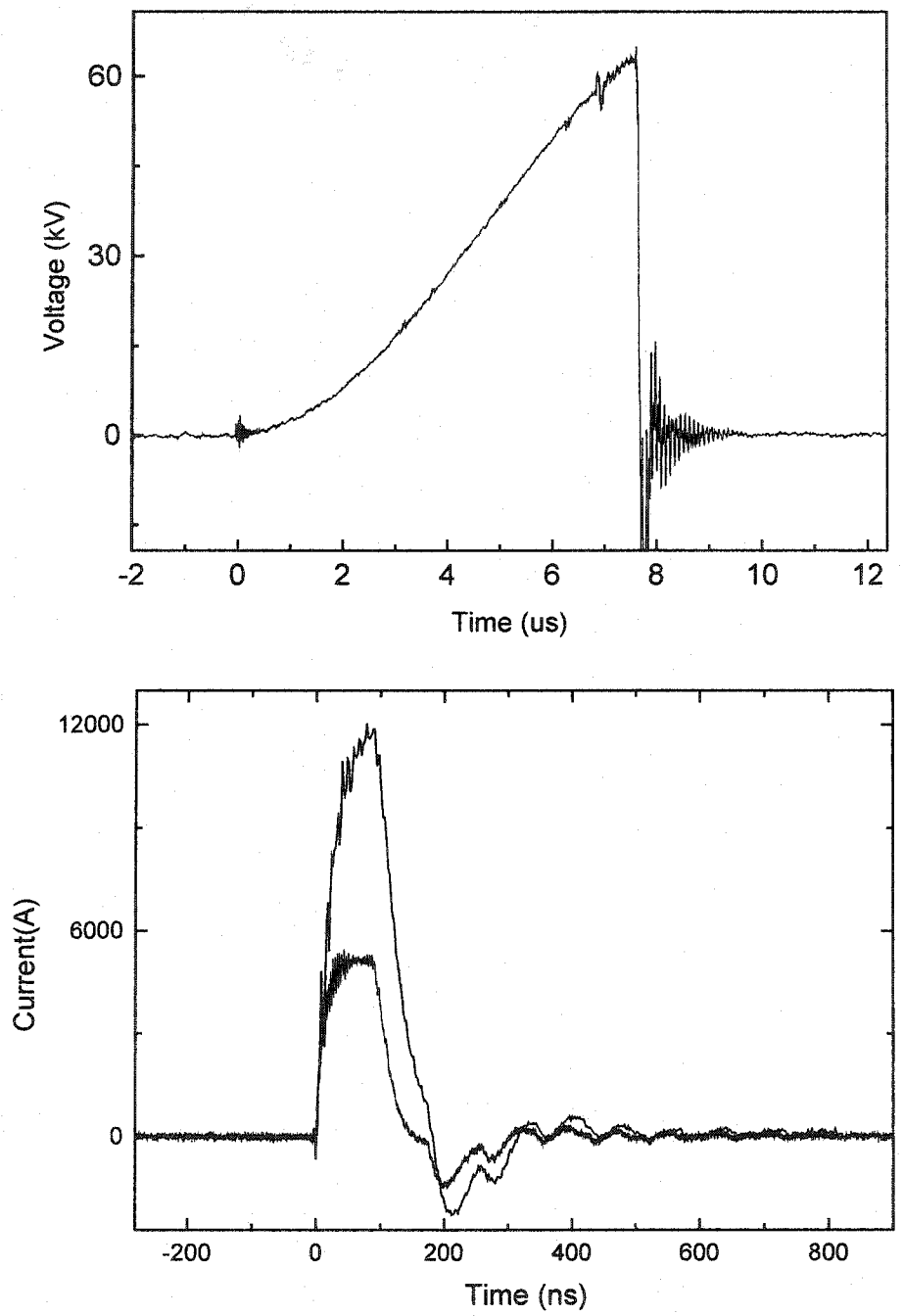

FIG. 6.2. Top: The charging pulse is applied to the water gap until self-breakdown causes the voltage collapse. Bottom: The current pulses for 28 kV (0.5 mm gap) and 63 kV (1 mm gap) breakdown.

Reproduced with permission of the copyright owner. Further reproduction prohibited without permission.

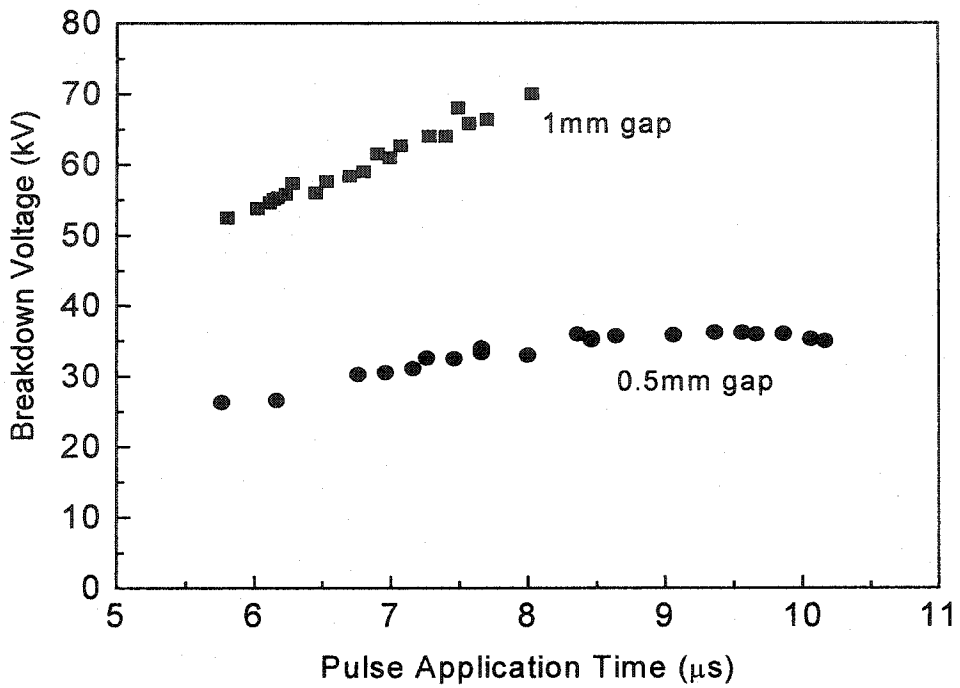

FIG. 6.3. Breakdown voltage as a function of pulse application time for 1 mm gap and 0.5 mm gap.

Reproduced with permission of the copyright owner. Further reproduction prohibited without permission.

For a 2.5 Ω, all-water system with a higher stored energy, it takes 8 μs to charge the PFL (Fig. 6.2). In the experiment, the anode is a nozzle electrode and the pin is at ground potential. For a 1 mm gap distance, with a breakdown voltage 63 kV, the resulting peak current is 12 kA, approximately equivalent to 0.5V/Z, where Z is 2.5 Ω. It is observed that this current pulse has a duration time longer than the other current pulse (100 ns, 5.2 kA), which is generated by 28 kV at gap distance of 0.5 mm. This is because the longer gap causes an increase in the inductance. A slight mismatch (<15% reflection) is observed in both current pulses (Fig. 6.2) and could be due to the nonlinearity of the carbon film resistors.

The breakdown voltages for both the 0.5 mm and 1 mm gaps are shown in Fig. 6.3. These are based on results from 20 shots. The average breakdown voltage is 33 ± 2.0 kV for 0.5 mm gap and 63 ± 3.0 kV for 1 mm gap. The average energy stored in the PFL is 15 J and 50 J respectively.

6.2 POSTBREAKDOWN PHENOMENA IN WATER

Schlieren photographs taken during the postbreakdown phase of a 200 μm water gap at various times after breakdown are shown in Fig. 6.4. The plasma generated during breakdown is visible for more than 1 μs. The photograph taken at 200 ns also shows, besides the plasma, a shock wave extending from the inter-electrode area. After 500 ns, a system of shock waves is visible, with the plasma fading away. At 1.3 μs, an opaque volume between the electrodes begins to emerge between the electrodes. By 200 μs, it has grown to millimeters in size. It begins to decay around 500 μs and disappears after 1 ms.

Reproduced with permission of the copyright owner. Further reproduction prohibited without permission.

Higher energies of 15 J and 50 J also show the decay of plasma, emission of spherical shock waves, and opaque volume development (Fig. 6.5). Fig. 6.6 shows the gap 2 ms after breakdown for these conditions. Opaque pockets still adhere to the electrodes. In both cases, the gaps become free of opaque pockets after 10 ms. Compared to a low energies, the time for the gap to becomes free of opaque volume is only about ten times longer even though the energy levels have been increased by a factor of fifty.

Reproduced with permission of the copyright owner. Further reproduction prohibited without permission.

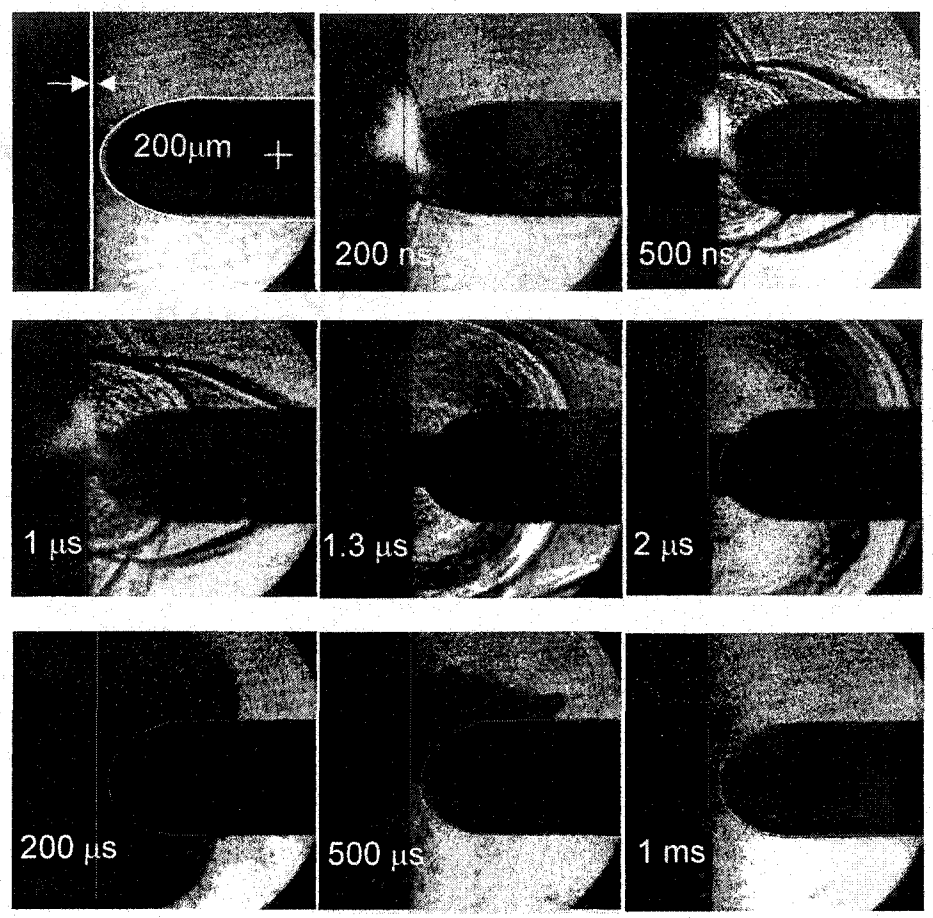

FIG. 6.4. Temporal development of plasma, shock wave and opaque volume after breakdown of a 200 μm water gap. Top left is a reference (no pulse).

Reproduced with permission of the copyright owner. Further reproduction prohibited without permission.

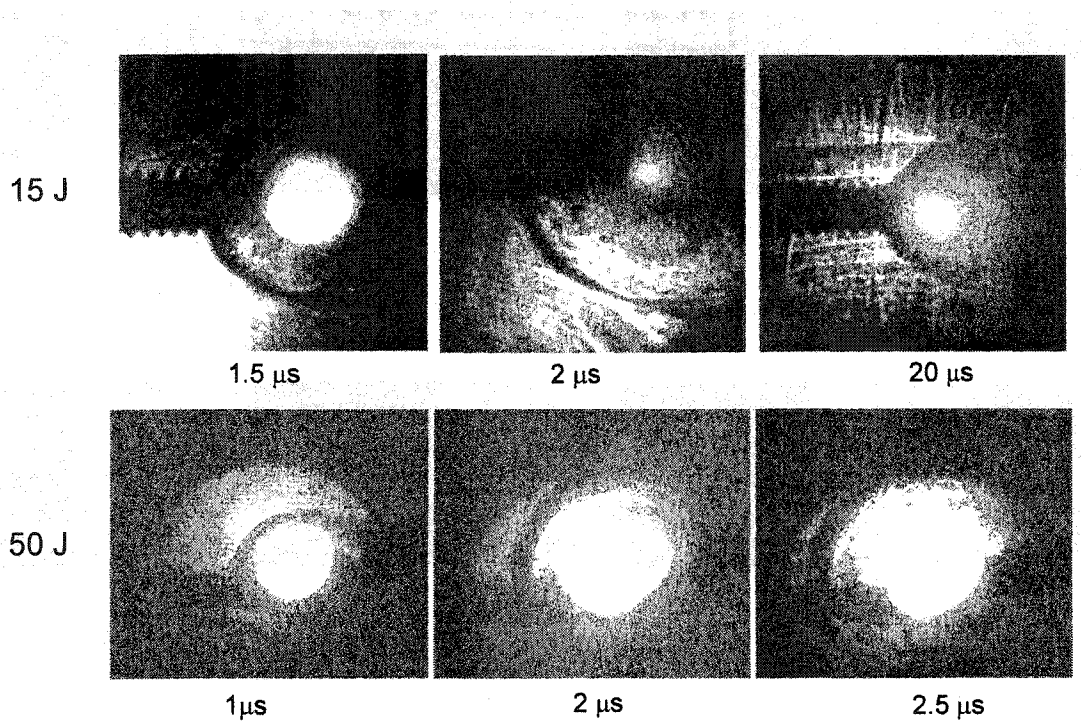

FIG. 6.5. Postbreakdown events a few microseconds after breakdown for energies of 15 J and 50 J.

Reproduced with permission of the copyright owner. Further reproduction prohibited without permission.

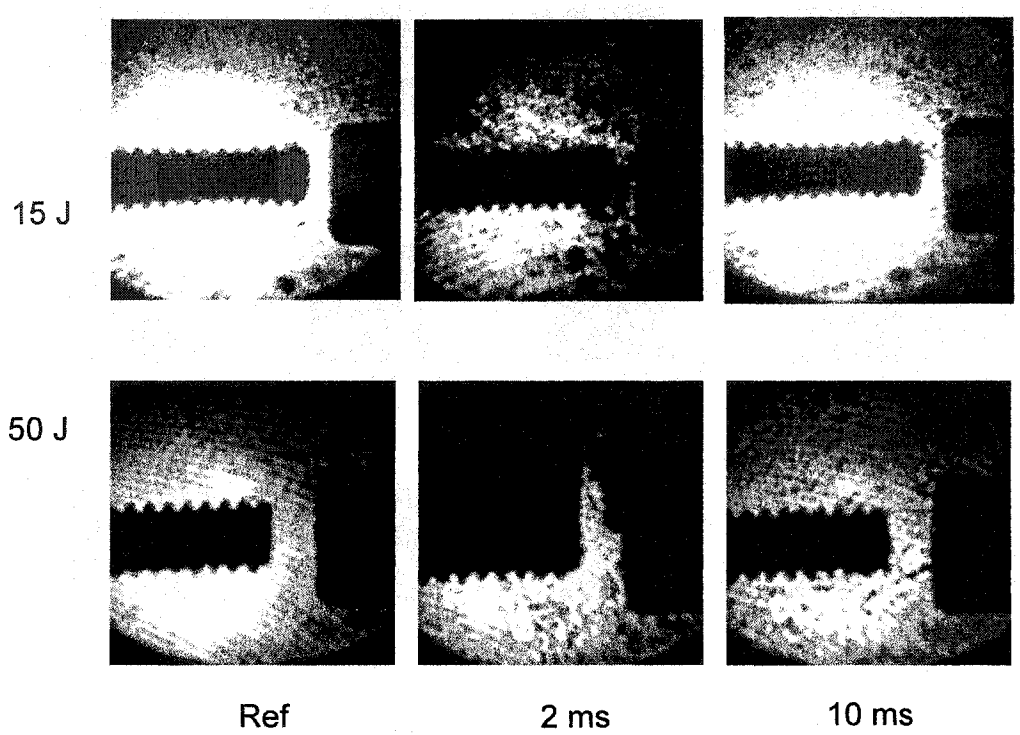

FIG. 6.6. Postbreakdown events several milliseconds after the breakdown for 15 J and 50 J.

Reproduced with permission of the copyright owner. Further reproduction prohibited without permission.

6.3 VOLTAGE RECOVERY OF WATER AFTER BREAKDOWN

The presence of the opaque volume generated during breakdown and the conduction of the gap determine the recovery of water for approximately 1 ms after breakdown. Higher energy lengthens the recovery time to 10 ms at 50 J. We shall see that application of high voltage probe pulses during this recovery time results in breakdown at significantly lower voltages. The value of the breakdown voltage and the position of plasma formation depend on the time after the first breakdown. To demonstrate this, we use the pulse-probe system (Fig. 5.1) to diagnose the dielectric strength. The first voltage pulse generates the breakdown, and by applying a second pulse the electrical voltage recovery is measured. The first pulse deposits energy stored in the PFL 32 ± 10 mJ to the gap. The charging time is 100 ± 20 ns. We took shadowgraphs in the probing phase with different delays after the first breakdown. At 250 μs after breakdown, the probe pulse causes a breakdown at the center of the gap, with an amplitude of 3 kV, corresponding to 20% of the full dielectric strength (Fig. 6.7). At 500 μs, the gap breaks down near the edge of the electrodes at an increased breakdown voltage of 9 kV (60% of full dielectric strength). This indicates that the recovery of the gap begins at the center and propagates with time to the edges. After 700 μs, the breakdown occurs again in the center of the gap at 12 kV (80% of full dielectric strength). In addition, plasma formation is also observed in the outer areas, where opaque pockets obviously still exist. At 1 ms, the water gap is fully recovered, and the breakdown occurs only in the center, where the electric field is most intense. The breakdown voltage is now 14.5 kV. The changes in

Reproduced with permission of the copyright owner. Further reproduction prohibited without permission.

breakdown position indicate the location and the state of recovery at various times after the first breakdown.

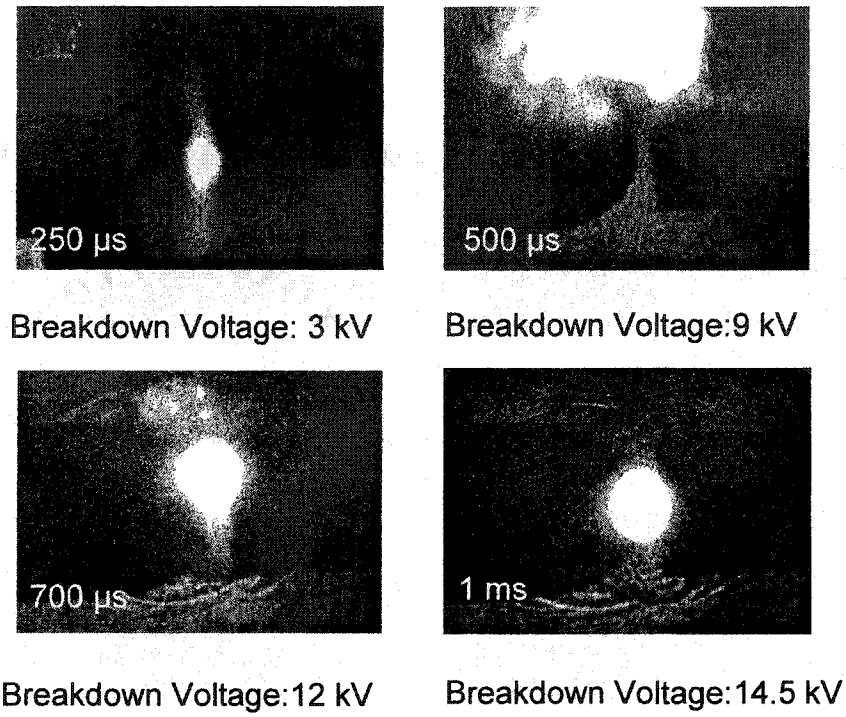

FIG. 6.7. Breakdown and plasma formations due to a second probing pulse at various delays after the first breakdown.

Reproduced with permission of the copyright owner. Further reproduction prohibited without permission.

6.4 EFFECTS OF FLOW ON THE RECOVERY OF WATER

From the Schlieren (Fig. 6.4) and shadowgraph images (Fig. 6.7) taken after breakdown, it is obviously that the opaque volumes determines the dielectric recovery and dielectrics strength of the liquid. To shorten the recovery time of the liquid before the time it takes naturally to decay, we need to remove the opaque volumes.

6.4.1 Recovery of Water with Transverse Flow

The effect of differing transverse flow rates on the recovery of the water gap is studied with the pin-rod electrode system. Shadowgraphs are taken at various times after breakdown for static water and for flow rates of 0.56 L/min and 3.5 L/min, respectively. For static water the recovery time is approximately 1 ms, as shown in Fig. 6.8. A flow rate of 0.56 L/min results in laminar flow (also shown in Fig. 6.8) and reduces the recovery time from 1 ms to 700 μs. As shown in Fig. 6.8, at 500 μs, the opaque volume has already been swept away from the center, however the gap recovery is not complete. For the flow rate of 3.5 L/min, which causes turbulence (Fig. 6.9), the opaque pocket has been pushed to the lower part of the electrode system, where it remains. The breakdown event always occurs in the volume where the turbulence is confined for three different times after the first breakdown event. At 250 μs, the breakdown voltage is approximately 3 kV (18%). At 500 μs and 1 ms, the breakdown voltage is 6 kV (37%). Turbulent flow does not help the recovery of water and applying a second

Reproduced with permission of the copyright owner. Further reproduction prohibited without permission.

pulse causes a large volume discharge at a low voltage at various times after the first breakdown.

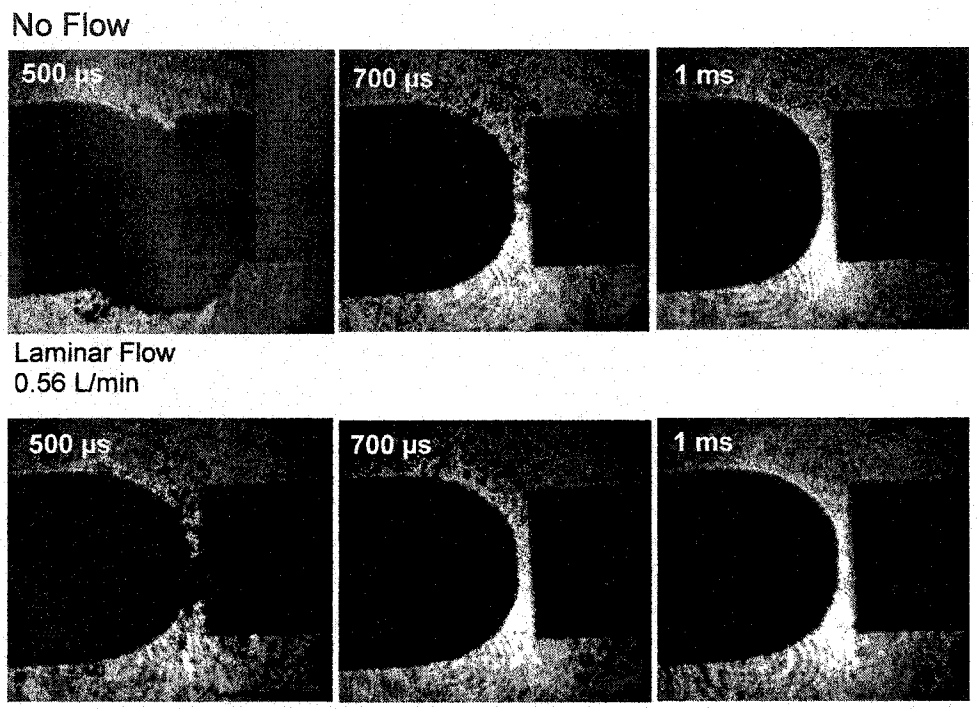

FIG. 6.8. Transverse flow in a laminar pattern effectively shortens the recovery time to 700 µs.

Reproduced with permission of the copyright owner. Further reproduction prohibited without permission.

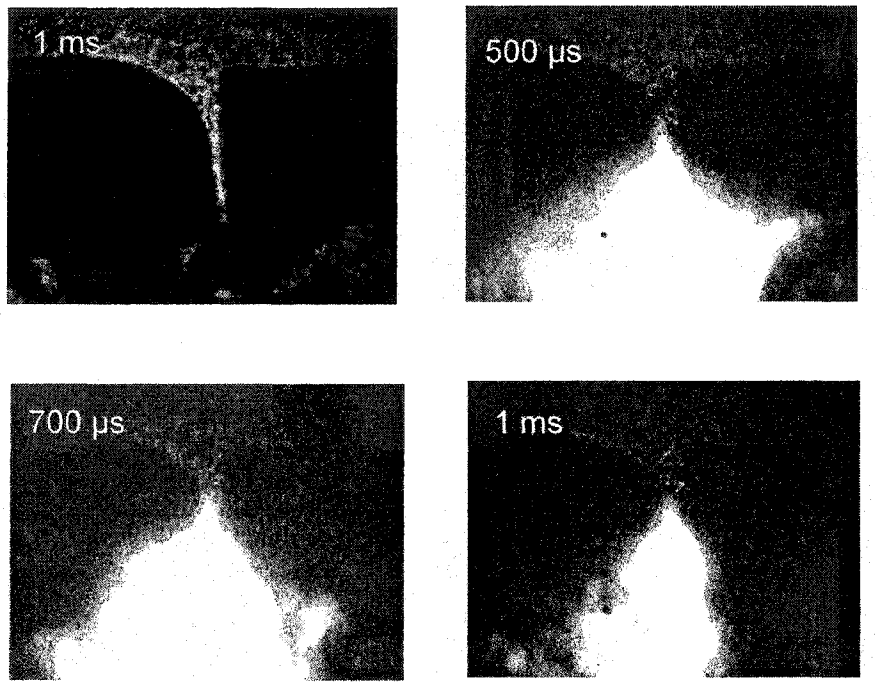

FIG. 6.9. Turbulent flow does not help the recovery. Applying a second pulse causes large volume discharge at a low voltage at various times after the first breakdown.

Reproduced with permission of the copyright owner. Further reproduction prohibited without permission.

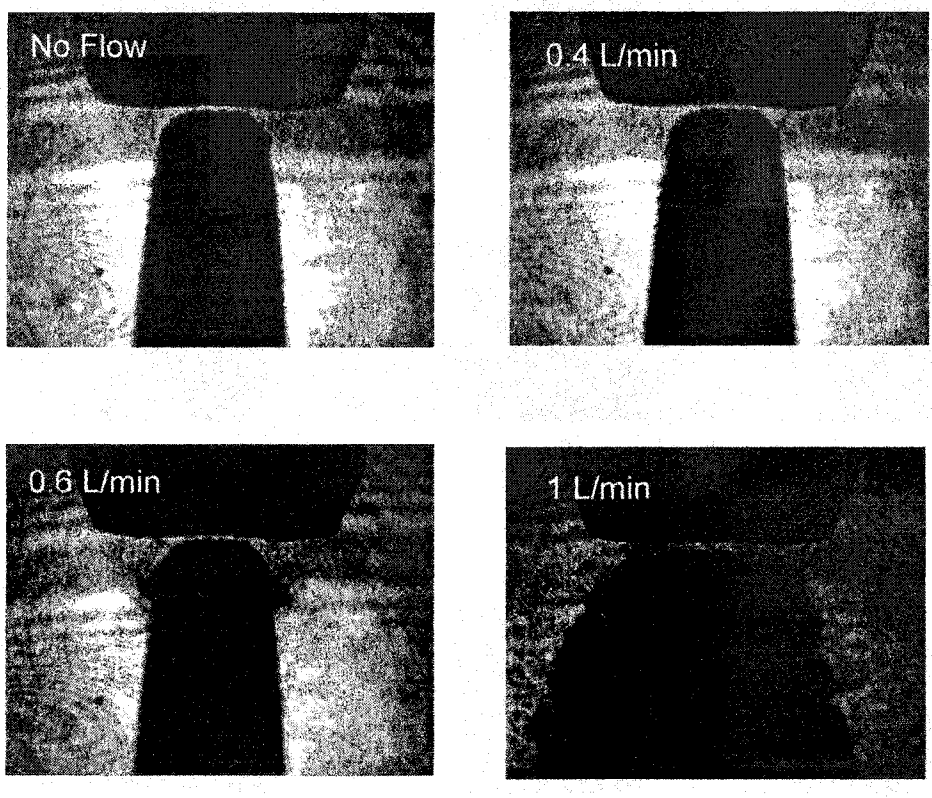

FIG. 6.10. Axial flow patterns at different flow rates. A flow rate of 0.4 L/min creates a laminar flow. Increasing flow rate to 0.6 L/min causes slight turbulence. Extreme turbulence is seen at flow rate of 1.0 L/min

Reproduced with permission of the copyright owner. Further reproduction prohibited without permission.

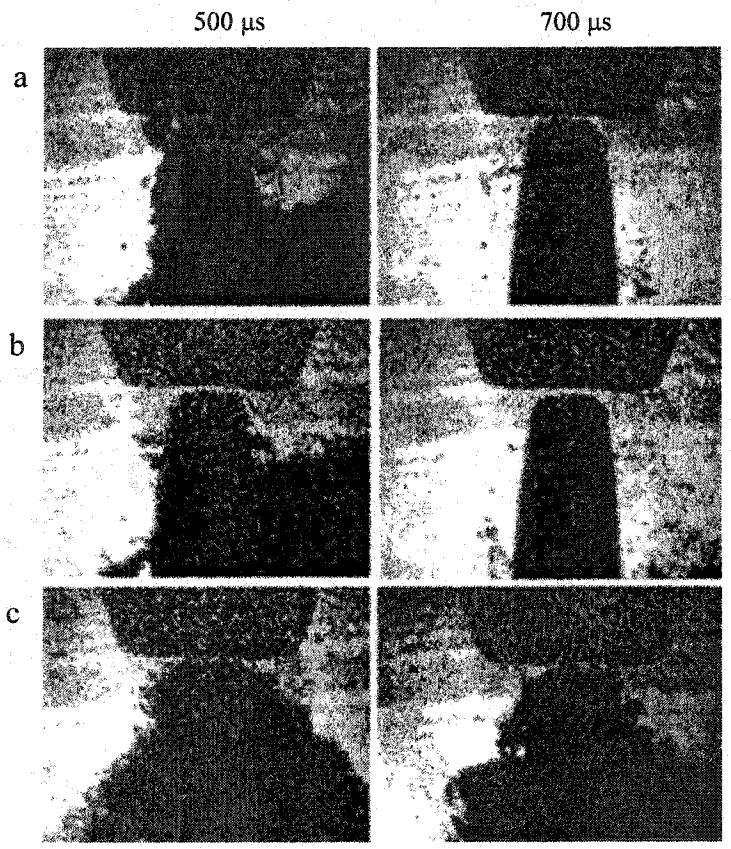

FIG. 6.11. Flow pattern after the first breakdown in a) static water b) laminar flow (0.4 L/min) and c) turbulent flow (0.6 L/min).

Reproduced with permission of the copyright owner. Further reproduction prohibited without permission.

6.4.2 Recovery of Water with Axial Flow

The effect of axial flow on the recovery of the water gap is also studied using the nozzle-pin electrode system (Fig. 4.3). Highly pressurized water flows through the nozzle and around the pin electrode. Up to a flow rate of 0.4 L/min, the flow in this geometry is found to be laminar. A higher flow of 0.6 L/min creates some turbulence. Further increasing the flow to a value larger than 1 L/min causes extreme turbulence in the gap.

Fig. 6.11 shows the effect of the axial flow on the removal of the opaque pockets during the postbreakdown phase. At 500 μs, a flow with a rate of 0.4 L/min removes the opaque pockets efficiently than 0.6 L/min. At 700 μs, the gap between the electrodes for 0.4 L/min is free of opaque pockets. Again, as in the case of transverse flow, efficient removal can only be achieved if the flow is laminar. Turbulent flow generally causes opaque pockets to persist in the gap longer even than with no-flow conditions.

6.5 ELECTRICAL RECOVERY RATE OF WATER

6.5.1 Recovery Rate of Static Water

The development and decay of the opaque volume determines the dielectric recovery of the water gap. This can also be shown from the results of the pulse-probe measurements. The first pulse, generated by the cable pulse generator shown in Fig. 5.1, causes water breakdown in the 200 μm gap at 15 kV, 100 ns after voltage application. The jitter in this breakdown time lag is 40 ns.

Reproduced with permission of the copyright owner. Further reproduction prohibited without permission.

The power deposited into the water prior to breakdown is calculated from the voltage-current waveform as 12 mJ ± 2 mJ.

The recovery versus pulse rate (inverse of time between first and second pulse) is shown in Fig. 6.12. Each data point is based on measurements obtained from 30 discharges. The breakdown voltage for single shot operation with a 4 s interval (pulse rate of 0.25 Hz, triangle in this figure) is measured as 14 kV ± 1 kV, corresponding to a normalized value of 1 ± 0.05 with respect to the voltage of 14 kV. The breakdown voltages are almost identical to the lowest values obtained with pulse-probe experiments (at 10 Hz). The water gap recovers almost fully at pulse rates up to 1 kHz. For higher pulse rates, the maximum voltage which can be applied for the second pulse decreases drastically. At 2 kHz it has decreased almost 50% with large fluctuations in value (30%-90%). At 4 kHz only 10% of the initial voltage can be applied.

6.5.2 Recovery Rate of Water with Flow

Optical studies (Fig. 6.11) show that an axial flow of 0.4 L/min for the nozzle-pin electrode allows us to remove the opaque pockets most efficiently with the least amount of water compared to transverse flow (Fig. 6.8). This is also the optimum condition for high recovery rates as shown in Fig. 6.13. The energy transferred to water by the first pulse (19 kV) is 65 ± 10 mJ. The charging time is 70 ± 14 ns. Each error bar represents the data of 30 shots, normalized to the breakdown voltage of fully recovered water (16.2 kV). The recovery rate for static

Reproduced with permission of the copyright owner. Further reproduction prohibited without permission.

water is approximately 1 kHz with an average recovery of 95%. At recovery rates larger than 1 kHz, the average recovery is less than 80%.

With a flow of 0.4 L/min (laminar flow), the recovery rate is increased over the value obtained with static water to 1.4 kHz (95%). At 2 kHz, the average recovery is 80%. At 2.5 kHz, the average recovery can still reach 60%. For 0.6 L/min (turbulent flow), the recovery is on the same order, or even less than, static water. At 1 kHz, the recovery is less than that of static water.

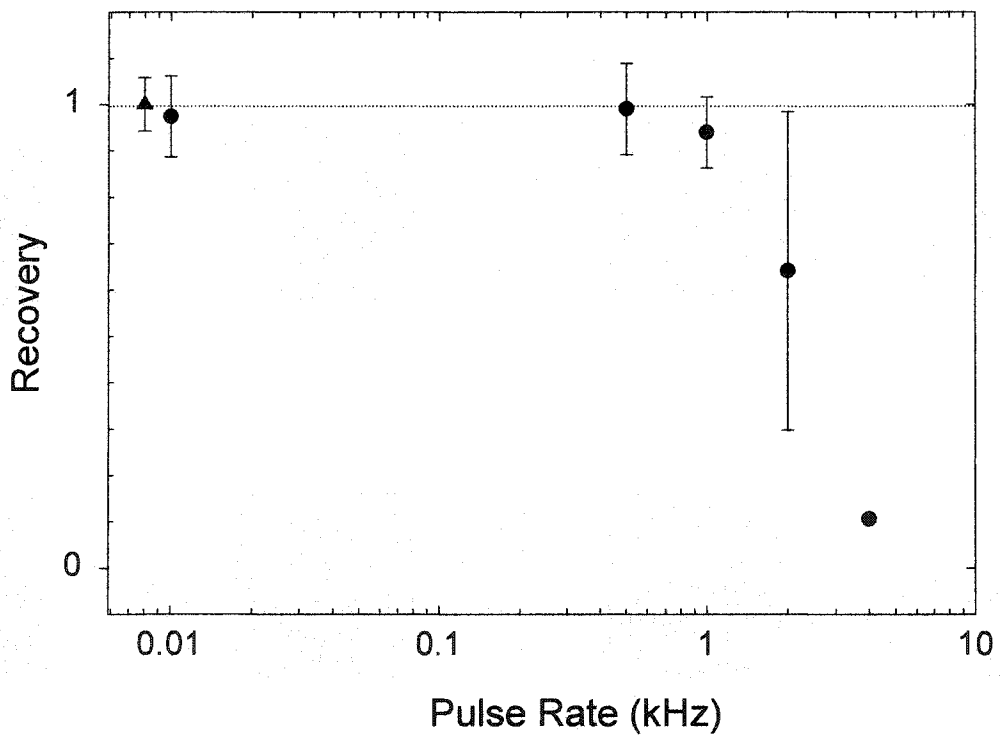

FIG. 6.12. Dielectric recovery as defined by the ratio of the breakdown voltage of the second pulse to that of the first pulse (14 kV in the experiment). The pulse rate is the inverse of the interval between the two pulses. The error bars are based on measurements of 30 pulses. Triangle symbol represents the results of 0.25 Hz.

Reproduced with permission of the copyright owner. Further reproduction prohibited without permission.

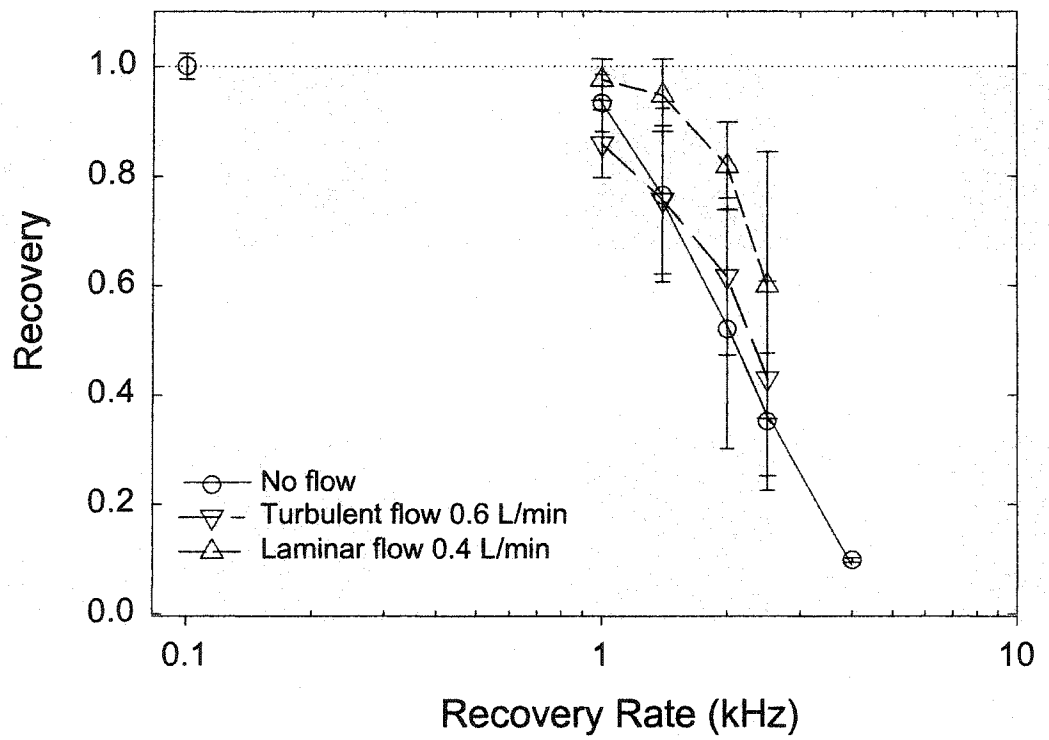

FIG. 6.13. Dielectric recovery for varying flow rates from laminar to turbulent flow.

Reproduced with permission of the copyright owner. Further reproduction prohibited without permission.

6.6 POSTBREAKDOWN PHENOMENA IN PROPYLENE CARBONATE

The postbreakdown phenomena and recovery process of propylene carbonate are studied with the Blumlein line pulse generator (50 Ω, 120 ns). For a 250 μm gap, it requires a voltage as high as 19 kV to cause the gap to break down, which corresponds an average electric field of 760 kV/cm. The energy deposited in the gap is calculated as 30 ± 8 mJ. Laser shadowgraphy records the breakdown and postbreakdown phenomena with variable delays. Some typical events are shown in Fig. 6.14.

Light emission from the plasma volume is seen until 800 ns after breakdown. The plasma volume also emits shock waves in intricate patterns that are similar to the patterns shown for water breakdown. These shock waves can be observed in several microseconds. However, the propagation direction changes to toward the plane electrode (8 μs).

When the light emission decays, opaque volumes similar to those described in water are seen growing in size until they reach a maximum radius at 200 μs. They then begin to shrink until 400 μs when the shape of the opaque cloud becomes asymmetric. This "opaque clog" phenomenon lasts several tens of millisecond. An image taken 10 ms after the breakdown shows clogs near 1 mm in diameter appearing near the gap.

After several tens of shots, the colorless propylene carbonate in the chamber is still transparent, but has changed color in pale yellow, indicating byproducts have been generated. The pale yellow coloration appears to be similar to the one described in literature for polypropylene carbonate dissolved in

Reproduced with permission of the copyright owner. Further reproduction prohibited without permission.

propylene carbonate [72]. To separate this yellow component, we mix the treated propylene carbonate with distilled water. Since propylene carbonate is soluble in water with the proportion of 16:85, we use water in excess. A viscous pale yellow liquid turns out not to be resolvable in water and can be separated. The extracted liquid is dried by keeping it overnight in an oven at 60 $^{\circ}$C to obtain the solid product shown in Fig. 6.15. For ~18 cm^3 treated propylene carbonate after 30 discharges, 0.1-0.5 grams of the byproducts can be extracted. For each discharge, the energy deposited into the gap is 30 mJ, thus the efficiency to generate this kind of product is then 0.1-0.6 gram/J. Raman spectroscopy (Nicolet 960) is used to identify the structure of the new compound. The Raman spectra for the generated products and propylene carbonate are shown in Fig. 6.16. Two main differences are seen through the comparison of the spectrums of the treated byproducts and propylene carbonate. The signal of propylene carbonate at 1780 cm^{-1} is shifted to 1730 cm^{-1}. In addition, two signals at 712cm^{-1} and 850 cm^{-1} disappear and a new signal at 812 cm^{-1} appears.

The voltage recovery is studied with the pulse-probe system (Fig. 5.2). The recovery versus pulse rate (inverse of time between first and second pulse) is shown in Fig. 6.17. Each data point is again based on 30 discharges. We have measured the breakdown voltage for single shot operation at 4 s interval corresponding to a pulse rate of 0.25 Hz (triangle in this figure). We have replaced the liquid during every shot. The breakdown voltage is measured as 19 kV $\pm$ 1 kV, corresponding to a normalized value of 100 $\pm$ 5% with respect to the breakdown voltage of the preceding shot of 19 kV. For pulse rates between 100

Reproduced with permission of the copyright owner. Further reproduction prohibited without permission.

Hz and 10 Hz, the recovery percentage does not change and the breakdown voltages are almost 80% of the values obtained with pulse-probe experiments at 0.25 Hz. For higher pulse rates, the maximum voltage which can be applied for the second pulse decreases drastically. At 1 kHz, it has decreased to almost 50% with large fluctuations in value (30%-80%). At 2 kHz, only 10% of the initial voltage can be applied.

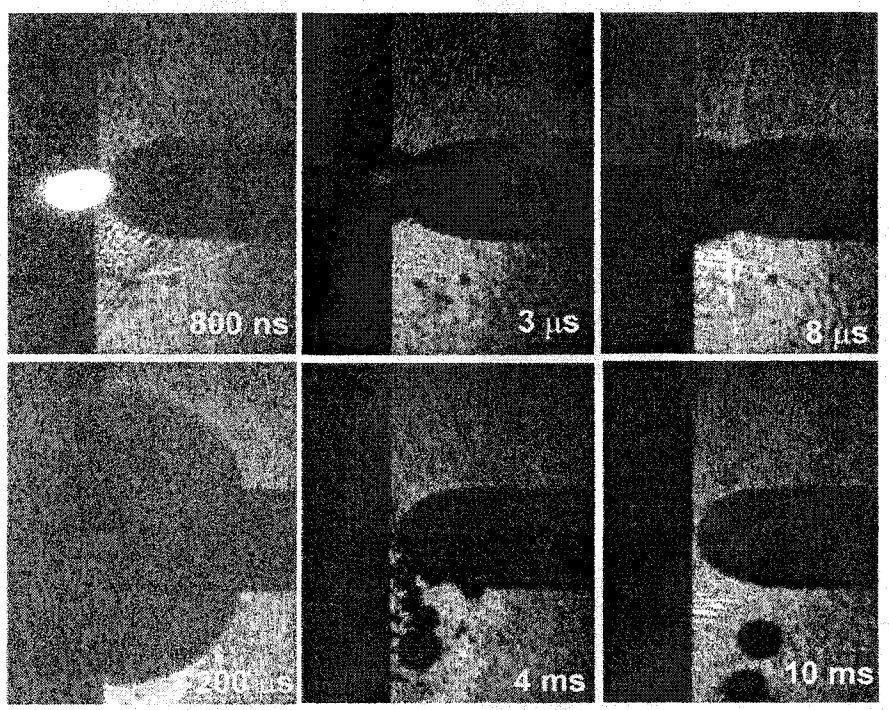

FIG. 6.14. Postbreakdown events after breakdown in a gap with propylene carbonate.

Reproduced with permission of the copyright owner. Further reproduction prohibited without permission.

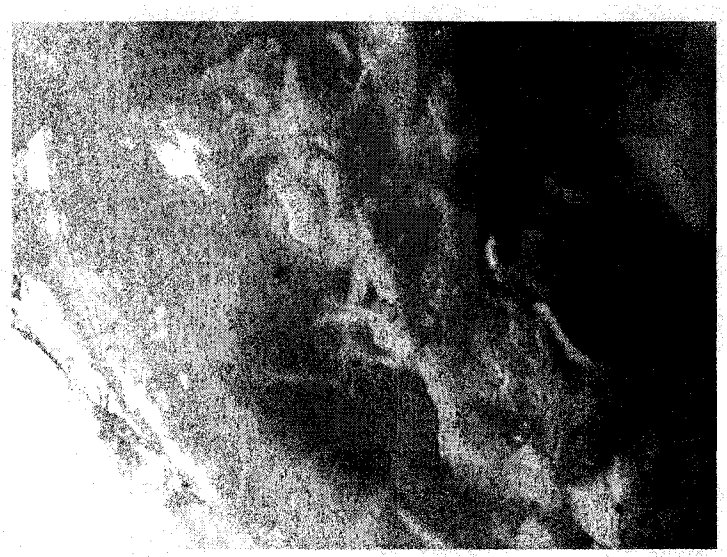

FIG. 6.15. Extracted byproducts after several discharges in propylene carbonate. The sample is dried overnight in the oven at 60 °C.

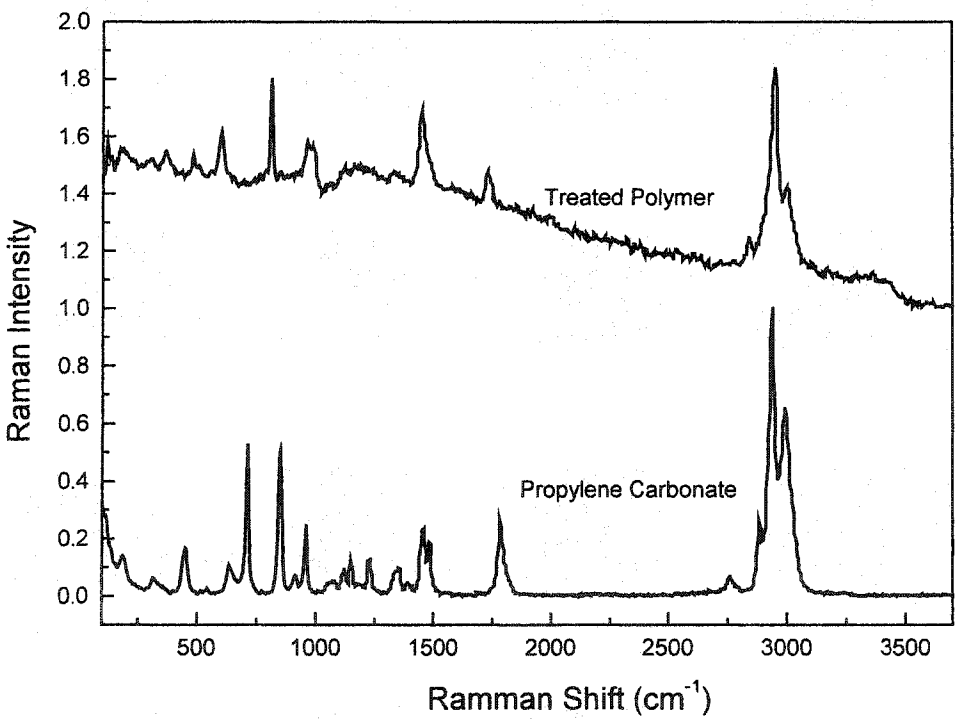

FIG. 6.16. Raman wavelength shift for propylene carbonate before treatment and byproducts separated from the treated propylene carbonate after discharge.

Reproduced with permission of the copyright owner. Further reproduction prohibited without permission.

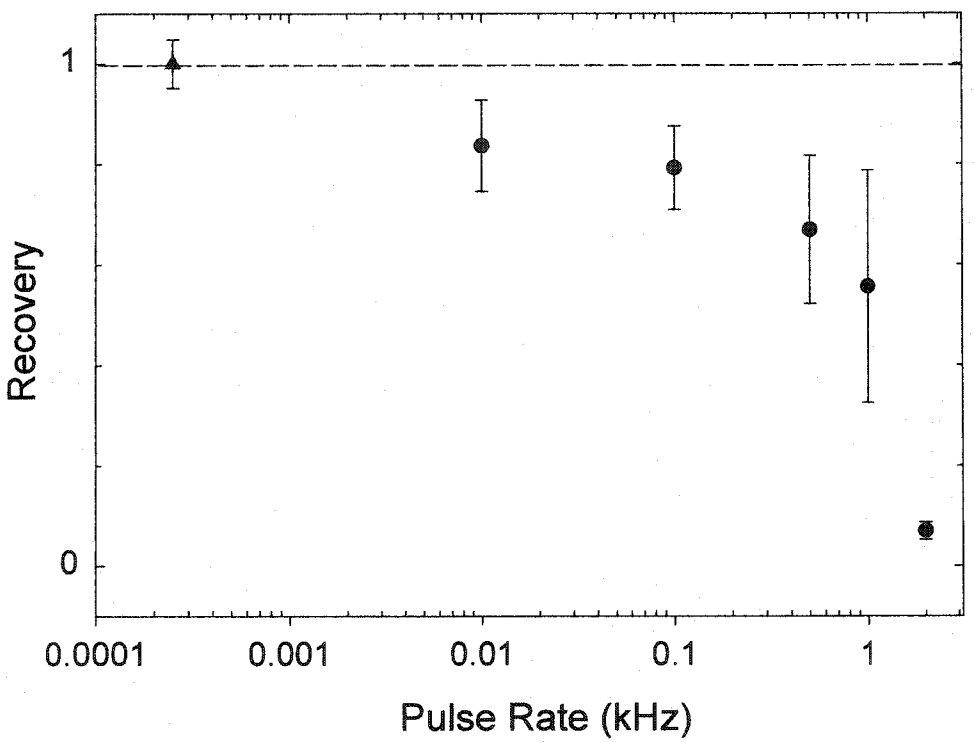

FIG. 6.17. Dielectric recovery obtained by pulse-probe system for propylene carbonate (up triangle data is for pulse rate of 0.25 Hz).

Reproduced with permission of the copyright owner. Further reproduction prohibited without permission.

CHAPTER VII

DISCUSSION

7.1 DIELECTRIC STRENGTH OF WATER

The dielectric strength of water in our experiments with a 200 μm gap consisting of rod and plane electrodes has shown averagely 750 kV/cm. This value is obtained with a pulse duration less than 200 ns pulse in which the rod electrode has positive polarity. Similar levels of breakdown strength, 700-800 kV/cm, have been obtained under the same condition as described in [43]. This value is higher than the 620 kV/cm that Martin's formula predicts. In a longer distance gap (0.5-1 mm), when the discharge is generated with a long pulse of several microseconds and pin electrode is of negative polarity, the calculations based on Eq. (2.2) yield 385 kV/cm and 420 kV/cm for 0.5 mm and 1 mm gaps, respectively, taking into account the field enhancement at the pin electrode. The measured breakdown voltages of 33 kV and 63 kV correspond to electric fields of 670 kV/cm and 720 kV/cm, as calculated by the field simulation software MAGIC [73]. The values are almost twice those predicted by J. C. Martin's scaling law. A comparison of the breakdown strength for two polarities is given in Fig. 7.1. One can see that for a positive polarity, Martin's law seems applicable with stressed time of less than one microsecond. However, for negative polarity with long-term stress, the values of Martin's law differ from our experimental results. The primary differences of our system with Martin's system on which he based his empirical law are the effective stressed area (ours, 0.01 cm^2, Martin's, several

Reproduced with permission of the copyright owner. Further reproduction prohibited without permission.

cm^2) and the gap distance (ours, ≤ 1 mm, Martin's, several millimeters). Since these two parameters determine the power deposition volume, we believe that the breakdown strength may rely on the power density of the pulsing condition. However, it was found that for gap distances between 100 and 400 micrometers, the breakdown field has only a slight dependence on the length of the gap [43]. This result suggests that the breakdown strength more likely depends on the effective area of the electrode.

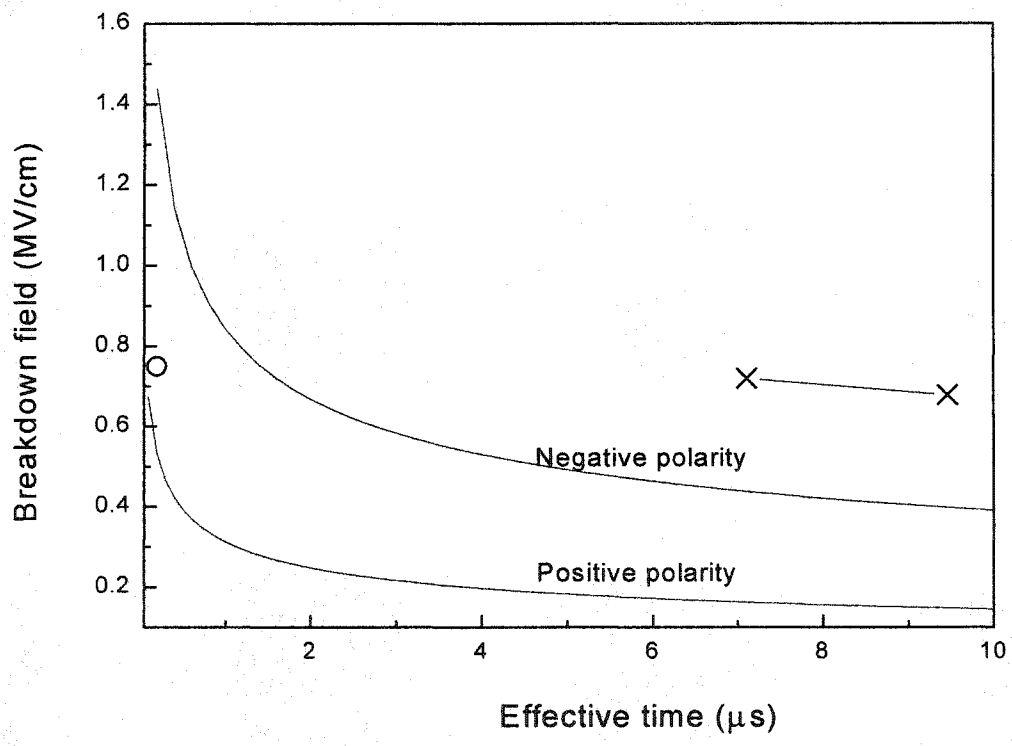

FIG. 7.1. Breakdown field versus pulse application effective time. Solid lines are plotted according to J. C. Martin's formula. Hollow circles represent the data obtained for positive polarity with effective time less than 200 ns. Cross symbols represent the data obtained for negative polarity with a long pulse application time.

Reproduced with permission of the copyright owner. Further reproduction prohibited without permission.

7.2 POSTBREAKDOWN PHENOMENA IN WATER AND IN PROPYLENE CARBONATE

The hydrodynamic process after water breakdown is characterized by three distinct phases with vastly different time scales (Fig. 6.4). The most rapid changes occur during the first phase which is determined by the decay of the plasma between the electrodes. It is on the order of microseconds. The second phase is determined by the propagation of shock waves which are launched during the expansion phase of the plasma column. The time constant for this effect is determined by the propagation velocity of the shock waves and the typical dimensions of the water volume surrounding the gap. The third phase is related to the development and decay of the opaque volume which emerges from the space between the electrodes. The time constant is on the order of millisecond. For higher energy levels, the third phase could be on the order of tens of miliseconds. It is this phenomenon that ultimately determines the recovery of the gap.

7.2.1 Boundary Effect on Shock Wave Emission

After breakdown, characterized by a sudden rise in conductance due to plasma formation between the electrodes, energy is transferred into this plasma in form of Joule heating. This leads to an expansion of the plasma column which, similar to a piston as described in Chapter 3, drives shock waves radially outward. The shock waves appear in the Schlieren photographs as dark lines with bright edges. The observed shock wave structure is rather complex, as shown in Fig.

Reproduced with permission of the copyright owner. Further reproduction prohibited without permission.

6.4. In order to understand the shock wave structure, a description of shock wave propagation in similar geometrical optics (ray approach) has been used [74]. The rays are perpendicular to the wave fronts (Fig. 7.2). The wave emission source S is assumed to be located in the center between the two electrodes. The directed ray trajectory, from S to A, describes the primary directed wave expanding in the water. When the primary directed wave hits the plane electrode, reflection and refraction occur at the interface between the water and stainless steel. Snell's law can be applied to describe the effects at the interface:

$$v_1 \sin\alpha_2 = v_2 \sin\alpha_1 \qquad 7.1$$

where v_1 and v_2 are the sonic velocities in the mediums 1 and 2 respectively, and α_1 and α_2 are the angles of incidence and refraction respectively. In our case, medium 1 is water and medium 2 is stainless steel. The sound velocity in water is 1.48 km/s and in stainless steel it is 5.79 km/s. Consequently, for a shock wave incident from the water, the refracted wave in the electrode is bent towards the plane of incidence (ray SED). This holds for all angles of incidence smaller than the critical angle. The critical angle α_c is calculated as 14.8° by

$$\alpha_c = \arcsin(v_1/v_2) \qquad 7.2$$

For an angle of incidence equal to α_c, an acoustic wave propagates along the plane electrode surface for a certain distance SN, i.e., critical distance, which is determined by the critical angle. It is constantly refracted back into the water with the same angle α_c (such as ray SFN and ray SFGH). These rays result in head waves, which propagate as a surface wave at the acoustic velocity of stainless steel. For an angle of incidence larger than the critical angle, total

Reproduced with permission of the copyright owner. Further reproduction prohibited without permission.

internal reflection occurs. The totally reflected wave, characterized by the ray SBC, has a smaller wave front curvature than the directed wave.

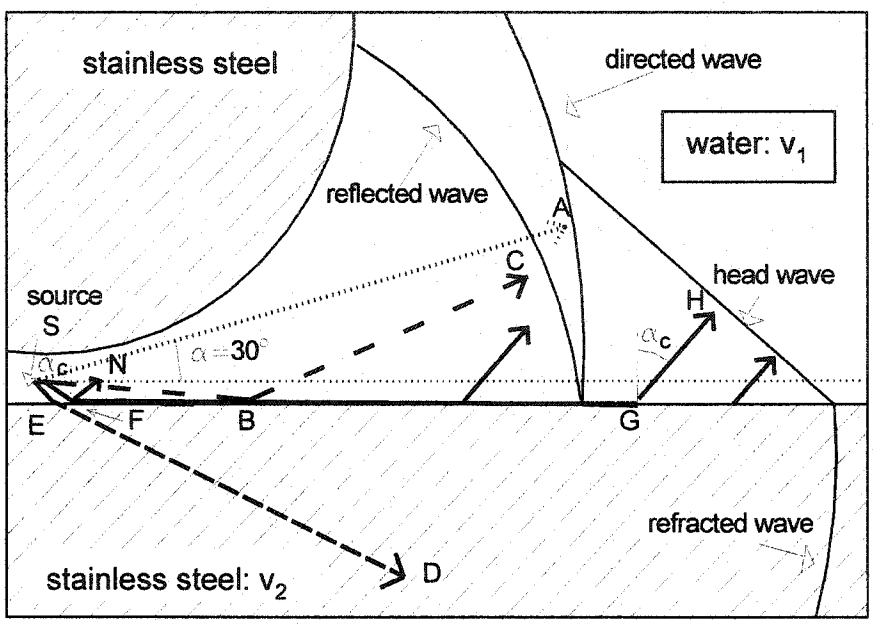

FIG. 7.2. Ray paths between stainless steel electrodes in water ($v_1 < v_2$). The direct ray is SA, the reflected ray is SBC, the refracted ray is SED (invisible in the Schlieren photographs), and the critically refracted ray is SFGH (head wave). The critical distance of headwave is SN with the corresponding ray SFN.

Reproduced with permission of the copyright owner. Further reproduction prohibited without permission.

The directed wave, reflected wave, and head wave can be seen in Schlieren photographs (Fig. 5.4, 200 ns - 2 μs). In addition, from the velocity of the shock wave it is possible to calculate the pressure gradient in the shock wave, which is the difference of the pressure in the undisturbed water in front of the shock wave, p_∞, and the pressure p right behind the shock wave. In order to calculate the shock wave velocity dependent on time after breakdown, the distance SA (Fig. 7.2) is taken from the Schlieren images (Fig. 6.4) for an angle of α=30°, and the values are divided by the time of observation. The differentiation of the various distances SA with respect to time provides the velocity of the shock waves v_s. The time interval for this calculation ranges from 200 ns to 1.3 μs. For longer times the shock wave has passed the observable volume. The angle of 30° is chosen because for this angle the wave can be considered spherical. This shock wave expansion radius is shown in Fig. 7.3 (squares). An extrapolation (dashed line) to time zero gives us the initial size of the shock wave source as approximately 270 μm. From the shock wave velocities v_s, the pressure, p, can be calculated by [75]:

$$p = c_1 \rho_0 v_s [10^{(v_s - v_1)/c_2} - 1] + p_\infty \qquad 7.3$$

where c_1 = 5190 ms^{-1}, c_2 = 25306 ms^{-1} are empirical constants determined from Rankine-Hugoniot data, v_1 = 1483 $ms^{-1}$and ρ_0 = 998 kgm^{-3} are the sonic velocity and density of the undisturbed water, respectively, and p_∞ is the pressure in the unperturbed water.

The calculated pressure versus time is shown in Fig. 7.3. It can be seen that the pressure for the direct wave (SA) decays rapidly from 1000 MPa to 200

Reproduced with permission of the copyright owner. Further reproduction prohibited without permission.

MPa close to the shock wave source (between 270 μm and 2.7 mm). For distances in the centimeter range, the shock waves would be dampened to values which don't pose any hazard to the mechanic stability of the discharge chamber. This holds for all discharge parameters used in our system. The boundary also affects the impedance of the shock wave, as discussed by Murata et al. [76].

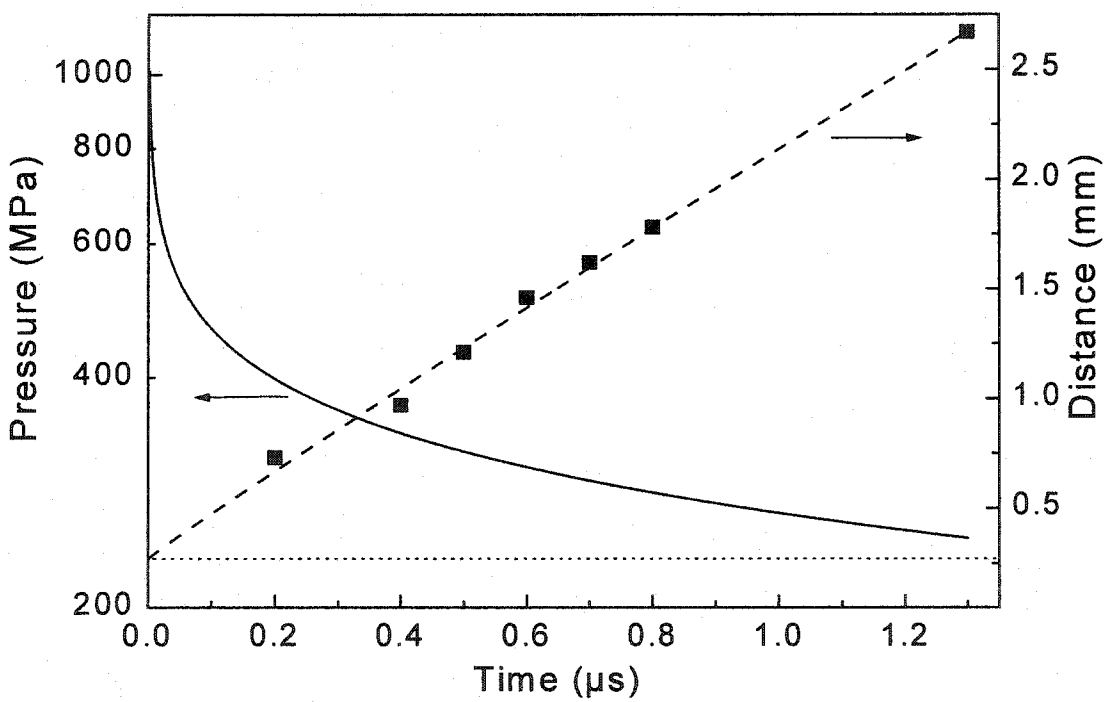

FIG. 7.3. Dependence of measured distance of primary shock wave (square) from source S (Fig. 6.2) versus time after breakdown, and the calculated shock wave pressure. The values extrapolated to time zero indicate source diameter of 270 μm, which corresponds to an initial pressure of 1000 Mpa.

Reproduced with permission of the copyright owner. Further reproduction prohibited without permission.

7.2.2 Energy Dependence of Shock Wave Emission in Water

The breakdown of the water gap at higher switching energies is expected to deposit more energy into the gap. The fraction converted to mechanical energy in the form of shock wave is also expected to increase. This is a factor that needs to be investigated to determine the acoustic energy conversion ratio and the safety of the discharge cell, especially, in the case of repetitive discharges.

Fig. 7.4 shows the expansion of the shock wave for 50 J, 15 J and < 1 J. It reveals that the expansion of the shock front satisfies a power law as given in Chapter 3:

$$R=\alpha t^{a} \qquad 3.18$$

By fitting the curve, we are able to obtain α = 4.02, a = 0.475 for 50 J and α = 3.091, a = 0.4483 for 15 J. The initial kinetic energy, E, is calculated as 3.091 J and 4.02 J for 15 J and 50 J respectively. This shows that for an increase of energy, the percentage of energy that is converted to shock waves (20% for 15 J and 8% for 50 J) decreases.

This tendency can be explained by the fact that the inductance of the water gap is increasing as the gap distance (and energy) is enlarging. As shown in the current signal (Fig. 6.2), for 15 J, the current decay time is much less than for 50 J since the decay of the current depends on the inductance of the gap and the circuit inductance, which is invariable when the gap is changed. Due to the limitation of our electrical diagnostics, the rise times for both current pulses appear with no appreciable difference. However, from the decay time of the

Reproduced with permission of the copyright owner. Further reproduction prohibited without permission.

current pulses for 15 J and 50 J, we can still deduce that the current risetime is slower for 50 J than 15 J. The current risetime indicates how fast the plasma conduction channel is building up and how fast the plasma piston is expanding. Faster expansion of the plasma piston should result in a larger percentage of energy going into the shock wave for 15 J than 50 J.

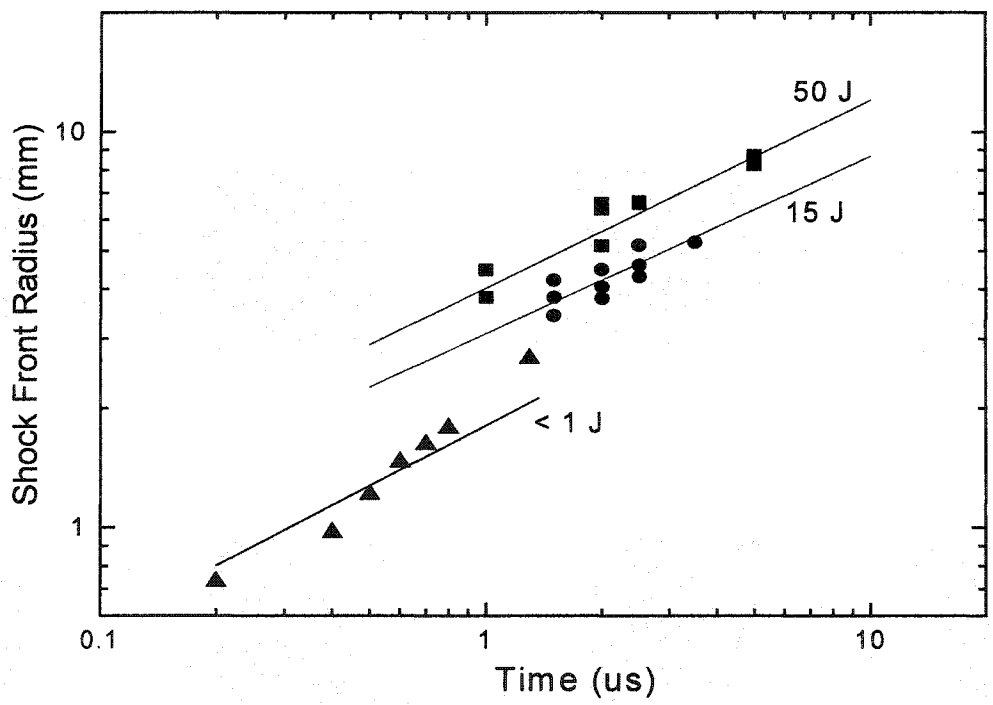

FIG. 7.4. Shock wave developments for energies up to 50 J.

Reproduced with permission of the copyright owner. Further reproduction prohibited without permission.

The pressure, p_s, in the shock wave front, can be estimated by [75]:

$$\int p_s^2 dt = E_s \rho_0 c_0 / 4\pi R_m^2 \qquad 7.4$$

where ρ_0 is the unperturbed density, c_0 is the speed of sound in water, and R_m is the distance from the emission center. For a spherical shock wave front of 1 cm radius, corresponding to an expansion time of 5 μs, with E_s = 4 J, Eq. 7.4 yields a pressure of 2.6×10^7 Pa (approximately 260 atm). At a radius of 2 cm, the pressure decreases to 6.3×10^6 Pa, which a stainless steel chamber with dimensions of several centimeters should be able to withstand. In a much higher energy experiments [40], 8% of the total dissipation of 1.5 kJ is radiated as acoustic energy. After a discharge 50 μs at a distance of 21 cm from the 7.6 cm long gap, a pressure of 10^7 Pa was measured.

It is noted that Eq. 3.18 does not fit for low energies (< 1 J) and results in a large error. Since our data for low energy are obtained with rod-plane electrodes, this could be due to the boundary effect of the electrodes modifying the expansion as describe in 7.2.1, whereas the expansion law is based on shock expansion in free space.

7.2.3 Shock Wave Development in Propylene Carbonate

The shock wave in propylene carbonate shows the same emission pattern as seen in water and also has the dependence on electrode boundary. The temporal and spatial evolution of the shock wave in propylene carbonate is shown in Fig. 6.5, based on data from Fig. 5.14. Although the total energy dissipation in water (~20 mJ) is slightly less than in propylene carbonate (~30

Reproduced with permission of the copyright owner. Further reproduction prohibited without permission.

mJ), the shock wave in water is stronger than that in propylene carbonate. For initial value (t=0), an extrapolated pressure for propylene carbonate is 550 Mpa, which is almost half that of water.

An energy balance analysis of electrical breakdown in liquid has shown that the energy deposited into the discharge gap can be converted into the thermal energy of the heating of plasma, mechanical energy of shock wave, radiation energy, and other forms [77]. Among these, the heating energy of the plasma is the dominant form, which then heats the liquid into vaporization. For liquids with different physical properties, the fraction of energy that is dissipated into each form may be different. For example, as shown in Table 1.2, the heat capacitance of propylene carbonate is nearly three times high than water; we then expect the thermal heating required for plasma formation in propylene carbonate to require more energy than that in water, which could explain the phenomenon observed in Fig. 6.5. Here, we assume the liquid (water and propylene carbonate) within the plasma is completely evaporated, but neglect the heat dissipation due to heat conduction. We also assume an isobaric evaporation and use specific heat to account for the amount of energy consumed for the vaporization of V_p, the plasma volume.

For the initial plasma volume, although we do no have very accurate data from the extrapolation to the initial point where the plasma channel is formed, we are able to obtain a rough size of the initial plasma channel. As we have already seen, for water the extrapolated value is 0.27 mm. Following similar approaches to extrapolate the development of shock in propylene carbonate, we obtain an

Reproduced with permission of the copyright owner. Further reproduction prohibited without permission.

initial plasma radius of about 0.26 mm, which indicates the initial plasma volume is roughly the same as water.

The energy required for the heated material to be transformed into vapor with vaporization temperature T_v is given by:

$$E_v=\rho_0 V_p[c_p(T_v-T_0)]=\rho_0 V_p c_p \Delta T \qquad 7.5$$

where, ρ_0 is the density of the liquid, c_p is the specific heat capacity, T_0 is the temperature at ambient state, usually 20°C . T_v for water is 100°C, for propylene carbonate is 242°C. The density of water is 1000 kg/m^3 and propylene carbonate is 1180 kg/m^3 . The specific heat capacity for water is 4.18 kJ(kg°C)$^{-1}$, for propylene carbonate 2.18 kJ(kg°C)$^{-1}$. A calculation gives that, for the same amount of volume in liquid phase, such as for a cylindrical volume with length of 260 μm, diameter of 200 μm, the energy required to heat the propylene carbonate is 34 mJ, which is 1.7 times higher than that for water 20 mJ. This fact could explain why propylene carbonate has less energetic shock wave emission than water since a larger amount of energy needs to be converted into heating and vaporization. This also indicates that the real plasma size is smaller than the value extrapolated from the shock expansion.

Reproduced with permission of the copyright owner. Further reproduction prohibited without permission.

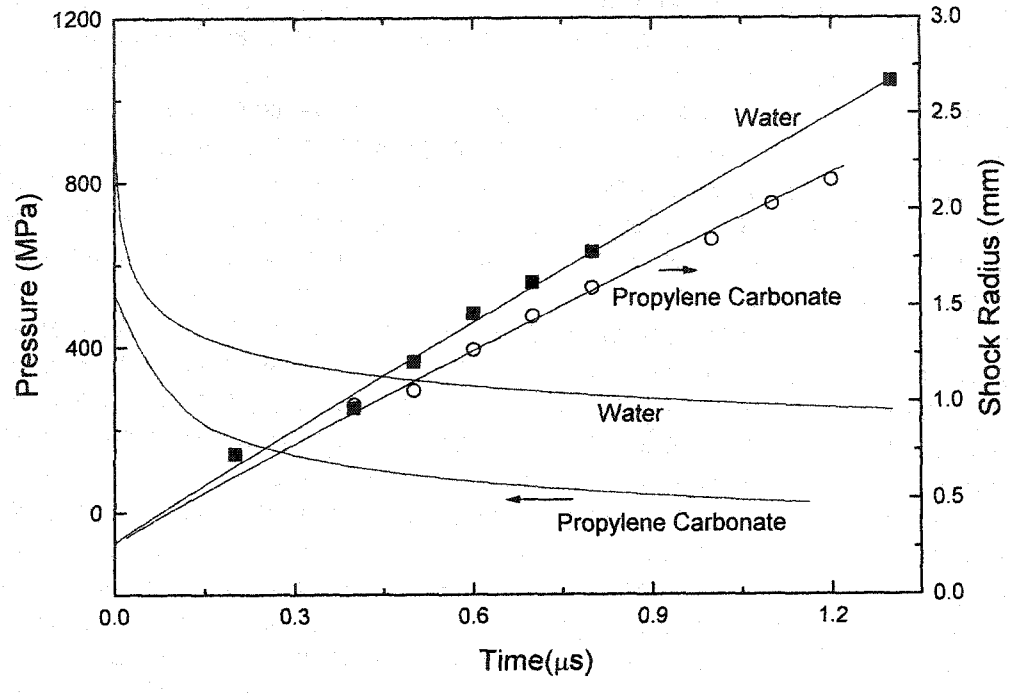

FIG. 7.5. Pressure carried by shock wave and the shock radius after breakdown in propylene carbonate. Pressure and shock radius for water are also shown for comparison.

Reproduced with permission of the copyright owner. Further reproduction prohibited without permission.

7.2.4 Optical Properties and Dynamics of Vapor Bubble in Water

While the shock waves travel through the water gap rather quickly, it takes a long time for the opaque volume between the electrodes to develop and then decay. From the pictures shown in Fig. 5.4, it can be seen that the opaque volume originates from the center area between the two electrodes, and becomes visible at about 1.3 μs. It expands for 0.2 ms and disappears after about 1 ms. The opaqueness can be explained by a change in the index of refraction, which lead us to believe that the volume consists of water vapor generated by the large input in electrical energy into a small volume during the breakdown and expansion of the plasma. The energy density is sufficient to heat the water to its point of evaporation and to provide enough latent heat to cause a phase change.

For the differences in the index of refraction (liquid water (n = 1.33) and water vapor (n = 1)), the laser light used for Schlieren photographs (633 nm) is to be largely deflected, and the vapor bubble appears to be opaque. This is shown schematically in Fig. 7.6. The assumption that the opaque volume represents an expanding water vapor bubble is supported by a model that describes the expansion of such bubbles [78]. The radius of a bubble is, according to this model, dependent on time as described by the following equation:

$$R=R_0 + Ct^{0.4} \qquad 7.6$$

where R_0 is the initial radius of the bubble, and C is a constant related to mass and the kinetic energy of the water surrounding the bubble. The radius of the opaque volume R can be obtained from Schlieren photographs in the temporal

Reproduced with permission of the copyright owner. Further reproduction prohibited without permission.

range from 1.3 μs to 0.9 ms. As shown in Fig. 7.7, R is proportional to $t^{0.4}$ in the expansion phase (< 200 μs), which is in a good agreement with bubble model. An extrapolation to time zero gives us the initial vapor bubble size R_0 = 265 μm, which is close to the source size obtained from shock wave measurements.

When the pressure inside the bubble decreases below the pressure of the surrounding, undisturbed water, the expansion stops and collapse begins (>200 μs). It can be seen that by 1 ms, the bubble has vanished. Compared with the expansion stage, the decay process of the bubble seems to be random and takes a longer time (200-1000 μs) than the expansion (< 200 μs).

Reproduced with permission of the copyright owner. Further reproduction prohibited without permission.

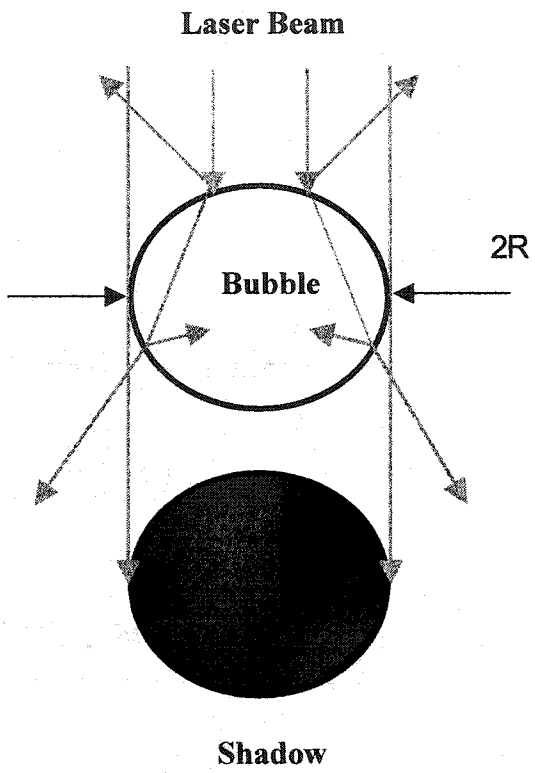

FIG. 7.6. Deflection of He-Ne laser light at vapor bubble (n = 1), in water (n = 1.33), and the resulting image of the bubble.

Reproduced with permission of the copyright owner. Further reproduction prohibited without permission.

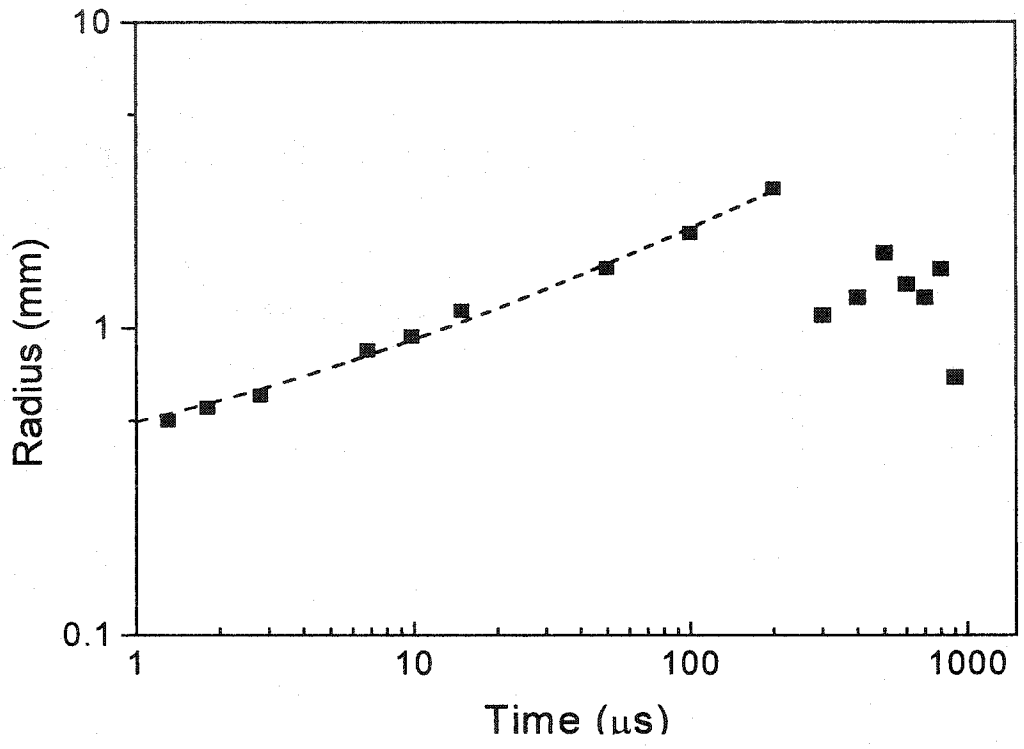

FIG. 7.7. Radius of the vapor bubble, R, versus time. The experimental values (squares) agree well with the results of a model (dashed line).

Reproduced with permission of the copyright owner. Further reproduction prohibited without permission.

7.2.5 Onset of Breakdown in Water

The parameters of the initial plasma can be derived based on our results of postbreakdown phenomena such as shock waves and vapor bubbles. The source of shock waves and the initial vapor bubble is assumed to be identical to the volume occupied by the plasma column. The size of the plasma channel (270 μm) is on the same order as the gap length. This plasma column contains an energy of 46 mJ, calculated by the ideal gas equation $W=p_0V_0$, where p_0 is the pressure of 1 GPa, V_0 is the volume of a cylindrical plasma with a radius of 270 μm and a length of 200 μm. This energy is more than a factor of two larger than the electrical energy input of 20 mJ from the circuit indicating that the original plasma size has a radius a factor of 1.5 smaller than extrapolated value (270 μm) in Fig. 7.3. If we assume the gas number density n, is determined by the vaporized water in a volume V_0, a gas temperature $T = p_0V_0/nR_c$ =2200 K can be expected, where R_c is the gas constant.

7.2.6 Energy Dependence of Vapor Bubble in Water

For energies up to 50 J, it takes less than 1 ms for the vapor bubbles to reach their maximum expansion, as shown in Fig. 7.8. The maximum bubble radius R_{max} (in mm) and the time t_{max} (in ms) to reach it are related by the Rayleigh equation [79]:

$$t_{max} = 0.915R_{max}(\rho/p_a)^{1/2} \qquad 7.7$$

where ρ = 1000 kg/m^3 and p_a=1.0×10^5 Pa, Eq. 7.7 is equivalent to

$$t_{max}/ R_{max} = 0.0915 \qquad 7.8$$

Reproduced with permission of the copyright owner. Further reproduction prohibited without permission.

For < 1 J, 15 J, and 50 J, t_{max} is 0.2 ms, 0.6 ms, and 0.9 ms. R_{max} is 2.85 mm, 7 mm, and 10 mm. Obviously, as the energy increases, the maximum bubble size does not grow linearly and is not strongly dependent on the energy changes.

The energy of a spherical bubble is:

$$W_B = 4\pi(p_0 - p_v)R_{max}^3 \qquad 7.9$$

where p_0 = 0.1 Mpa, p_v = 2230 Pa at 20 °C [80]. Calculations give the bubble energy for < 1 J W_B 6.5 mJ, for 15 J, E_B is 0.146 J, and for 50 J case, E_B 0.42 J. One can see that the kinetic energy for bubble expansion is very small compared to shock wave radiation.

The vapor bubble decays after t_{max}. Fig. 6.6 shows that 10 ms after breakdown, for both of 15 J and 50 J, the gaps become free of vapor. Compared to the recovery of a water gap at 1 J, the recovery time at 50 J takes only about ten times longer although the energy levels have been increased by a factor of fifty.

Reproduced with permission of the copyright owner. Further reproduction prohibited without permission.

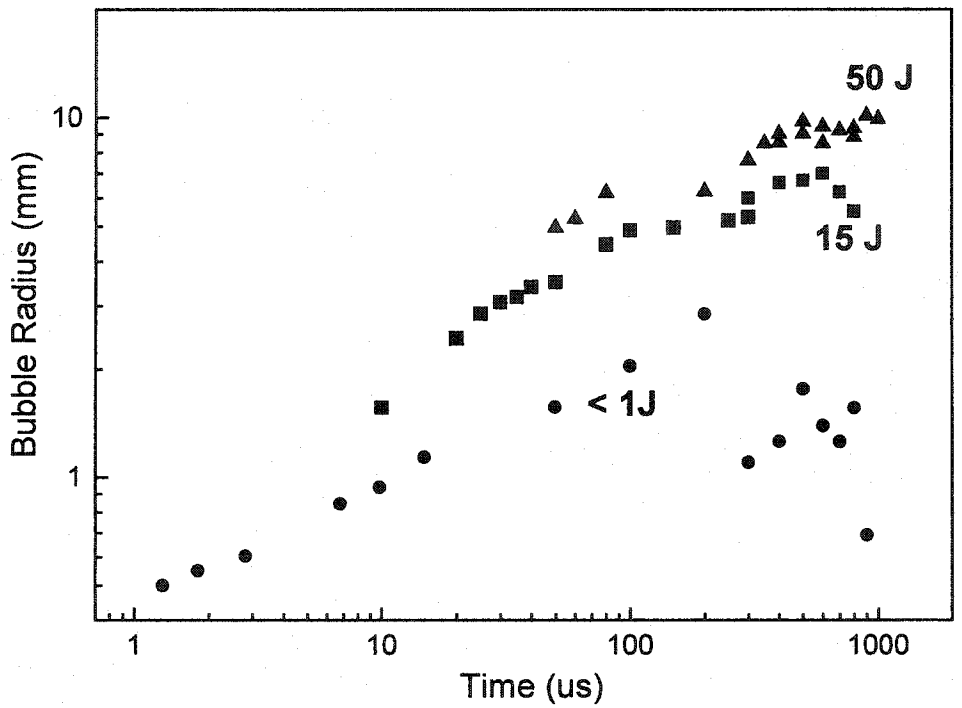

FIG. 7.8. Bubble radius expansion in water for energies up to 50 J.

Reproduced with permission of the copyright owner. Further reproduction prohibited without permission.

7.2.7 Dynamics of Vapor Bubble in Propylene Carbonate

Fig. 7.9 shows the expansion of the vapor bubble after breakdown in propylene carbonate. Based on Eq. 7.7, we use the experimental value R_{max} = 2.5 mm to calculate the time t_{max} as 0.24 ms. This is in agreement with the experimental data of 0.2 ms. The vapor bubble expands in nearly the same manner as water and can be predicted by Eq. 7.6. This supports that vapor bubble expansion is not strongly dependent on the energy, as shown in Section 6.2.5, which changes as the shock wave expands. An extrapolation indicates the initial bubble formation of propylene carbonate is the same size as that in water. At longer times (> 4 ms), the black clogs (Fig. 6.14) cannot be explained as bubbles, suggesting new products are generated, which will be discussed later.

Reproduced with permission of the copyright owner. Further reproduction prohibited without permission.

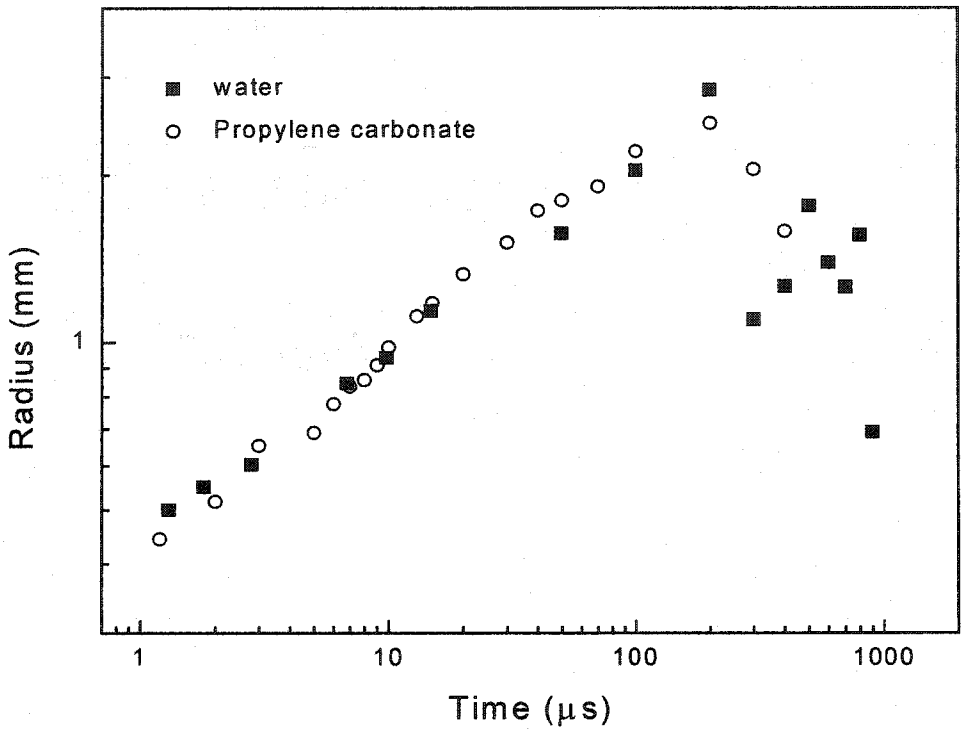

FIG. 7.9. The expansion of the vapor bubble for propylene carbonate. As a comparison, the vapor bubble expansion for water is also shown.

Reproduced with permission of the copyright owner. Further reproduction prohibited without permission.

7.2.8 Effect of Vapor Bubble on the Dielectric Strength of Liquids

In the dielectric recovery of the water after breakdown, the expansion and decay of the vapor bubble determine the dielectric strength. This is supported by the shadowgraphs (Fig. 6.4, 6.7) and electrical pulse probe measurement results (Fig. 6.12). The dependence of the dielectric recovery of the water gap on the time required to eliminate the water vapor bubble can be understood in terms of the dielectric strength of water vapor versus liquid water. The dielectric strength of gases or vapors is always lower than that of liquids. Consequently as long as there are pockets of vapor between the electrodes, the dielectric strength of the gap will be less than that of the water gap without vapor inclusions.

Assuming the vapor/gas pockets left by the previous discharge remains near the inter-electrode volume, a simple model can be shown in Fig. 7.10. The electric field in a spherical gas bubble, which is immersed in a liquid of permitivity ε_{liq} is [81]:

$$E_b=3E_0/(\varepsilon_{liq}+2) \qquad 7.10$$

where E_0 is the field in the liquid in the absence of the bubble. When E_b reaches the ionization field of the gas, (in air 30 kV/cm), partial discharge can occur in the vapor pockets. Assuming E_0=650 kV/cm, which is usually lower than the breakdown voltage of water for a submicrosecond pulse, we obtain E_b = 20 kV/cm, which is close to the breakdown voltage 30 kV/cm of air. This may cause the partial discharge observable in the vapor pockets in Fig. 6.7. In addition, field enhancement in the remaining liquids due to existence of vapor bubble, can also lower the hold-off voltage of the gap.

Reproduced with permission of the copyright owner. Further reproduction prohibited without permission.

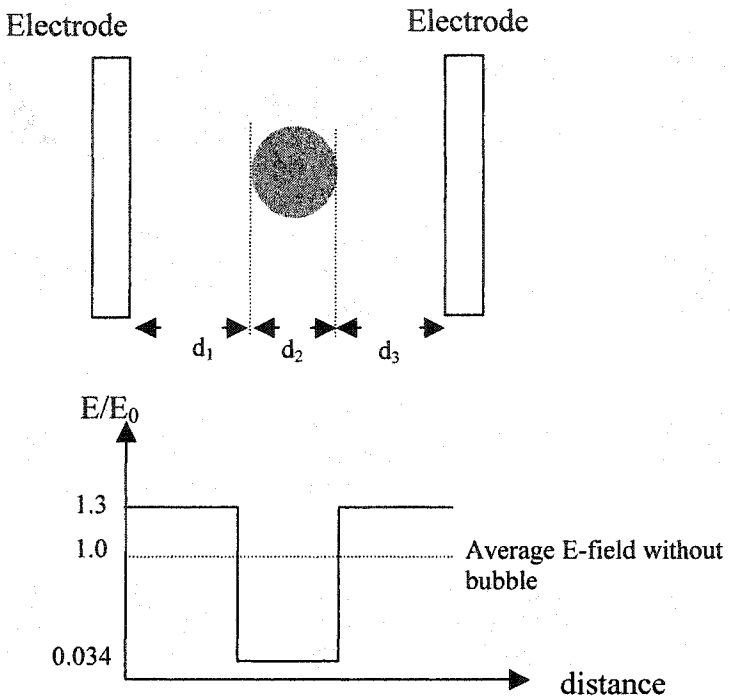

FIG. 7.10. The expansion of vapor bubble for propylene carbonate. As a comparison, the vapor bubble expansion for water is also shown.

The voltage drop across the gap is:

$$U=E_{liq}(d_1+d_3)+E_b d_2 \qquad 7.11$$

here, $d=d_1+d_2+d_3$ is the electrode distance. We have already seen that E_b is lower than E_0; for a given total voltage potential, this will cause field enhancement of E_{liq} (greater than E_0) so as to maintain the potential. For example, if there is a spherical bubble with a diameter of 50 μm presenting in the center of a 200 μm gap, we are able to obtain 30% field enhancement (Fig. 7.10). Here, the field enhancement is defined as the ratio of the electrical field along the axis to the average field with bubble. This effect indicates a voltage applied that

Reproduced with permission of the copyright owner. Further reproduction prohibited without permission.

is lower than the hold-off voltage without bubble could possibly cause the whole gap to break down.

7.2.9 Increasing the Recovery Rate of Liquids

All of the gas-filled bubbles that are present in subsaturated liquid should dissolve away if the ambient pressure is sufficiently high [82]. One approach to accelerate recovery is to use flow instead of waiting for the natural dissolution process. This is already proven for 50 Ω systems, as shown in the pulse-probe results in Fig. 6.12. The recovery rate has been increased from 1 kHz to 1.4 kHz. For higher energies, up to 50 J, a rough estimate indicates an axial laminar flow of 1 L/min can replace the water volume in the for 1 mm gap within 1 ms. However, turbulent flow needs to be avoided since the gas dissolved in the liquid could be released by the imbalanced pressure and adsorb to the electrodes.

Epstein and Prosperetti found an approximate time for the dissolution of a bubble in a liquid initially at uniform gas concentration c_∞, through a mass diffusion process [83]. For a bubble of radius R, in a liquid at a fixed ambient pressure P_∞, the typical duration of the shrinkage of the bubble is roughly given as:

$$t_{cs} \approx \frac{\rho_G [R(0)]^2}{2\alpha_G (c_S - c_\infty)} \qquad 7.12$$

where $c_s = p_{GE}/H$, p_{GE} is the partial pressure of gas in the bubble, $p_{GE} = p_\infty - p_V + 2S/R$, H is Henry's law constant, S is the surface tension of bubble and R is the bubble size. For a 10-micrometer bubble, a complete dissolution takes about

Reproduced with permission of the copyright owner. Further reproduction prohibited without permission.

2.5 s. This prediction may be long compared to our results however, it does point out that one approach to shorten the bubble dissolution is to apply a higher pressure p_∞. It is expected that doubling pressure, for the same size of bubble, can reduce the time of the dissolution by half.

7.3 BREAKDOWN IN PROPYLENE CARBONATE

The black clogs that appear 4 ms after breakdown in propylene carbonate (shown in Fig. 6.14) can be explained as a new, generated product. The plasma channel formed during the breakdown has a temperature as high as at least several thousands Kelvin degrees, which is not only enough to heat the liquid into vapor phase but also provides suitable conditions for degradation of the liquid. This could cause polymer formation during the discharge. As shown in by Soga et al., the polymers can be formed at 440 K with certain ionic mechanism in propylene carbonate [72].

The temperature of the plasma in propylene carbonate could be roughly evaluated by means of equation state, as shown in Section 7.3. The initial size of the plasma column has similar dimension as that formed in water breakdown, in our case, 260 μm. This could lead to a similar temperature of several thousand Kelvin degrees, which is much higher than 440 K, the temperature required for polymerization of propylene carbonate. Polymer formation has been proved by our extraction from the treated propylene carbonate. The degraded products are isolated by dissolving the propylene carbonated in excess of water and solidified by drying, which confirms the polymer has been formed. Raman spectrum (Fig.

Reproduced with permission of the copyright owner. Further reproduction prohibited without permission.

6.16) has shown that the C=O signal in the Raman spectra of propylene carbonate is at 1780 cm^{-1} and it shifted to 1730 cm^{-1} in the polymer. This is because the carbonate group in propylene carbonate is incorporated in a five member ring with some strain on the O-C-O bond angle. The signal of C=O group of strain free carbonate is expected to be 40 to 50 cm^{-1} lower than the signal of a cyclic carbonated group. Upon polymerization the ring structure breaks, and the product contains an open chain structure as shown in Fig. 7.11, explaining the shift of the C=O signal from 1780 cm^{-1} to 1730 cm^{-1}. Another change in the spectra is that two signals, at 712 cm^{-1} and 850 cm^{-1}, disappeared and a new signal at 812 cm^{-1} appeared. We assume these signals are due to C-O single bond which is in a five member cycle in the propylene carbonate and in an open chain structure in the product polymer.

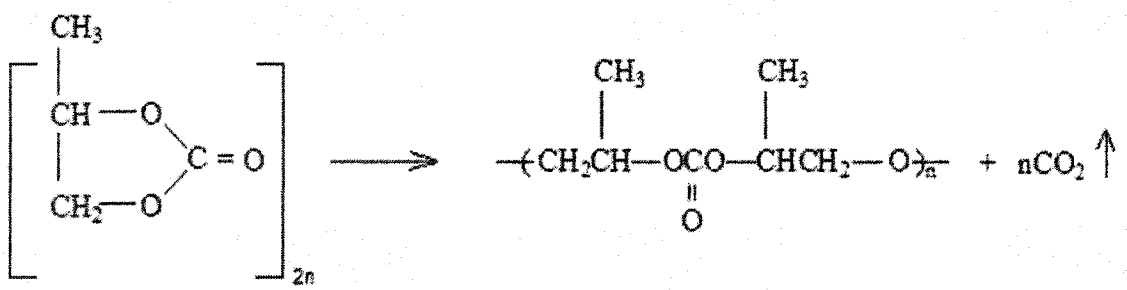

FIG. 7.11. Propylene carbonate degrades into the polymer polypropylene carbonate.

Reproduced with permission of the copyright owner. Further reproduction prohibited without permission.

CHAPTER VIII

SUMMARY

Electrical breakdown and the following hydrodynamic process in water and propylene carbonate are explored using submillimeter gaps. Independent of polarity effect, breakdown strengths of water are found to be between 600 and 750 kV/cm for both short pulse (< 200 ns) and long-term stress (7-8 μs). The dielectric strength of water, up to 750 kV/cm, indicates that an energy storage density of at least 2 J/cm^3 can be achieved. In addition, applying water as high power switching medium allows a reduction in the size of high power switches considerably as compared to gaseous switches in addition to reducing switch inductance.

Three processes characterize the postbreakdown phase of a water gap: decay of discharge plasma, emission of shock waves, and formation and decay of vapor bubbles. The process with the fastest time constant is the decay of the plasma as indicated by the decreasing light emission from the switch plasma. The time constant is on the order of one microsecond for energies less than 1 J. The second postbreakdown process is the propagation of shock waves emitted from the plasma. The time constant of the second phase is dependent on the shock wave velocity, which in turn is dependent on the plasma pressure (pressure values of up to 1000 MPa were calculated) and the dimensions of the discharge cell. In our system, the time constant is several microseconds. The third process is the formation and decay of a water vapor bubble. The energy

Reproduced with permission of the copyright owner. Further reproduction prohibited without permission.

deposited into the plasma is eventually transformed into thermal energy, leading to a phase transition from liquid to vapor in a small volume between the electrodes. The vapor expands in the form of a bubble until pressure balance is achieved. It then decays, although not necessarily through symmetric radial contraction, as seen in the Schlieren photographs. The final process is on the order of one millisecond and determines the full recovery of the water gap.

The studies of postbreakdown have been extended to higher energies, up to 50 J. The percentage of energy converted to shock wave decreases as energy rises. For 15 J, the shock energy is calculated as 3 J, accounting for 20% of the total stored energy. It decreases to 8% (4 J) for 50 J. The pressure carried by shock waves at 50 J is 2.6×10^7 Pa (approximately 260 atm) for a spherical shock wave front of 1 cm radius, corresponding to expansion time of 5 μs. At a radius of 2 cm, the pressure decreased to 6.3×10^6 Pa. The vapor bubble expands to its maximum radius, 1 cm, in less than 1 ms for all energies up to and including 50 J. The vapor bubble decays approximately 10 ms after breakdown, indicating a full recovery. Although the energies have been increased by a factor of 50, the recovery time does not take 50 times longer compared to energies less than 1 J. For much higher energy switch operation (>100 J), the formation of shock waves and the possible damage to the discharge chamber needs to be considered in repetitive operation mode. Because of the rapid decay of the pressure carried by shock wave, the simplest way to prevent damage is to provide large volumes of water around the discharge gap. For fast switches with low inductance, this might not be a practical option. Mechanical reflectors would

Reproduced with permission of the copyright owner. Further reproduction prohibited without permission.

need to be installed to deflect the shock wave and guide it into areas where the shock wave energy can be safely dissipated [84].

The spatial and temporal postbreakdown and dielectric recovery has been extended to another polar liquid, propylene carbonate. Plasma formed in the discharge decays on the order of 1 μs, which is in the same range as that in water breakdown however shock wave pressure (initial value) is about two times less. This phenomenon is considered to be due to a larger fraction of energy being converted into heating instead of to shock mechanical energies. The vapor bubble expands to its maximum size of 2.48 mm, close to that of water vapor (2.85 mm), nearly 200 μs after breakdown. Besides the decay of the vapor in the long-term dielectric recovery process, polypropylene carbonate, a polymer formed in the discharge, is observed 4 ms after breakdown. The size of the polymer is a half-millimeter which is eventually dissolved in the liquid propylene carbonate.

Electrical pulse-probe systems support that the dielectric recovery is determined by the presence of the vapor left by the previous breakdown. For static water and energies less than 1 J, when pulse rate reaches up to 1 kHz, the dielectric strength is at the same level as the fully recovered water, indicating the recovery time is 1 ms. For higher pulse rates (greater than 1 kHz), the dielectric strength is not recovered fully, which is a consequence of the low dielectric strength of the vapor bubble and the breakdown in liquid caused by field enhancement. This is confirmed in the pulse probe experiments of propylene carbonate, which demonstrate an even lower voltage recovery rate not only

Reproduced with permission of the copyright owner. Further reproduction prohibited without permission.

because of the presence of the vapor but also because of the generated polymer cluster.

The relatively small discharge volume enables us to use flow to quickly remove the bubble generated during discharge, allowing the gap to operate at a high repetition rate. The efforts to accelerate the recovery of the water after breakdown instead of waiting until it recovers naturally have been successfully proved. Laminar flow from both the transverse direction and axial direction successfully eliminate the vapor pockets more quickly than in controls. Pulse-probe experiments have shown the recovery rate can be increased from 1 kHz to 1.4 kHz for axial flow, in which one electrode is a nozzle introducing a moderate flow of 0.4 L/min. A recovery rate of 0.5 -1 kHz can be achieved for energies of 50 J per switching cycle with proper laminar flow. This is the same rate as an oil switch [85]. Turbulent flow deteriorates the recovery rate and needs to be avoided. However, it creates a large volume discharge by a relatively low magnitude voltage, which is favorable in water treatments.

Finally, compact, high pulsed power systems can be realized by making use of water as a dielectric in the energy storage and switching medium [86-87]. An all-water system has shown that with a hold off voltage 20 kV, the voltage rise time is in the ns range [88]. The repetition rate of 0.5 kHz is realized in a burst mode. Propylene carbonate, due to its slow recovery time, may require rapid flow if it is to be used as a switching medium.

Reproduced with permission of the copyright owner. Further reproduction prohibited without permission.

BIBLIOGRAPHY

1. A. H. Sharbaugh and P. K. Watson, Progress in Dielectrics, Wiley, New York, pp.199-248 (1982).

2. T. H. Martin, A. H. Guenther and M. Kristiansen, J. C. Martin On Pulsed Power, Plenum, New York, pp.191-199 (1996).

3. E.E. Kunhardt, L. G. Christophorou,and L. H. Luessen, The Liquid State and Its Electrical Properties, NATO ASI Series, Martinus Nijhoff Publishers, 520 (1981).

4. A.J. Toepfer, Advances in Electronics and Electron Physics, edited by L. Maron and C. Marton, Academics, San Diego, CA, **53**, 1 (1980).

5. E. V. Yanshin, I. T. Ovchinnikov, and Y. N. Vershinin, Zh. Tekh. Fiz., **43**, 1303 (1974).

6. S. Katsuki, D. Takano, T. Namihira, and H. Akiyama, *Review of Scientific Instruments*, **72** (6), pp. 2759-2763 (2001).

7. I. Vitkovitsky, High Power Switching, Van Nostrand Reinhold Company, New York, pp.116-137 (1987).

8. S. M. Turnbull, S. J. MacGregor, F. A. Turema and A. Jmcphee, *J. Phys. D: Appl. Phys.*, **33**, pp.1410-1416 (2000).

9. M. Zahn, Y. Ohki, D. B. Fenneman, R. J. Gripshover, and V. H. Gehman, *Proc. IEEE,* **74**, 1182 (1986).

10. J. Talati, T. Schah, A. Memon, M. Sidhwa, S. Adil, and A. Omair, *J. Urology* **146**, 1482 (1991).

11. I. Z. Okun, *Sov. Phys.-Tech. Phys.* **16**, 219 (1971).

Reproduced with permission of the copyright owner. Further reproduction prohibited without permission.

12. R. D. Rechtier, K. L. Hambacker, and R. F. Ballard, Jr., *Geophys.* **58**, 660 (1993).

13. E. C. Cassidy, R. E. Hebner, M. Zahn, and R. J. Sojka, *IEEE Trans. Electri. Insul.*, **EI-9**, pp. 43-56 (1974).

14. Y. Minamitani, B. Goan, J. Kolb, S. Xiao, C. Bickes, X. Lu, M. Laroussi, K. H. Schoenbach, S. Kono, R. P. Joshi, Submitted to Power Modulator Symposium, San Francisco, CA (2004).

15. MURI CP^3 annual meeting, K. H. Schoenbach, Hollywood, CA (2002).

16.T. S. Light, S. L. Licht, *Anal. Chem.*, **59**, pp.2327-2330 (1987).

17. S. Grimnes, and O. G. Martinsen, Bioimpedance and Bioelectricity Basics, Academic Press, San Diego, CA (2000).

18. N. Felici, *IEEE. Trans. Electr. Insul.*,, **20**, 233 (1975).

19. V. H. Gehman, Jr., T. L. Berger, and R. J. Gripshover, "Theoretical Considerations of Water-dielectric Breakdown Initiation For long Charging Times," *6th IEEE Pulsed Power Conference, Arlington*, VA (1987).

20.J. O'M. Bockris and A. K. N. Reddy, Modern Electrochemistry, Volume 2, Chapter 7, Plenum Press, NY (1973).

21. L. Onsager, *J. Amer. Chem. Soc.* **58**, 1486 (1936).

22. B. Singh, W. G. Chadband, C. W. Smith, and J. H. Calderwood, *J. Phys. D: Appl. Phys.*, **5**, pp.1457-1466 (1972).

23. J. C. Devins, S. J. Rzad, and R. J. Schwabe, *J. Appl. Phys.*, **52** (7), pp. 4531-4545 (1981).

24. H. M. Jones and E. E. Kunhardt, J. Appl. Phys., **77**, 795 (1995).

Reproduced with permission of the copyright owner. Further reproduction prohibited without permission.

25. T. J. Lewis, *IEEE Trans. Electr. Insul.*, **1**, pp. 336-351 (1994).

26. A. H. Sharbaugh, J. C. Devins, and S. J. Rzad, *IEEE Trans. Electr. Insul.,* **13** (4), pp. 249-276 (1978).

27. P.K.Watson, W.G. Chadband, and M. Sadeghzadeh-Araghi, *IEEE Trans. Electr. Insul.*, **26** (4), pp. 543 –559 (1991).

28. M.Sadeghzadeh-Araghi, M.I.Qureshi, W.G.Chadband,and P.K.Watson, *IEEE Trans. Electr. Insul.*, **26** (4), pp. 663–672 (1991).

29. A. Beroual, *J. Appl. Phys.*, **71** (3), pp.1142 – 1145 (1992).

30. S.M.Korobeinikov, *High Temperature*, **36** (4), pp. 541 –547 (1998).

31. V.Giraud and P.Krebs, *Chemical Physics Letters*, **86** (1), pp. 85–90 (1982).

32.H.M.Jones and E.E.Kunhardt, *J. Phys. D: Applied Physics*, **28** (1), pp.178 – 188 (1995).

33. T. J. Lewis, *IEEE Trans. Dielec. and Electri. Insul.*, **5** (3), pp. 306-315 (1998).

34. T. J. Lewis, *IEEE Trans. Dielec. and Electri. Insul.*, **10**, pp. 948-995 (2003).

35. R. P. Joshi, J. Qian, K. H. Schoenbach, E. Schamiloglu, *J. Appl. Phys.*, **96** (7), pp. 3617-3625 (2004).

36. R. P. Joshi, J. Qian, G. Zhao, J. Kolb, K. H. Schoenbach, E. Schamiloglu, J. Gaudet, *J. Appl. Phys.*, **96** (9), pp. 5129-5139 (2004).

37. F. Jomni, F. Aitken, and A. Denat, *J. Acoust. Soc. Am.,* **107** (3), 1203 (2000).

38. D. B. Fenneman and R. J. Gripshover, *IEEE Trans. Plasma. Sci.*, PS-8, 209 (1980).

39. L. S. Levine and I. M. Vitkovitsky, *IEEE Trans. on Nucl. Sci. NS.,* **18**, pp. 255-264 (1971).

Reproduced with permission of the copyright owner. Further reproduction prohibited without permission.

40. J. P. VanDevender, *J. Appl. Phys.*, **49**, pp. 2616-2620 (1978).

41.K. H. Schoenbach, S. Katsuki, R. H. Stark, E. S. Busescher, and S. J. Beebe, *IEEE Trans. Plasma. Sci.,* **30**, pp. 293-300 (2002).

42.B. Ganguly, WPAFB, private communication.

43. S. Katsuki, S. Xiao, R. P. Joshi, M. Laroussi, and K. H. Schoenbach, *Conf. Record, 25th Modulator Symposium, Hollywood, CA*, 199 (2002).

44. J. Kolb, S. Kono, S.Xiao, B. Goan, XP. Lu, C. Bickes, M. Laroussi, R. P. Joshi, K. H. Schoenbach, E. Schamiloglu, *IEEE Pulse Power Conference*, Dallas, Texas (2003).

45. F. Leipold, G. Yu, R. H. Stark, A. Abou-Ghazala, and K. H. Schoenbach, 24th Power Modulator Symposium, Norfolk, VA (2000).

46. E. Kuffel, W. S. Zaengl and J. Kueffel, High Voltage Engineering: Fundamentals, Butterworth-Heinemann, Woburn, MA (2000).

47. J. C. Martin, Nanosecond pulse techniques, *Proceedings. IEEE*, **80** (6), pp. 934-945 (1992).

48. D. B. Fenneman and R. J. Gripshover, *2nd IEEE International Pulsed Power Conference*, Lubbock, Texas (1979).

49. J. Kolb, X. Lu, S. Xiao, C. Bickes, Y. Minamitani, M. Laroussi, K. H. Schoenbach, R. P. Joshi, E. Schamiloglu, submitted to 26th Power Modulator Symposium, San Francisco, CA (2004).

50. F. J. Zutavern, M. T. Buttram, and M. W. O'Mallery, *IEEE Conference record of Sixteenth Power Modulator Symposium*, pp. 273-279 (1984).

Reproduced with permission of the copyright owner. Further reproduction prohibited without permission.

51. Ya. B. Zel'dovich and Yu. P. Raizer, Physics of Shock Waves and High-Temperature Hydrodynamic Phenomena, Academic Press, New York (1966).

52. P. S. Sincerny, "Electrical Breakdown Properties of Water for repetitively Pulsed Burst Conditions", *3rd IEEE International Pulsed Power Conference*, Albuquerque (1981).

53. H. M. Jones and E. E. Kunhardt, *IEEE Trans. Dielectr. Electr. Insul.*, **1**, pp. 1016-1025 (1994).

54. A. Beroul, *J. Appl. Phys.*, **73** (9), pp. 4528-4533 (1993).

55. P. A. Brnes, K. E. Rieckhoff, *Appl. Phys. Lett.*, **13**, 282 (1968).

56. XinPei Lu, Mounir Laroussia, Juergen Kolba, Susumu Konob, and K. H. Schoenbach, IEEE Proceeding of Pulsed Power Conference, Dallas, Texas, (2003).

57. W. B. Kunkel, Plasma Physics in Theory and Application, McGraw-Hill, NY (1966).

58. V. M. Fedorov, " High Power Nanosecond Discharge Channel in Water", Megagauss V Conference, Novosibersk, USSR (1989).

59. V. M. Kosenkov and N. I. Kuskova, *Sov. Phys. Tech. Phys.*, **32** (10), 1215 (1987).

60. N. M. Beskaravainyi, V. G. Kovalev, and E. V. Krivitskii, *Zh. Tekh. Fiz.*, **64**, pp.197-200 (1994).

61 E. Gidalevich, R. L. Boxman and S. Goldsmith, *J. Phys. D: Appl. Phys.*, **37**, pp. 1509-1514 (2004).

62. J. W. Robinson, *J. Appl. Phys.*, **44** (1), pp. 76-81 (1973).

Reproduced with permission of the copyright owner. Further reproduction prohibited without permission.

63. S.I. Braginskii, *Sov. Phys. JETP*, **34**, 1068 (1959).

64. A. V. Donskoi, V. S. Klubnikin and A. A. Salangin, *Sov. Phys. Tech. Phys.*, **30** (11), pp. 1255-1257 (1985).

65. R. Courant and K. O. Friedrichs, Supersonic Flow and Shock Waves, Interscience Publishers, Inc., NY (1948).

66. G. Schmidt, Physics of high Temperature Plasmas (second edition), Academic Press, New York (1979).

67. M. Zahn, E. O. Forster, E. F. Kelley and R. E. Hebner, JR., *J. Electrostatics*, **12**, pp. 535-546 (1982).

68. L. I. Sedov, Similarity and Dimensional Methods in Mechanics, Academic Press, New York (1959).

69. K.H. Schoenbach, J. Cooper, A. Garner, B. Goan, R.P. Joshi, J. Kolb, S. Katsuki, S. Kono, M. Laroussi, F. Leipold, X. Lu, C. Mallot, J. Quian, S. Xiao, *BEAMS 2002,* 14th Intern. Conf. On High-Power Particle Beams, Albuquerque, NM, IAP Conf. Proc., 111 (2002).

70. M. Hara and H. Akiyama, High Voltage Pulsed Power Engineering, Mori Kita Publisher (in Japanese) (1991).

71. G. S. settles, Schlieren and Shadowgraph Techniques, Springer-Verlag, Berlin (2001).

72. K. Soga, Y. Tazuke, S. Hosoda and Sakuji, *Journal of Polymer Science*, **15**, pp. 219-229 (1977).

73. Magic user's manual, Mission Research Corporation, October (2003).

Reproduced with permission of the copyright owner. Further reproduction prohibited without permission.

74. A. Udias, Principles of Seismology, Cambridge University Press, New York (1999).

75. A.Vogel , S. Busch, and U. Parlitz, *J. Acoust. Soc. Am.*, **100**, pp. 148-165 (1996).

76. Murata,K., Takahashi,K. and Kato,Y., Shock Waves, Springer-Verlag, Berlin, pp.947–952 (1992).

77. F. Aitken, F. M. J. Mccluskey and Denat, *J. Fluid. Mech.*, **327**, pp. 373-392 (1996).

78. A. Larsson, A. Sunesson, J. Garmer and S. Kroll, *IEEE Trans. Dielectr. Electric. Insul.*, **8**, pp. 212-219 (2001).

79. R. T. Knapp, J. W. Daily, F. G. Hammitt, Cavitation, McGraw-Hill, New York (1971).

80. R. C. Weast (Ed): CRC Handbok of Chemistry and Physics, CRC press, Boca Raton (1988).

81. K. C. Kao, Trans. AIEEE Elec. Ins. **E1-11**, pp. 121-128 (1976).

82. C. E. Brennen, "Cavitation and Bubble Dynamics," Oxford University Press, New York (1995)

83. M. S. Plesset and A. Prosperetti, *Ann. Rev. Fluid Mech.*, **9**, 145-185 (1977).

84. P. Sunka, *Physics of Plasmas*, **8** (5), pp. 2587-2594 (2001).

85. R. Curry, P. D'A. Champney. C, Eichenberger, J. Fockler, D. Morton, R. Sears, I. Smith, and R. Conrad, *IEEE. Trans. Plasma. Sci.*, **20** (3), pp. 383-392 (1992).

Reproduced with permission of the copyright owner. Further reproduction prohibited without permission.

86. J. Deng, R. H. Stark, K. H. Schoenbach, Proc. PPPS2001, Las Vegas, NV, 1587 (2001)

87. S. Xiao, S. Katsuki, J. Kolb, S. Kono, M. Moselhy and K. H. Schoenbach, *Conf. Record, 25th Modulator Symposium, Hollywood*, CA, 471 (2002).

88. C. Bickes, J. F. Kolb, and K. H. Schoenbach, submitted to *26th Modulator Symposium, San Francisco*, CA (2004).

Reproduced with permission of the copyright owner. Further reproduction prohibited without permission.

APPENDIX A

THERMAL RADIATION OF THE PLASMA IN WATER DISCHARGE

Barnes and Rieckhoff found the spectral energy density of plasma radiation to be in the wavelength between 300 nm and 900 nm, which closely resembles the spectral distribution of a blackbody radiator [55]. The spark in water breakdown created by a short pulse (<200 ns) of electrical field 750 kV/cm emits continuum radiation peaked at 380 nm [56]. No line radiation was observed. A comparison with blackbody radiation provides a plasma temperature corresponding to an energy between 1 eV and 2 eV.

In an arc discharge under breakdown field between 200 and 500 kV/cm with an energy >1000 J in the arc, the light observed in water is consistent with a temperature T >1 eV [37]. OH absorption lines dominate the emission spectrum. The spectral distribution of emitted light between 360 and 410 nm could not be adequately fitted to a blackbody emission profile.

Blackbody radiation is emitted by a plasma which is in thermodynamic equilibrium [57]. In plasma, it is mainly the electrons that contribute to this radiation; if the electrons are in equilibrium, even if the ions are non-Maxwellian or at a different temperature, we may discuss blackbody equivalence. Radiation power density for a black body is given as [58]:

$$W_{rad} = 5\ (100\ r)\ (T/30)^4\ GW/cm \qquad A.1$$

Where T is the temperature in eV and r is the plasma radius in cm. For example, W_{rad} = 5 GW/cm when T = 30 eV and r = 0.01 cm. For a low temperature

Reproduced with permission of the copyright owner. Further reproduction prohibited without permission.

blackbody radiator (1 eV), W_{rad} drops to nearly 5 kW/cm. Thus, the plasma radiation plays a minor role in the energy balance of the discharge.

Reproduced with permission of the copyright owner. Further reproduction prohibited without permission.

APPENDIX B

FLUID MODEL

The problems of treating a flow involving a discontinuity can be completely determined by the three conservation laws and entropy conditions.

Momentum condition gives:

$$\frac{\partial M}{\partial t}+\frac{\partial}{\partial r}(M^2/\rho+p)=0 \qquad \text{A.2}$$

Mass flow condition can be written:

$$\frac{\partial \rho}{\partial t}+\frac{\partial M}{\partial r}=\frac{3k_L(\frac{\partial T}{\partial r})_{r=R}}{RL} \qquad \text{A.3}$$

Here we include the average increment of mass due to the vaporization of the plasma-liquid layer. k_L is the thermal conductivity of water. The heat supplied to the interface from the plasma is: $4\pi R^2 k_L(\frac{\partial T}{\partial r})_{r=R}$, the rate of mass change is then, $\frac{3k_L(\frac{\partial T}{\partial r})_{r=R}}{RL}$, where L is the heat of the evaporation of the liquid.

In the energy conservation, we account for the Joule heating source and heat dissipation due to diffusion:

$$\frac{\partial}{\partial t}W+\frac{\partial}{\partial r}[M(W+p)/\rho+k_L\frac{\partial T}{\partial r}]=J^2/G_1 \qquad \text{A.4}$$

where $W=p/(\gamma-1)+\frac{1}{2}\rho v^2$. G is the conductance, $G= G_1+G_2$, G_1 is the conductance of the thermal plasma ($G_1=\pi R^2\lambda(T)W_{eff}$), λ is the electrical conductivity of the

Reproduced with permission of the copyright owner. Further reproduction prohibited without permission.

partially ionized plasma ($\lambda=\frac{e^2}{\sqrt{m_e kT}}\frac{x}{x\sigma_{ei}+(1-x)\sigma_{ea}}$, where $x=n_i/n$ is the ionization degree, σ_{ei} and σ_{ea} is the cross section for electron-ion collisions, σ_{ea} is the cross section for electron-neutral particle collisions), and G_2 is the conductance of the circuit.

The external circuit supplies electrical energy to the fluid motion through the current (or current density).

$$L\frac{di}{dt}+i/G+\frac{1}{C}\int_0^t id\tau = U_0 \qquad \text{A.5}$$

Where L is the circuit inductance, C is the circuit capacitance and U_0 is the initial charging voltage of the capacitor. With the Tait equation relating pressure and density in water, $p=B[(\rho/\bar{\rho})^{\gamma}-1]$, equations A.2-A.5 form a closed set of equations and give a full description of the plasma channel expansion due to Joule heating. Numerical solution can be given by finite difference schemes combining a random choice algorithm.

Reproduced with permission of the copyright owner. Further reproduction prohibited without permission.

VITA

Shu Xiao

Education:

Doctor of Philosophy (Electrical Engineering), Old Dominion University, Norfolk, Virginia December 2004

Master of Science (Microwave Engineering), University of Electronic Science and Technology of China, Chengdu, Sichuan, China, August 1999

Bachelor of Science (Physics), Gannan Teacher College, Jiangxi, China, July 1996

Reproduced with permission of the copyright owner. Further reproduction prohibited without permission.